

# UC Berkeley

## UC Berkeley Electronic Theses and Dissertations

### Title

Regulatory Dynamics of Natural and Artificial Photosynthesis

### Permalink

<https://escholarship.org/uc/item/7f97r3pk>

### Author

Zaks, Julia

### Publication Date

2012

Peer reviewed|Thesis/dissertation

**Regulatory Dynamics of Natural and Artificial Photosynthesis**

by

Julia Zaks

A dissertation submitted in partial satisfaction of the

requirements for the degree of

Doctor of Philosophy

in

Applied Science & Technology

in the

Graduate Division

of the

University of California, Berkeley

Committee in charge:

Professor Graham Fleming, Chair

Professor Robert Dibble

Professor Krishna Niyogi

Professor Naomi Ginsberg

Fall 2012

**Regulatory Dynamics of Natural and Artificial Photosynthesis**

Copyright 2012

by

Julia Zaks

## **Abstract**

Regulatory Dynamics of Natural and Artificial Photosynthesis

by

Julia Zaks

Doctor of Philosophy in Applied Science & Technology

University of California, Berkeley

Professor Graham Fleming, Chair

The research presented in this dissertation focuses on understanding the regulation of excited states, both in natural photosynthesis and in artificial systems.

Chapters 1, 2, and 3 contribute to the understanding of natural photosynthesis by describing a mathematical model that quantifies a process by which plants protect themselves from damage due to excess absorbed energy. Chapter 1 contains a description of a mathematical model of photosynthetic processes that govern the rapid components of nonphotochemical quenching. Chapter 2 contains a manual describing a Graphical User Interface (GUI) for this model. Chapter 3 extends the model of nonphotochemical quenching and applies the model to understand the role of the specific pigments and proteins which are required for rapidly-reversible nonphotochemical quenching to take place.

Chapters 4 and 5 are focused on experimental work done on artificial systems. Chapter 4 reports on the excited state dynamics of a pH-sensitive dye that has been used to regulated the excited state lifetime of an artificial antenna. Chapter 5 reports measurements of four molecular donor-bridge-acceptor triads where the bridge between the donor and acceptor is different in each triad, with the aim of understanding how the chemical bonding between donor and acceptor affects the timescales and yield of energy transfer and charge separation.

*For my family*

## Acknowledgements

There are many people who have shaped my experience at Berkeley. I am lucky to have joined the lab of my advisor, Graham Fleming. Graham has taught me how to formulate scientific questions and look for answers in a pragmatic way. Graham has also fostered an environment of both independence and collaboration, and this experience has taught me many lessons about the reality of how science is done.

Thanks to the students and postdocs in the Fleming group who mentored me in the first few years: Yuan-Chung Cheng, Tae Ahn, Matthew Graham, Ying-Zhong Ma, Naomi Ginsberg, Gabriela Schlau-Cohen, Jacquelyn Burchfield, Tessa Calhoun, and Hohjai Lee. In the later half of graduate school I have been fortunate to work with Kapil Amarnath, Eleonora De Re, Emily Jane Sylak-Glassman, Doran Bennett, Jahan Dawlaty. Outside of the Fleming group, I have worked with and learned from David Kramer, Saar Kirmayer, Jibin Sun, Matthew Brooks and Zhirong Li.

I'd like to thank the other professors of my dissertation committee: Kris Niyogi, Naomi Ginsberg, and Robert Dibble. Kris has been a collaborator on all the photosynthesis-related work in this thesis, and I've gained a great deal from interacting with him and his students. Kris has repeatedly shown me much more generosity with his time, patience than I expected. Naomi has provided me with a great deal of mentoring, both five years ago when I was starting graduate school and now as I look to the future. The integrity in her approach to science sets an important example for me. Professor Dibble's enthusiasm for science is infectious, and I've come away from all my interactions with him excited to learn more.

I have greatly benefitted from being part of the Applied Science and Technology Graduate Group at Berkeley. I could not have asked for a better group of peers. Professor Dave Attwood has been a consistent source of support, mentoring, and advice, and for chairing both my Preliminary and Qualifying exam. Pat Berumen, who was the administrator of our graduate group during the majority of my time in grad school, took care of everything with unsurpassed competence and dedication. Thanks also to Professors Roger Falcone, Jih-Wei Chu, and Robert Dibble for serving on my prelim and qualifying exams.

Graduate school has provided me with the time and opportunities to develop skills that I value and enjoy using. I'd like to thank Naomi Ginsberg, Trygve Ristroph, and Chiaki Treynor for giving positive perspective on the future, and Jessica Seeliger who has, over the past nine years, given me many much-needed nudges in the right direction.

Finally, I'd like to thank my parents, my grandparents, my brothers, and my parents-in-law and sister-in-law for their support during this long process, and especially my husband Robert Chin, who always inspires me, for his patience and optimism.

For the first two years of graduate school I was supported by a Chancellor's Fellowship from the university. This work was funded by the Division of Chemical Sciences, Office of Basic Energy Sciences of the Department of Energy through Grant DE-AC03-76SF000098 and by the Helios Solar Energy Research Center, which is supported by the Director, Office of Science, Office of Basic Energy Sciences of the U.S. Department of Energy under Contract No. DE-AC02-05CH1123.

# Contents

<b>1</b>	<b>A Model of Rapidly-Reversible Nonphotochemical Quenching</b>	<b>3</b>
1.1	Introduction . . . . .	4
1.2	Mathematical model . . . . .	7
1.2.1	pH-regulated quenching of excited chlorophyll . . . . .	7
1.3	Description of modules . . . . .	10
1.3.1	Energy transfer within PSII . . . . .	10
1.3.2	Electron transfer chain after PSII . . . . .	10
1.3.3	Luminal buffering and ion motion . . . . .	11
1.3.4	Activation of ATP synthase . . . . .	13
1.4	Comparison with PAM fluorescence . . . . .	14
1.4.1	Extracting NPQ from PAM measurements . . . . .	14
1.4.2	PAM simulation . . . . .	15
1.5	Model parameters . . . . .	16
1.6	Results and discussion . . . . .	18
1.6.1	qE as a feedback loop . . . . .	20
1.7	Concluding remarks . . . . .	23
1.8	Appendix: Model structure . . . . .	25
1.8.1	Running the simulation . . . . .	26
1.8.2	Units used in simulation . . . . .	26
1.8.3	Chlorophyll fluorescence . . . . .	26
1.8.4	Simulations . . . . .	26
<b>2</b>	<b>Manual for NPQ Systems Model</b>	<b>27</b>
2.1	Setup . . . . .	28
2.1.1	Input settings . . . . .	28
2.1.2	Running a simulation . . . . .	40
2.2	Displaying and exporting results . . . . .	42
2.3	Conclusions and future work . . . . .	45
<b>3</b>	<b>Modeling the role of carotenoids and PsbS in qE</b>	<b>46</b>
3.1	Lutein in qE model . . . . .	48
3.2	PsbS dosage effect . . . . .	50
3.3	Light-intensity dependence of model . . . . .	58

3.4	Conclusion . . . . .	61
<b>4</b>	<b>Transient Absorption Spectra of a pH-Sensitive Dye</b>	<b>62</b>
4.1	Introduction . . . . .	62
4.2	Transient absorption measurement . . . . .	65
4.3	Results . . . . .	68
4.4	Discussion . . . . .	69
<b>5</b>	<b>Effect of Bridge on Charge Separation of Molecular Donor-Acceptors</b>	<b>72</b>
5.1	Introduction . . . . .	72
5.2	Methods . . . . .	73
5.2.1	Steady state measurements . . . . .	73
5.2.2	Time-resolved fluorescence . . . . .	74
5.2.3	Transient absorption measurement . . . . .	75
5.3	Results . . . . .	76
5.3.1	Steady state absorption and fluorescence . . . . .	76
5.3.2	Time-resolved measurements . . . . .	76
5.3.3	PDI and HTH components . . . . .	77
5.3.4	Processes in HTH-PDI junctions . . . . .	80
5.4	Effect of bridge properties . . . . .	97
5.4.1	Kinetic scheme . . . . .	97
5.5	Conclusion . . . . .	100
5.6	Fits of fluorescence lifetime data . . . . .	102
<b>6</b>	<b>Reference Tables</b>	<b>103</b>

# Introduction

Effectively exploiting the energy contained in sunlight is a technological challenge with applications to electrical generation, in the form of solar cells; fuel, possibly in the form of biofuels; and food, through improving the efficiency of crops [1]. The research presented in this dissertation focuses on understanding the regulation of energy contained in excited electronic states of molecules, both in natural photosynthesis and in artificial systems.

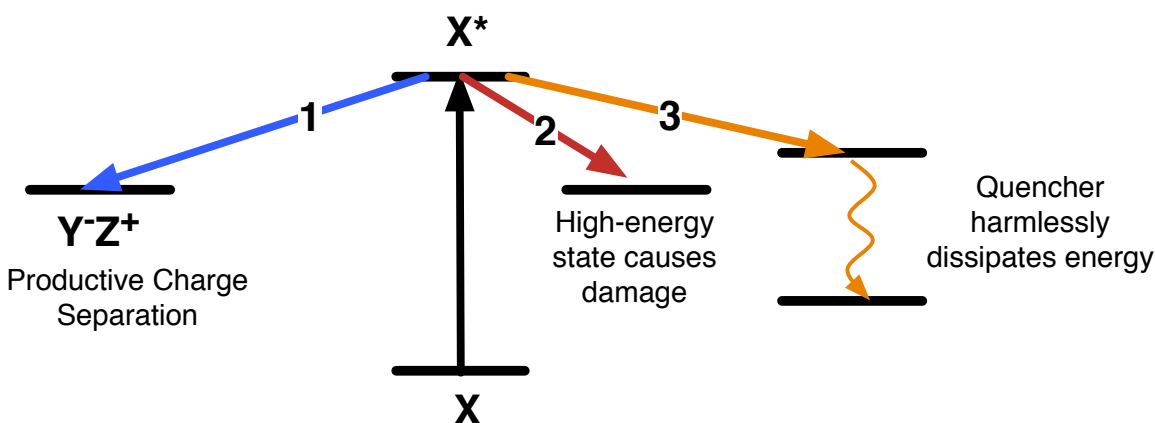


**Figure 1:** Pathways in a light harvesting device.

Figure 1 shows a schematic of the relaxation pathways of an excited state in a photovoltaic system. This system could be either natural, as photosynthesis is driven by photo-induced electron transfer across a lipid membrane, or artificial, as in a solar cell device where charges are separated on two different electrodes. Pathway 1 represents photo-induced electron transfer, which is a first step to a productive harvesting of charges. In photosynthesis, pathway 1 corresponds to electron transfer across the thylakoid membrane in the photosynthetic reaction center, which is the location of primary charge separation [2]. In solar cells, pathway 1 corresponds to overall power conversion efficiency of a solar cell. Improving this power conversion efficiency is for the widespread commercialization of photovoltaics [3]. Chapter 5 of this dissertation addresses ways of improving the initial rate of photoinduced charge separation between a donor and acceptor by studying the effect of the bridge with which the donor and acceptor are joined.

Pathway 2 corresponds to pathways that lead to damage and that eventually inhibit pathway 1. The exact mechanisms of such inhibition are an ongoing topic of research in both

---

photosynthesis [4, 5, 6, 7, 8] and solar cells[9, 10, 11], but it is clear that both natural and artificial light harvesting systems can be damaged as a result of absorbing light for driving pathway 1. In situations where the rate of light absorption exceeds the capacity for charge separation and subsequent extraction of the energy in separated charges, the yield of pathway 1 can be saturated, which creates an undesirable situation in which the destructive yield of pathway 2 is higher than the productive yield of pathway 1.

To alleviate the detrimental effect of pathway 2, photosynthetic organisms have evolved feedback mechanisms that regulate light harvesting in fluctuating light conditions [12, 13]. The quenching mechanisms are collectively called nonphotochemical quenching (NPQ) because they quench excitation energy without doing photochemistry that leads to productive photosynthesis [14, 15, 16]. NPQ manifests itself as a third pathway that rapidly and safely quenches excited states, reducing the destructive yield of pathway 2. This dissipation process is depicted as pathway 3 in Figure 1. In order for the presence of pathway 3 to improve the overall performance of the device, the availability of pathway 3 must be activated when needed and inactivated when it is no longer needed to avoid wasting energy that could be directed to pathway 1.

The regulatory apparatus of quenching natural photosynthesis has evolved to be beneficial at regulating quenching pathways. Several experiments provide evidence for the effectiveness of this regulatory pathway. Plants that are limited in their ability to perform NPQ experience greater inhibition of their oxygen-evolving complex after high-light illumination [13], produce smaller plants when grown with a single short burst of intense light every morning [17], and produce fewer seeds when grown in natural and fluctuating light [12]. In order to quantify the regulation of the most rapidly-reversible component of NPQ, I developed a mathematical model of differential equations to describe this regulation. The model is presented in Chapter 1. To facilitate the use of this model by other people, I developed a graphical user interface (GUI) that can run the model. Chapter 2 consists of a manual for this GUI. Chapter 3 develops a model to describe the observed dependence of NPQ on the pigments lutein and zeaxanthin and the protein PsbS. This model provides a basis for testing hypotheses of qE mechanism and investigating the components and structure of the regulation of light harvesting.

To my knowledge, the type of feedback regulation that is present in photosynthetic organisms has not been developed to date in functional solar cell devices. Efforts in this direction are discussed in reference [18] and Chapter 4 of this dissertation.

# Chapter 1

## A Model of Rapidly-Reversible Nonphotochemical Quenching

Adapted from *Proceedings of the National Academy of Sciences*, vol. 109, issue 39, p. 15757-15762.

### Contents

---

<b>1.1</b>	<b>Introduction</b>	<b>4</b>
<b>1.2</b>	<b>Mathematical model</b>	<b>7</b>
1.2.1	pH-regulated quenching of excited chlorophyll	7
<b>1.3</b>	<b>Description of modules</b>	<b>10</b>
1.3.1	Energy transfer within PSII	10
1.3.2	Electron transfer chain after PSII	10
1.3.3	Luminal buffering and ion motion	11
1.3.4	Activation of ATP synthase	13
<b>1.4</b>	<b>Comparison with PAM fluorescence</b>	<b>14</b>
1.4.1	Extracting NPQ from PAM measurements	14
1.4.2	PAM simulation	15
<b>1.5</b>	<b>Model parameters</b>	<b>16</b>
<b>1.6</b>	<b>Results and discussion</b>	<b>18</b>
1.6.1	qE as a feedback loop	20
<b>1.7</b>	<b>Concluding remarks</b>	<b>23</b>
<b>1.8</b>	<b>Appendix: Model structure</b>	<b>25</b>
1.8.1	Running the simulation	26
1.8.2	Units used in simulation	26
1.8.3	Chlorophyll fluorescence	26

## 1.1 Introduction

Photosynthetic organisms are highly efficient at absorbing photons and transferring energy to a reaction center, where charge separation takes place. However, when the rate of energy consumption by the reaction center is slower than the rate of energy transfer to the reaction center, long-lived chlorophyll excited states build up in the Photosystem II (PSII) antenna. These long-lived states present a significant hazard to the organism because the energy contained in excited chlorophyll is sufficient to generate singlet oxygen, which is highly reactive and can break bonds in the proteins essential for photosynthesis [4]. Because sufficient light harvesting is necessary for fueling growth, but too much is harmful, plants must balance light harvesting and photoprotection. Achieving this balance is especially challenging when light intensity rapidly fluctuates between levels that limit photosynthesis and levels that exceed the plant's capacity for photosynthesis [12].

The mechanisms of regulated dissipation of excess absorbed energy in the PSII antenna are collectively known as nonphotochemical quenching (NPQ) [14]. NPQ mechanisms dissipate excitation energy harmlessly as heat, reducing the extent of photoinhibition [13]. There are multiple mechanisms for NPQ and these mechanisms respond on different timescales [14]. The most rapid component of NPQ is called qE, and it responds to fluctuations in light intensity on the timescale of seconds to minutes [16, 19].

The qE quenching pathway is activated by a decrease in the pH of the thylakoid lumen [14]. The low pH of the lumen activates qE by protonating the proteins PsbS [20] and violaxanthin deoxidase (VDE) [21, 22], and possibly other LHC proteins [23, 24]. VDE goes on to convert the carotenoid violaxanthin to zeaxanthin in the xanthophyll cycle, which includes the intermediate antheraxanthin [25]. The presence of zeaxanthin and the xanthophyll lutein, along with PsbS, is necessary for full expression of qE *in vivo*. In addition to the protonation of PsbS and the formation of zeaxanthin, the PSII antenna undergoes a rearrangement that facilitates quenching of chlorophyll excitations [26, 27]. While many of the essential components of qE are known, the exact sequence of events that lead to quenching remains an area of active research [26, 27, 28, 29, 30].

qE is typically observed by Pulse Amplitude Modulation (PAM) fluorescence, which monitors changes in the chlorophyll fluorescence yield [31]. There is a great deal of PAM data showing altered qE dynamics in plants that have been genetically altered or chemically treated with various inhibitors. Interpreting the effects of mutations and chemical treatments on the lumen pH and on the dynamics of qE is difficult because a large number of interrelated processes occur on a large range of timescales (from picoseconds to minutes) in the thylakoid membrane. The ability to quantitatively evaluate and predict the expression of qE in plants would enable the testing of different hypothesized models of the qE mechanism.

Beyond testing hypotheses, a quantitative understanding of qE would provide significant benefits. Numerous experimental studies have shown that qE enhances various metrics of plant vitality in variable light conditions and does not impair the plant's ability to thrive in

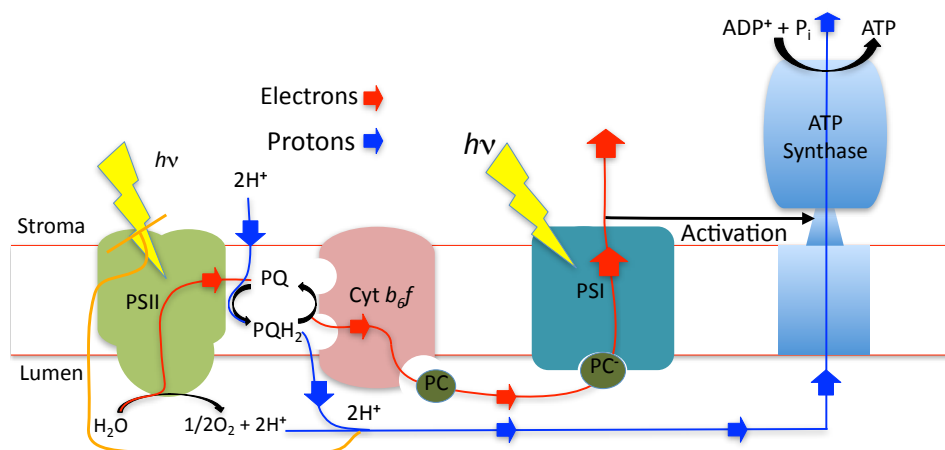


**Figure 1.1:** Schematic of components described in the model. For more detailed schematics, see reference [32]. Nonphotochemical quenching occurs in PSII.

constant light conditions [12, 13, 17, 33]. Because qE does not seem to negatively affect the performance of plants in natural conditions, the feedback loop that activates qE must be regulated to confer a net benefit to the plant. Understanding the control parameters governing this feedback loop would provide useful information for both optimizing photosynthesis [34, 35, 36] and for designing artificial systems that are robust in fluctuating light conditions.

Although there are numerous models of chlorophyll fluorescence kinetics [37, 38, 39], of ion transport in the lumen [40], of electron and ion transport in entire thylakoids [41], and of zeaxanthin-dependent NPQ [42], to our knowledge there are no models that simulate the kinetics of the appearance and disappearance of qE at low and high light intensities. Modeling qE at a range of light intensities is important for quantifying the benefit that qE confers to plants in fluctuating light conditions. We have developed a mathematical model that describes the kinetics of processes that directly and indirectly affect the lumen pH. This model enables us to simulate measurements of the induction and decay of qE with enough accuracy that the model can serve as a starting point for a computational assessment of the role of the components of qE in balancing the organism's needs for light harvesting and photoprotection.



## 1.2 Mathematical model

A general schematic of the model is shown in Figure 1.1. Our model consists of 26 nonlinear differential equations describing the evolution of variables involved in photosynthetic light harvesting for a given intensity of actinic light. The equations are of the form

$$\dot{\mathbf{X}}(t) = F(\mathbf{X}; p) + G(I(t); p) \quad (1.1)$$

where  $\mathbf{X}$  is a vector that contains all the variables included in our model,  $p$  is a vector containing all the model parameters, and  $I$ , the light intensity, is the input.  $F(\mathbf{X}; p)$  is the set of differential equations that describes how the evolution of the components of  $\mathbf{X}$  depends on the components themselves, and  $G(I(t); p)$  is a function describing how the evolution of the components of  $\mathbf{X}$  depends on the light intensity. An illustration of the components of the model is shown in Figure 1.2A.

**Table 1.1:** Model components and references.

Module	references (if available)
$(F_1)$ light harvesting	[38, 43, 44, 34]
$(F_2)$ qE quenching	[45, 13]
$(F_3)$ electron transfer through plastoquinone pool	[38]
$(F_4)$ plastoquinol oxidation at cytochrome $b_6f$	[40, 45]
$(F_5)$ electron transfer through plastocyanin and PSI on to ferredoxin	[46]
$(F_6)$ reduction of the stroma by ferredoxin	-
$(F_7)$ activation of proton efflux via the ATP synthase enzyme	-
$(F_8)$ proton and ion dynamics in the lumen and stroma	[40]

We have separated the processes that describe the time-evolution of the components of  $\mathbf{X}$  into eight modules, which are described in Table 1.1. These modules are designated  $F_1$  through  $F_8$ , each of which contains a set of differential equations corresponding to a particular process. The modules are  $(F_1)$  light harvesting,  $(F_2)$  qE quenching,  $(F_3)$  electron transfer through the plastoquinone pool,  $(F_4)$  plastoquinol oxidation at cytochrome  $b_6f$ ,  $(F_5)$  electron transfer through plastocyanin and PSI on to ferredoxin,  $(F_6)$  reduction of the stroma by ferredoxin,  $(F_7)$  activation of proton efflux via the ATP synthase enzyme, and  $(F_8)$  proton and ion dynamics in the lumen and stroma. We consider modules  $F_3$ - $F_8$  to be the ‘‘plant’’ which converts excitation energy to ATP, and we consider  $F_1$  to be the regulated input to the plant and  $F_2$  (qE) to be the feedback regulator to  $F_1$ .

In total the model contains 78 parameters, most of which were taken from the literature. The values of parameters in modules  $F_3$ ,  $F_4$ ,  $F_5$ , and  $F_8$ , were not modified from literature values. The values of parameters used in the remaining modules were adjusted to some extent. An overall schematic of the model is shown in Figure 1.2A, and details of the light harvesting and quenching models are shown in Figure 1.2B and C.

### 1.2.1 pH-regulated quenching of excited chlorophyll

The evolution of the number of excited chlorophylls in the PSII antenna is given by

$$\begin{aligned}
\frac{d[Chl^*]}{dt} = & \sigma I - [Chl^*](k_{T,RCO}[RCO] + k_{T,RCC}[RCC]) \\
& + k_{NR} + k_F + k_{qE}[Q] \\
& + [P680^*](k_{R,RCO}[RCO] + k_{R,RCC}[RCC])
\end{aligned} \tag{1.2}$$

where  $[Chl^*]$  is the number of excited chlorophylls associated with one PSII core;  $\sigma$  is the absorption cross section of one PSII;  $[RCO]$  and  $[RCC]$  are the fractions of RCs that are open ( $Q_A$  oxidized) and closed ( $Q_A$  reduced), respectively; the rates  $k_{T,RCO}$  and  $k_{T,RCC}$  are the rate constants associated with energy transfer from the light harvesting antenna to the special pair of chlorophylls in the reaction center (P680) when the reaction centers are open and closed, respectively;  $k_{R,RCO}$  and  $k_{R,RCC}$  are the rate constants associated with energy transfer from excited P680 back to the antenna for open and closed reaction centers [47];  $k_F$  is the rate constant for spontaneous emission (fluorescence) by an excited chlorophyll;  $k_{NR}$  is a rate constant for other nonradiative decay processes such as intersystem crossing and internal conversion; and  $k_{qE}$  is the rate constant associated with quenching by a qE quencher. We assume  $k_{qE}=1/330$  ps, based on the two PsbS-dependent lifetimes in reference [13]. Equation 1.2 contains numerous simplifications which are discussed in section 1.3.1.

The quenching due to qE is modulated in equation 1.2 by the quantity  $[Q]$ , which is the fraction of quenching sites in the PSII antenna that are able to dissipate excitation energy by qE. We assume that for a quenching site to be present, it is necessary to have an activated PsbS protein and a de-epoxidized xanthophyll in photosystem II. We base this assumption on the facts that 1) the *npq4* mutant, which lacks PsbS, has no rapidly-reversible NPQ *in vivo* [20] and 2) inhibition of the violaxanthin deepoxidase enzyme, either chemically with dithiothreitol [21] or genetically by removing the gene for it [22], results in decreased levels of rapidly-reversible NPQ.

A working model in which both PsbS and a de-epoxidized xanthophyll is required for qE *in vivo*[45] assumes that the protonation of VDE and PsbS are uncorrelated with each other, and so the fraction of PSII that contain both elements needed for quenching can be written as

$$[Q] = F_{PsbS} \cdot [PsbS]^* \cdot ([Z] + [A]) \tag{1.3}$$

where  $[PsbS]^*$  is the fraction of PSII with a protonated PsbS and  $[Z]$  ( $[A]$ ) is the fraction of xanthophyll binding sites in PSII that contain zeaxanthin (antheraxanthin) in a site able to perform qE. Although this expression is a simplification of the exact nature of qE quenching, since some VDE-independent NPQ is present in plants [48, 49], it serves as a reasonable starting point for mechanistically modeling the experimental observations of PsbS-dependent NPQ.

The active forms of PsbS and VDE are both triggered by a low lumen pH, but with different  $pK_a$ s and Hill coefficients. The  $pK_a$  determines the pH values at which 50% of the proteins are protonated, and can be thought of as a “set point” level at which the pH-triggered protein is activated. The Hill coefficient determines the steepness of the pH-dependence of the protein in transitioning from the fully active form to the fully inactive form. We assume

that PsbS is in equilibrium with the lumen and that the activation of PsbS into a quenching-active state following protonation happens instantaneously, giving the following expression for active PsbS ( $[PsbS]^*$ ):

$$[PsbS]^* = \frac{[H^+]^{n_p}}{K_p^{n_p} + [H^+]^{n_p}} \quad (1.4)$$

where  $K_p$  and  $n_p$  are the  $pK_a$  and Hill coefficient of PsbS protonation. To calculate the VDE-dependent component [21], we also assume that the activation of VDE by low lumen pH happens instantaneously. The expression we use for the effective rate constant of VDE ( $k_{VDE}^*$ ) is

$$k_{VDE}^* = k_{VDE,max} \frac{[H^+]^{n_v}}{K_v^{n_v} + [H^+]^{n_v}} \quad (1.5)$$

where  $k_{VDE,max}$  is the rate constant of fully protonated VDE activity, and  $K_v$  and  $n_v$  are the  $pK_a$  and Hill coefficient of VDE protonation. We take the maximum rate of VDE activity to be  $4 \times 10^{-2}$  de-epoxidation events per second, which corresponds to a timescale of one de-epoxidation event every 20 seconds if there were one VDE enzyme present per PSII. We assume that, under the conditions used for this work, zeaxanthin epoxidase (ZE) has a fixed concentration and the rate of zeaxanthin epoxidation is constant. This assumption may need to be revised in the future as more information regarding the regulation of ZE emerges [50]. The rate of zeaxanthin epoxidase is 10 to 300 times slower than that of violaxanthin deepoxidase [45], so we assumed a rate of  $4 \times 10^{-4}$  epoxidation events per second. With these assumptions, the concentrations of zeaxanthin and antheraxanthin in the PSII antenna are given by

$$\begin{aligned} [A(t)] &= \int_0^t k_{VDE}^*(t') [V(t')] + k_{ZE}(t') ([Z(t')] - [A(t')]) dt' \\ [Z(t)] &= \int_0^t k_{VDE}^*(t') [A(t')] - k_{ZE}(t') [Z(t')] dt' \end{aligned} \quad (1.6)$$

where  $[V] = 1 - [Z] - [A]$  is the fraction of qE-relevant xanthophyll binding sites occupied by violaxanthin.

Plants with elevated levels of PsbS have shown elevated levels of qE [13], indicating that not all possible qE sites are modulated by wild-type levels of PsbS. To account for this effect, we have incorporated an effective PsbS dosage factor,  $F_{PsbS}$ , which can be interpreted as the fraction of potential qE sites that are modulated by PsbS [13, 51]. For wild type, we set this dose to be 0.6, because that gave the best agreement with experimental data.

For simplicity, we assume that there is only one site of qE in PSII and that it is accessible to all the chlorophylls within PSII, with the probability of quenching being proportional to the rate  $k_{qE}$ . We do not incorporate a microscopic model of the quenching process, but rather assume that quenching occurs infinitely fast and therefore that quenching sites are always “open” (in contrast with reaction centers, which are closed when  $Q_A$  is reduced).

These assumptions are necessary at this point for simplicity, but it will be important in the future to systematically address the effect of multiple quenching sites and different quenching mechanisms [28, 29, 30] on the predictions of the model.

In order to compare the predictions of the model with experimental measurements on intact leaves, the quantum yield of chlorophyll fluorescence was simulated by assuming that the quantum yield is related to variables and parameters in equation 1.2 by

$$\Phi_F = \frac{k_F}{k_{T,RCO}[RCO] + k_{T,RCC}[RCC] + k_O + k_F + k_{qE}[Q]}. \quad (1.7)$$

Quantifying the extent of qE expression *in vivo* requires knowledge of the lumen pH at each point during the light-adaptation process. To calculate lumen pH, it is necessary to account for the rate of protons entering the lumen, the rate of protons leaving the lumen, and the buffering capacity of the lumen. These processes are interrelated because they all affect and are affected by the proton motive force and by the concentration of mobile ions that move across the thylakoid membrane [40]. The lumen pH is also affected by the conductivity of ATP synthase, which is activated by linear electron flow through the thioredoxin system [52]. Details pertaining to the calculation of lumen pH are given in section 1.3.3. Incorporating a rate for activation of ATP synthase was necessary for simulating qE at low light intensities, and is described in section 1.3.4.

## 1.3 Description of modules

### 1.3.1 Energy transfer within PSII

Excited chlorophylls are quenched by energy transfer to the RC, by intrinsic decay processes, and by regulated NPQ pathways, as illustrated in Figure 1.2 B. Our model assumes a “lake” model of energy transfer in which quenching sites are shared between all excited chlorophylls [53], and that excitation equilibrates within PSII instantaneously before any photochemical or nonphotochemical quenching processes can take place. This assumption is a simplification because the timescale of energy transfer through the PSII antenna [54], as well as the exact location of the quenching site, will affect the relative yields of light harvesting and quenching energy. Nonetheless, because neither the exact nature of energy transfer through the PSII antenna [55] nor the exact site of qE quenching [19] are definitively known, our assumption is a necessary initial assumption and provides a framework for testing different models of energy transfer.

### 1.3.2 Electron transfer chain after PSII

For modeling energy transfer through PSII, electron transfer in the reaction center and through the plastoquinone pool, and plastoquinone reoxidation at cytochrome  $b_6f$ , we have followed previous models [38, 40]. A schematic is shown in Figure 1.3. One notable modification is that we assumed that undocking of reduced plastoquinol and the docking of oxidized plastoquinol into the  $Q_B$  binding site had reverse rates that occurred at 10% of the rate of the

forward reaction. We did this to improve agreement between simulated and measured  $Q_A$  oxidation state, typically measured as  $1 - qP$  [53], at a range of light intensities, although accurate simulation of the oxidation state of  $Q_A$  at a range of light intensities requires further work. Following reference [45], we assumed that the rate of plastoquinol oxidation at cytochrome  $b_6f$  slowed down at lower pH values, with a  $pK_a$  of 5.8 and Hill coefficient of 1.2, causing plastoquinol oxidation to be slower at lower pH. The  $pK_a$  value we used (5.8) is lower than the  $pK_a$  value used in Takizawa et al, which was 6.6, but is closer to earlier estimates of the pH-dependence of plastoquinol oxidation [40]. After passing through cytochrome  $b_6f$ , electrons are transferred to plastocyanin, then undergo another photo-induced electron transfer through the PSI reaction center, and finally to ferredoxin. Because calculating the redox state of the stroma [56] is beyond the scope of our current model, we assume that ferredoxin is rapidly re-oxidized with a single rate constant.

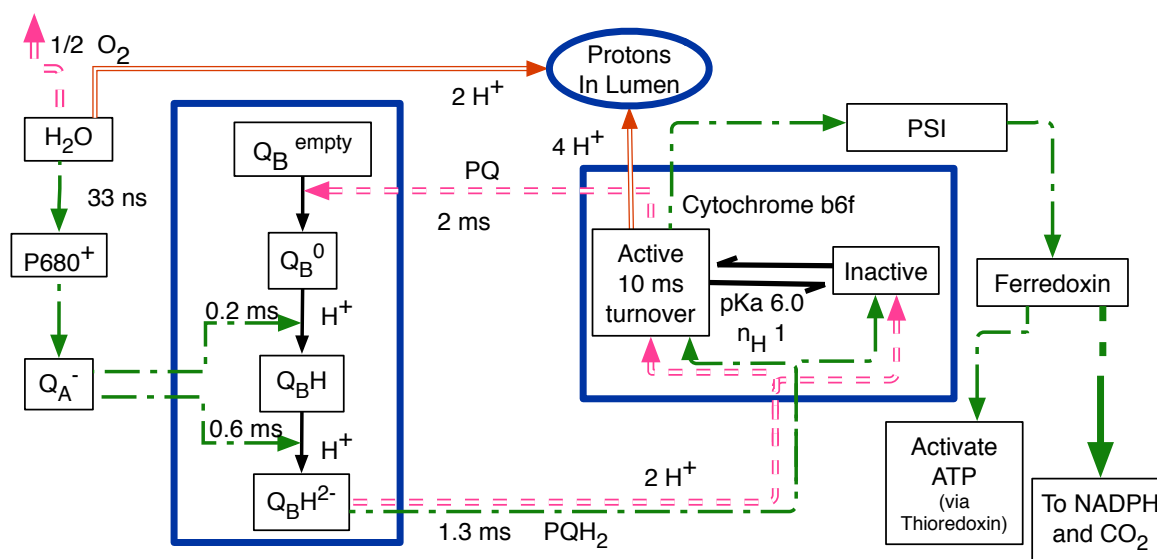
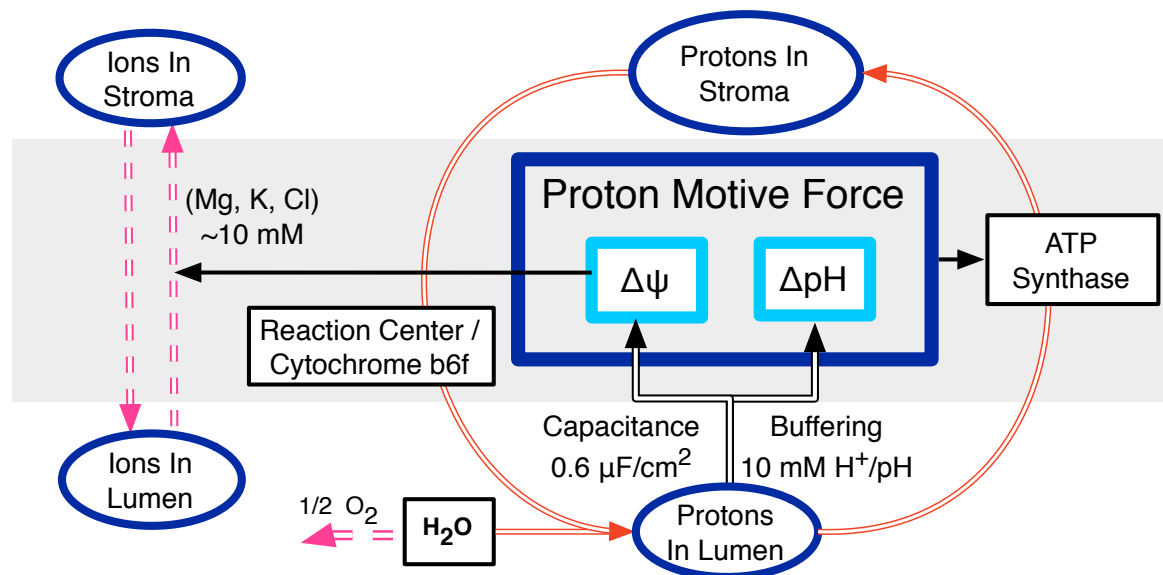


Figure 1.3: Schematic of proton and electron flow in photosynthesis.

### 1.3.3 Lumenal buffering and ion motion

To simulate the lumen pH, which triggers  $qE$ , it was necessary to calculate the rate of protons entering the lumen, the rate of protons leaving the lumen, and the buffering of protons inside the lumen. A schematic of these processes is given in Figure 1.4. Protons enter the lumen at two points during linear electron flow: 1) water splitting at PSII and 2) plastoquinol oxidation at the cytochrome  $b_6f$  complex. Protons leave the lumen through ATP synthase, which converts the energy contained in the proton gradient across the thylakoid membrane to a phosphate bond in the molecule ATP. Overall, under conditions of linear electron flow, three protons enter the lumen for each electron transferred through the PSII reaction center [46]. These protons contribute to the  $pmf$  in two ways [40]: 1) by creating an electrical potential that drives positive charges to the outside of the lumen and 2) by creating a pH gradient that

provides a diffusive potential for protons to exit the lumen. This parsing of the *pmf* into an electric field and a diffusion potential depends on the buffering capacity of the lumen and on the motion of charged ions across the thylakoid membrane [40].



**Figure 1.4:** Schematic of the dynamics affecting lumen pH. The grey box represents the thylakoid membrane. Protons pumped into the lumen at PSII and cytochrome  $b_6f$  are buffered with a buffering capacity of 10 mM  $H^+/pH$ .

The buffering of protons in the lumen has been studied in great detail in isolated chloroplasts [57] and a detailed mathematical model for luminal buffering has also been developed [37], which indicates that the luminal buffering capacity increases at decreasing pH. For simplicity, we use a constant buffering capacity of 30 mM protons per  $\Delta pH$  [40]. Nonetheless, incorporating a more accurate model of lumen buffering may be important in the future to achieve good agreement with a wider set of data, especially as the model is extended to incorporate plants in stressed conditions in which the lumen pH may be lowered past that of healthy plants.

The relationship between protons entering the lumen and the lumen pH also depends on the motion of ions in and out of the lumen. We have assumed that a significant portion of the proton motive force that drives ATP synthase is stored in the form of an electric field gradient across the thylakoid membrane, which occurs when the ionic strength of the lumen is low (5 mM) [40]. In the absence of a *pmf* or electric field, which is what we assume the state of the system to be in the dark, the ion concentration of stroma and lumen are in equilibrium. In the light, the electric field formed by proton pumping exerts a driving force on the mobile ions within the lumen, which dissipate this electric field over time [40]. Consequently, the fraction of the *pmf* that is stored as an electric field decreases over time as ions move across the thylakoid membrane and dissipate this electric field. This dissipation of the electric field increases the relative fraction of the *pmf* that must be stored as a  $\Delta pH$  between lumen and stroma, and therefore lowers the lumen pH. The equations describing

this process are taken from reference [40]. We use a concentration of 10 mM for the initial concentration of lumenal and stromal ion concentrations and assume that the stromal ion concentration does not change.

We assume that the volume of lumen per PSII is  $6.7 \times 10^{-21}$  liters and that the ratio of lumen volume to surface area of the thylakoid membrane is  $8 \times 10^{-10}$  liters/cm<sup>2</sup> [40]. Because we have assumed that the proton motive force (*pmf*), which drives ATP synthesis, arises from both an electric field gradient ( $\Delta\psi$ ) and  $\Delta$ pH component, our model is consistent with recent views that sufficient *pmf* for ATP synthesis and qE can be attained at a moderate lumen pH [58].

### 1.3.4 Activation of ATP synthase

Accurately modeling the conductivity of ATP synthase is challenging because there are numerous factors regulating ATP synthesis[59]. One possible approach is to assume, as in reference [40], that the ATP synthase has a constant proton conductivity. The problem with such an approach is that it does not incorporate the effect of the activation of the Calvin-Benson cycle by linear electron flow through the thioredoxin system [52], and as a result will overestimate the lumen pH in the initial few minutes when plants are moved from dark to light, especially in situations when the actinic light intensity does not saturate linear electron flow. At low light intensities, a transient qE appears within tens of seconds after the onset of illumination and disappears after several minutes, most likely because the ATP synthase enzyme is initially inactive, and its activity is activated along with the ATP-consuming reactions of the Calvin-Benson cycle [60].

To account for this transient qE without building a complex model of ATP synthase activation and ATP consumption, we have chosen to modulate the proton conductivity of ATP synthase with an effective average of the many processes that affect the rate of proton flux through ATP synthase. To model the rate of protons leaving the lumen through ATP synthase, we use the equation

$$H_{\text{out}} = g_{H^+} \times pmf \times F_{ATP} \quad (1.8)$$

where  $g_{H^+}$  is the conductivity of ATP synthase, for which we use a value of  $10^{-9}$  mol protons/Volt/cm<sup>2</sup>/s, *pmf* is the proton motive force, and  $F_{ATP}$  is a unitless number between 0 and 1 that modulates the conductivity of ATP synthase.  $F_{ATP}$  increases with linear electron flow, and the rate of increase of  $F_{ATP}$  is a single rate representing all reactions that affect the rate of proton flux through ATP synthase. In the model  $F_{ATP}$  evolves according to the equation

$$\frac{dF_{ATP}}{dt} = k_{ATPAct}[Fdxr](1 - F_{ATP}) - k_{ATPInact}F_{ATP}$$

where  $[Fdxr]$  is the fraction of the total ferredoxin in the stroma that is reduced. In fact, the factors controlling the rate of proton flux through ATP synthase are numerous and not fully understood, and include the activation of ATP synthase itself as well as the activation of several enzymes in the Calvin-Benson cycle that affect the consumption of ATP [52]. Because

the detailed dynamics of the carbon reactions and ATP synthase regulation are outside the scope of our model, we have chosen to capture the effect of the changing proton conductivity of ATP synthase during acclimation from dark-adapted to light-adapted state with a single rate constant,  $k_{ATPAct}$  and a reverse rate of inactivation,  $k_{ATPInact}$ . We note that this simplification reduces the applicability of our model to situations in which plants are stressed by, for example, cold or drought, though qE does play an important photoprotective role in these situations [61]. More work is needed in order to be able to apply this model to such situations, where there may be significant potential for improving photosynthetic yields.

### Proton to ATP ratio and cyclic electron flow

Cyclic electron flow (CEF) around PSI is an important process that affects qE in *Arabidopsis* [62]. However, details of the regulation of cyclic electron flow are not fully understood and are an area of current investigation [63]. As a result, we have chosen to omit this process from our model and to compensate for its absence by altering the proton-to-ATP ratio of ATP synthase. Experimental and theoretical work has suggested that a major role of cyclic electron flow is to set the ratio of ATP to NADPH production to be equal to 3:2, which is the ratio needed for the carbon reactions [64]. It is thought that 14 protons are translocated through ATP synthase to form 3 molecules of ATP, causing the ratio of ATP to NADPH production to be lower than the 3:2 ratio needed for carbon reactions. If, instead, the ratio of protons to ATP produced by ATP synthase were 12:3, then ATP and NADPH production would be balanced with the demands of the Calvin-Benson cycle [64]. If the role of CEF is indeed to balance the ratio of ATP and NADPH production with the ratio for their consumption, then assuming a proton to ATP ratio of 12:3 should lead to a more accurate estimate of lumen pH than if the effect of CEF were ignored completely. In our modeling, we have assumed that the proton-to-ATP ratio of ATP synthase enzyme is 12:3, which gives a 3:2 ratio of ATP to NADPH production.

## 1.4 Comparison with PAM fluorescence

### 1.4.1 Extracting NPQ from PAM measurements

In a PAM fluorescence measurement, the data have been normalized to the initial dark-adapted fluorescence state  $F_o$  [31]. While the plant is in the dark, an intense pulse of light measures the fluorescence yield of the plant when all photosystem II RCs are saturated, determining the level of fluorescence (denoted  $F_m$ ) before NPQ pathways have turned on. Upon transition from darkness to light, the fluorescence yield of the leaf rapidly increases to a maximal level, then decreases more slowly as the availability of photochemical and NPQ pathways increases. During repeated application of intense pulses (spikes) all reaction centers are fully closed, so the change in fluorescence quantum yield relative to  $F_m$  in the presence of these intense flashes (denoted  $F'_m$ ) is due to the appearance of NPQ pathways. A commonly used expression for total NPQ is  $NPQ = (F_m - F'_m)/F'_m$  [31, 65].

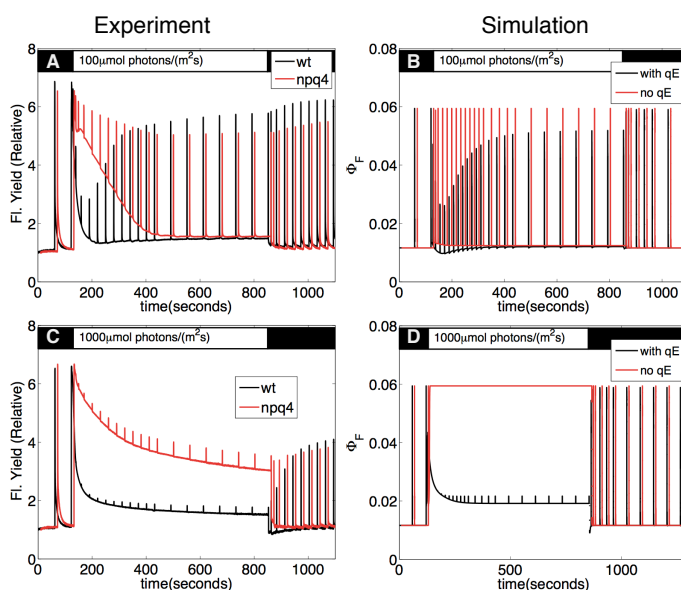


**Figure 1.5:** Measured (A,C) and simulated (B, D) chlorophyll fluorescence yield of *Arabidopsis thaliana* leaves at different light intensities with (black) and without (red) qE. The discrepancy between the *npq4* experiment and the no qE simulation is large because our model does not incorporate slowly reversible components of NPQ. The black bar at the top indicates times when the leaf is in the dark, and the white bar indicates times when the leaf is illuminated by actinic light illumination.

## 1.4.2 PAM simulation

The simulated qE curves shown in Figure 1.9 were obtained from simulations of chlorophyll fluorescence as in the PAM fluorescence experiment [66]. Figure 1.5 shows the measurements (left, A and C) and simulations (right, B and D) of PAM fluorescence traces of dark adapted plants exposed to 100 (Top, A, B) and 1000 (bottom, C,D)  $\mu\text{mol photons m}^{-2}\text{s}^{-1}$ . Although Figure 1.9 shows reasonable agreement between the model and data for qE, the deviation between the model and the full chlorophyll fluorescence trace is much greater. Because the model does not currently incorporate NPQ mechanisms other than qE, the height of the saturating spikes is constant in the simulation of the *npq4* mutant as shown in Figure 1.5 B and D, in stark contrast to the measured data (Figure 1.5 B and D). In particular, the model does not accurately calculate the baseline fluorescence level, denoted  $F_s$ , which is a measure of both photochemical and nonphotochemical quenching [31]. The model calculates that photochemistry is fully saturated at 1000  $\mu\text{mol photons m}^{-2}\text{s}^{-1}$ , leading to a completely flat and saturating fluorescence level in Figure 1.5D. Because of the model's limitations in accurately calculating photochemical quenching, there is some discrepancy between experiment and model in the height of the spikes due to saturating pulses, which is used experimentally to measure the fraction of open reaction centers. However, we note that the trend of increasing height of the spikes as the plant adapts to light, which signifies a reduction in excitation pressure, is reproduced by the modeled activation of ATP synthase by linear electron flow.

Because the chlorophyll fluorescence is simulated according to equation 1.7, the simu-

lated rate of photochemical quenching is determined by the concentration of oxidized  $Q_A$ , independently of the redox state of  $Q_B$  or the PQ pool. In the model we used for electron transfer among quinones [38], the rate of electron transfer from  $Q_A$  to  $Q_B$  is much faster than the rate of downstream electron transfer reactions, and does not directly depend on the redox state of the PQ pool. Because of this, the transition from  $Q_A$  being fully reduced to fully oxidized in the model is much more abrupt than in reality. It is possible that the reason for these discrepancies is due to the fact that the model neglects processes other than electron transfer through PSII that may reduce the PQ pool, such as chlororespiration [67] and cyclic electron flow around PSI. In order to apply this model to incorporate the role of qE at a range of light intensities beyond the two example light intensities presented here, it will be necessary to refine the present model to correctly simulate the photochemistry that determines the dependence of the  $Q_A$  redox state on incident light intensity.

## 1.5 Model parameters

Table 1.2 shows the parameters affecting qE used to generate the simulations shown in these chapter. Many of these values were fitted to achieve good agreement between experiment and data. The pKa and Hill coefficient of PsbS protonation that we used are 6.3 and 3, respectively, which are somewhat different from the values of 6.8 and 1 found by Takizawa et al. [45]. This discrepancy is probably due to the fact that, in Takizawa et al., *in-vivo* estimates of lumen pH derived from measurements of the electrochromic shift were used to fit to steady state NPQ values for various mutants; in this work, we fit NPQ of only the wild-type to dynamic NPQ measurements.

Some parameters that are not directly related to qE were adjusted in the model. Parameters related to energy transfer in PSII were adjusted to keep values of chlorophyll fluorescence yield close to observed of  $F_0$  and  $F_m$ , corresponding to fluorescence yields of dark-adapted plants transitioning to actinic light. The value of the rate of activation of ATP synthase was set to give agreement with the disappearance of qE in wild-type at low light intensities.

To assess the effect of varying parameters on the conclusion of Figure 1.12, which is that

111

**Table 1.2:** Values of parameters affecting qE used in simulations.

parameter	value	explanation and source
$k_{VDE,VA}$	$4 \times 10^{-2} s^{-1}$	rate of de-epoxidation from violaxanthin to antheraxanthin [60]
$k_{VDE,AZ}$	$4 \times 10^{-2} s^{-1}$	rate of de-epoxidation from antheraxanthin to zeaxanthin (fitted)
$k_{ZE}$	$4 \times 10^{-4} s^{-1}$	rate of violaxanthin and antheraxanthin epoxidation (fitted)
pKa VDE	6.0	pKa of VDE activation [45, 25]
nVDE	6	Hill coefficient of VDE activation (fitted)
pKa of PsbS	6.4	pKa of PsbS activation (fitted)
nPsbS	3	Hill coefficient of PsbS activation (fitted)
PsbS Dose	0.6	Fraction of possible quenching sites that are triggered by PsbS (fitted)

qE does not change the lumen pH, we plotted the lumen pH in the presence and absence of qE for a range of ATP synthase conductivities and rate of ATP synthase activation in Figure 1.6. For all these parameter values, the lumen pH was not affected by qE. Varying the conductivity of ATP synthase did affect the redox state of  $Q_A$  (Figure 1.7 A) and of the plastoquinone pool (Fig 1.7B). The fact that the lumen pH appears to be unchanged is likely due to the fact that the rate limiting step for linear electron flow occurs at the cytochrome  $b_6f$  complex [68].

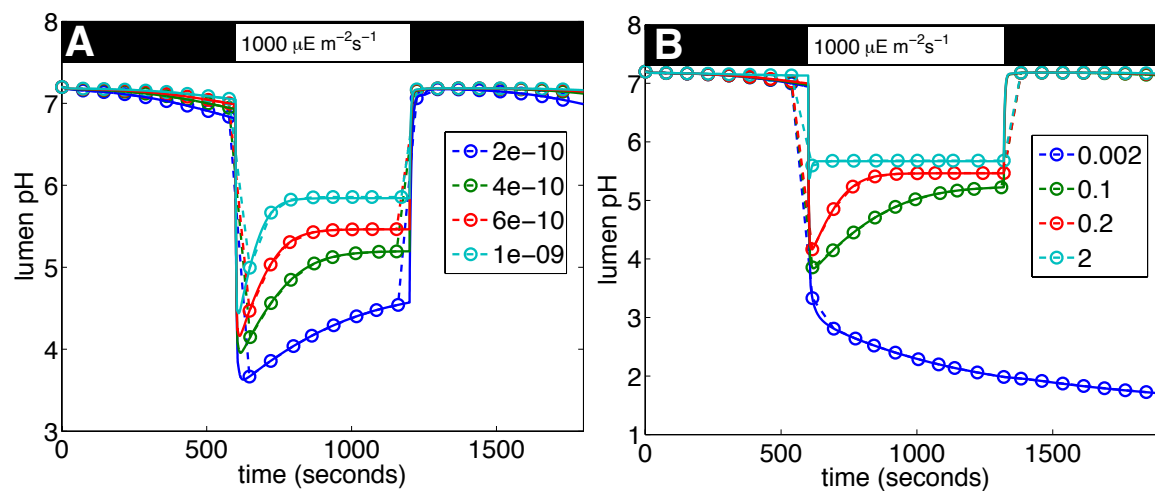


**Figure 1.6:** Simulated lumen pH values with qE (circles with dashes) and without qE (lines) quenching for different values of A) ATP conductivity, in units of mol protons/Volt/cm<sup>2</sup>/s and B) rate of activation of ATP synthase through ferredoxin, in units of Active ATP synthase/PSII/second/reduced Ferredoxin. The rate of ATP synthase de-activation was kept constant.

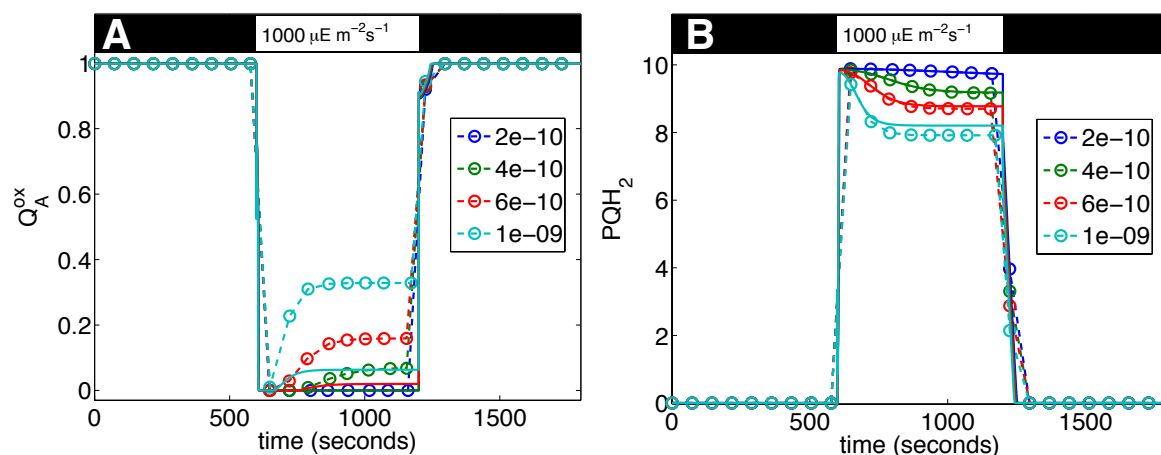


**Figure 1.7:** Simulated A)  $Q_A$  and B)  $PQH_2$  values with qE (circles with dashes) and without qE (lines) quenching for different values of ATP synthase conductivity, in units of mol protons/Volt/cm<sup>2</sup>/s

## 1.6 Results and discussion

Figure 1.8 shows an experimental pulse amplitude modulation (PAM) fluorescence [31] trace for *Arabidopsis thaliana* wild-type (*wt*) and *npq4* mutant, which lacks PsbS, measured at an actinic light intensity of  $1000 \mu\text{mol photons m}^{-2}\text{s}^{-1}$ . The amount of total NPQ in each plant, quantified using the formula  $NPQ = (F_m - F'_m)/F'_m$ , is shown in Figure 1.8B (the formula is explained in section 1.4.1). The rapidly reversible component of NPQ (qE) is absent in the *npq4* mutant but a substantial slowly reversible NPQ still accumulates that accounts for more than 25% of the total NPQ observed in *wt*. Figure 1.8C shows the difference in NPQ between the wild-type and *npq4* mutant. This difference is a measure of the NPQ due to qE and is the experimental observable to which we fit our model. Comparing simulations of models of qE directly to a PAM trace is not appropriate at all light intensities because a substantial fraction of NPQ is not due to qE but is due to other, slowly reversible mechanisms. These mechanisms include qI, which relates to inhibition of PSII, qT, which is quenching due to state transitions between PSII and PSI, [14] and qZ, which is zeaxanthin-dependent but PsbS-independent quenching in the PSII antenna [69]. These slower NPQ components are all present in the *npq4* mutant, as shown in Figure 1.8A and B, suggesting that the difference in NPQ between *npq4* and wild type is a reasonable estimate of qE. A concern is that *npq4* would have more qI quenching than wild type due to a reduced ability to protect PSII from photoinhibition [13], but the short duration of illumination presented here (<15 minutes) only induces a small (<0.5) amount of excess NPQ ascribed to qI in *npq4* compared to wild type.

Figure 1.9 compares the experimental values of qE with those simulated by the model at light intensities of 100 (A) and 1000 (B)  $\mu\text{mol photons m}^{-2}\text{s}^{-1}$ , for the same set of parameters. At 100  $\mu\text{mol photons m}^{-2}\text{s}^{-1}$ , qE rises to a value of 0.5 within 100 seconds of illumination, then relaxes to a smaller value within 400 seconds. When actinic light is turned off, the small steady-state qE rapidly relaxes. The model reproduces the rapid rise of qE, as

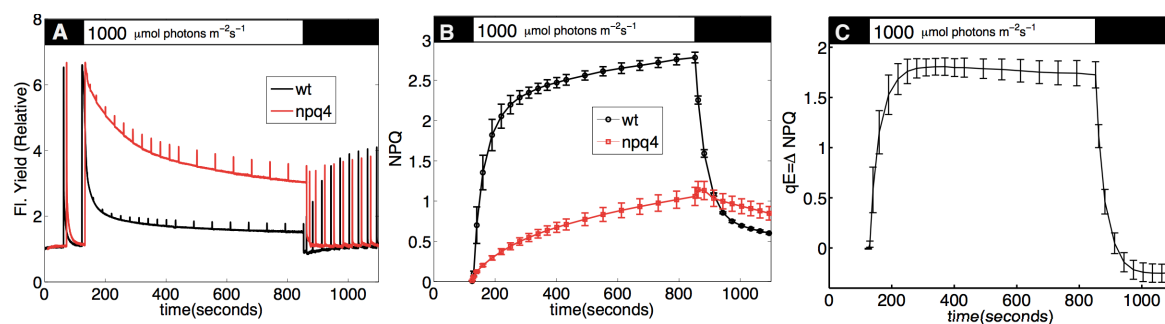


**Figure 1.8:** A) Pulse Amplitude Modulation (PAM) traces of wild type and *npq4 Arabidopsis thaliana* leaves at  $1000 \mu\text{mol photons}/\text{m}^2/\text{second}$ . B) NPQ in wild type and mutant, calculated using the formula  $\text{NPQ} = (\text{Fm} - \text{Fm}')/\text{Fm}'$ . C) Difference in NPQ between *wt* and *npq4*, which is a measure of  $qE$ . The black bar at the top indicates times when the plant is darkened, and the white bar indicates actinic light illumination.

well as the relaxation of  $qE$  to a low steady-state value. The remaining discrepancies between model and experiment are likely due to dynamics of photosynthesis that are not incorporated into the model, particularly the fact that the activation of ATP synthase and the consumption of ATP involve more complicated kinetics than what is currently incorporated into our model.

At higher light intensities, the model gives better agreement with experiment because the rate of proton flux into the lumen is large enough that the  $\Delta\text{pH}$  that activates  $qE$  remains large even when ATP synthase is fully activated. As shown in Figure 1.9 B, at  $1000 \mu\text{mol photons m}^{-2}\text{s}^{-1}$ ,  $qE$  increases monotonically to a value of 1.7, with the amount of  $qE$  mostly saturating within 300 s. When actinic light is turned off,  $qE$  rapidly relaxes back to nearly zero. The model slightly overestimates the rate of  $qE$  relaxation, leading to somewhat faster turn-off kinetics than are observed in actual leaves. This discrepancy could be due to two factors: either the increase in lumen pH is in fact slower than the model predicts, or the transition between a quenched state back to an unquenched state upon the de-protonation of PsbS occurs with a non-negligible rate. Further comparison between the model and experimental data, including simulations of PAM traces, is given below. Because our model does not incorporate slowly-reversible NPQ processes, the simulated  $qE$  relaxes to zero but the experimental  $qE$  appears to be negative upon relaxation (see above).

The timescale of the appearance and disappearance of  $qE$  in Figure 1.9 can be understood in terms of the time-dependent concentrations of PsbS and zeaxanthin/antheraxanthin, as shown in Figure 1.10. The model indicates that the timescale of the turn-on of  $qE$  is determined by the timescale of violaxanthin de-epoxidation (Figure 1.10B), and the rapid turn-off of  $qE$  is determined by the decrease in protonated PsbS (Figure 1.10C). The concentration of both components is determined by the lumen pH, but while the fraction of protonated PsbS (Figure 1.10A) is determined by the instantaneous pH, the fraction of de-epoxidized xanthophyll is determined by the history of the lumen pH, and appears more gradually as illustrated in Figure 1.10B. It is possible that the reason for the presence of these two components of  $qE$  is that the maximal level of  $qE$  for a given light intensity is set by the level of zeaxanthin, which persists in PSII, but that the plant retains the ability to rapidly modulate  $qE$  between a maximal level and a very low level using only PsbS.

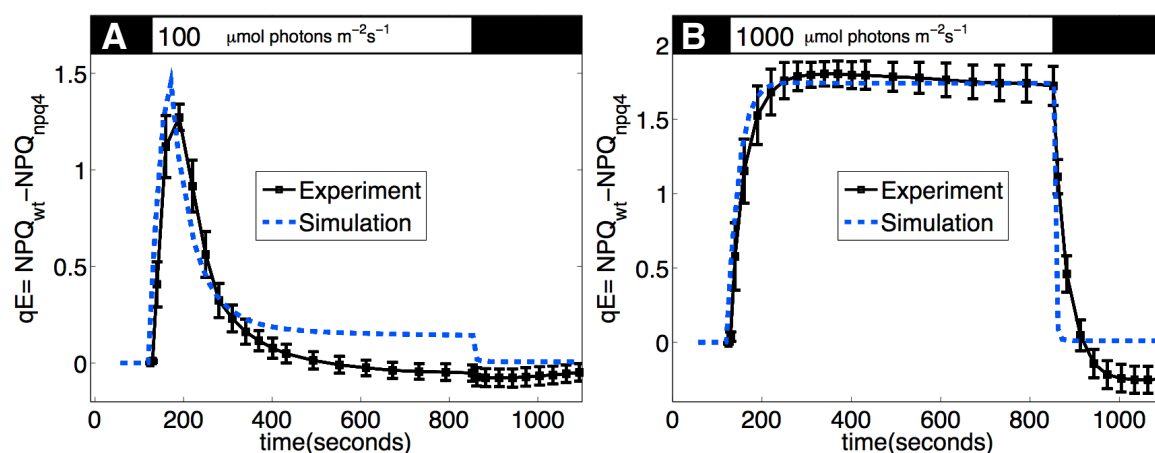


**Figure 1.9:** Measured (squares) and simulated (dashed lines)  $qE$  for input light intensities of A) 100 and B) 1000  $\mu\text{mol photons}/\text{m}^2\text{s}$ . The experimental trace in panel B is the same as in Figure 1.8C. Other than light intensity, all parameters for the simulation are the same.  $qE$  is taken to be the difference in NPQ between the wild type and *npq4* mutant in order to subtract the baseline of slowly-reversible NPQ. Both measured and simulated NPQ values are determined from the PAM traces shown in figure 1.5. The black bar at the top indicates times when the plant is darkened, and the white bar indicates actinic light illumination.

The ability of our model to calculate quantities such as the time-evolution of antheraxanthin and zeaxanthin provides a new opportunity to make testable, quantitative predictions about  $qE$  mechanism. For example, although antheraxanthin, which is a chemical intermediate between violaxanthin and zeaxanthin, is capable of some quenching [49], the relative contribution of antheraxanthin and zeaxanthin to  $qE$ -type quenching *in vivo* is difficult to measure. Our model could easily be modified to include a different rate of quenching by antheraxanthin than by zeaxanthin, which would change the shape of the predicted  $qE$  induction curve. By comparing predicted  $qE$  induction curves with simulations at a range of parameters and light intensities, it should be possible to clarify the role of antheraxanthin in the appearance and disappearance of  $qE$  quenching. As another example, the model could be extended to incorporate a rate of PsbS-induced rearrangement in the PSII antenna that leads to formatting of a quenching site once PsbS is protonated and zeaxanthin and antheraxanthin are made. By simulating  $qE$  induction curves that can be fit to experimental data for different values of this rearrangement rate, it should be possible to restrict the value of the timescale of  $qE$  quenching site formation to a narrower range than is currently known.

### 1.6.1 $qE$ as a feedback loop

Figure 1.11 shows the simulated lumen pH with and without  $qE$  for input light intensity of 100 and 1000  $\mu\text{mol photons}/\text{m}^2\text{s}^{-1}$ . It is notable that the two curves look identical, suggesting that the  $\Delta\text{pH}$ , which triggers  $qE$ , is not itself affected by  $qE$ . This simulated result is consistent with the experimental finding that in the *npq4* mutant,  $\Delta\text{pH}$  and xanthophyll cycle pigment levels are the same as those of wild type [13, 20]. The fact that  $qE$  does not appear to significantly affect the lumen pH indicates that  $qE$  does not affect the *pmf*

for driving ATP synthase under steady state conditions; consequently, qE does not dissipate excitons that could be used for driving linear electron flow that generates *pmf*. This result quantifies and corroborates the interpretation of experimental findings suggesting that, under specific conditions, overexpressing PsbS appears to help plants [17]. If qE is a “conservative” feedback loop, over-expressing the capacity for qE provides more photoprotection without excessively quenching useful excitons.

To examine the range of parameters for which the lumen pH is unaffected by qE, we ran the simulation at a range of values of the rate  $k_Q$ , which modulates the amount of quenching of chlorophyll excitation in the PSII antenna by a quenching site. The lumen pH for values of  $k_Q$  ranging from 1/300 ps to 1/10 ps is shown in Figure 1.12. Physically, this rate is a measure of the probability that a chlorophyll in the PSII antenna will be quenched by a qE site, and, in feedback control terms, can be thought of as the “gain” of the qE quenching feedback loop. Because the lumen pH is a component of the *pmf*, having too high a gain would reduce the  $\Delta\text{pH}$  and would waste energy that can be used for ATP synthesis; on the other hand, too low of a gain would cause the system to be insufficiently protected by quenching too few excess excited chlorophylls. Figure 1.12 suggests that, within the predictions of our current model, quenching rates faster than 1/100 ps would cause the feedback loop to be so aggressive that proton motive force is lost. We anticipate that this type of analysis, in conjunction with more refined models of qE and of energy transfer in PSII, will provide greater perspective on the role of qE in photosynthesis.

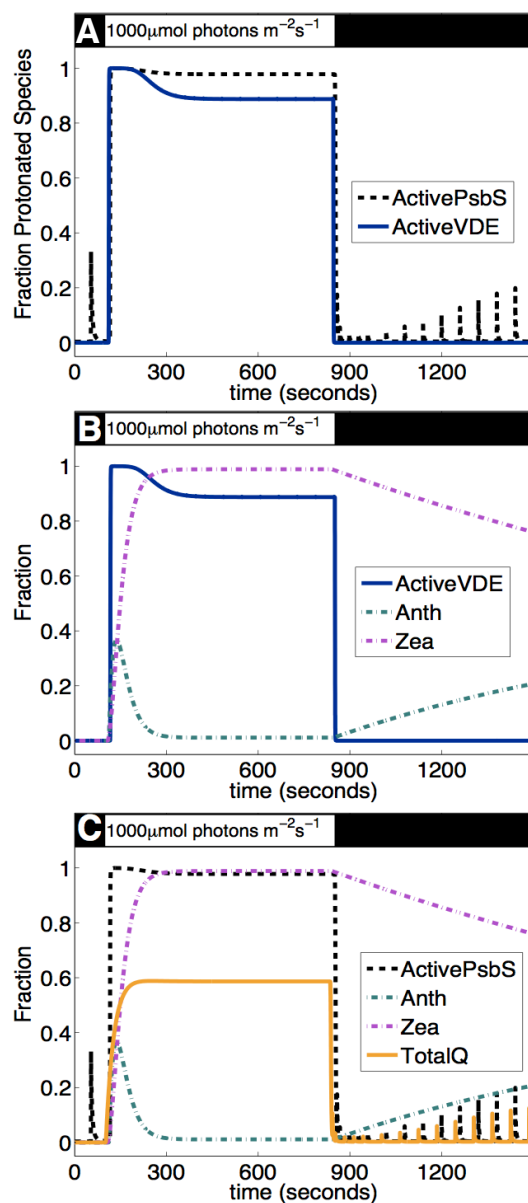


**Figure 1.10:** Evolution of quenching species at  $1000 \mu\text{mol photons/m}^2/\text{second}$ . Simulations done with the same parameters as those used in figure 1.9A. Key parameters are given in Table 1.2. The black bar at the top indicates times when the plant is darkened, and the white bar indicates actinic light illumination. A) Fraction of PsbS (black dashed line) and Violaxanthin Deepoxidase (blue solid line) that are activated by the lumen pH. B) Activity of Violaxanthin Deepoxidase (blue solid line) and fraction of xanthophyll that is in the form of antheraxanthin (green dashed line) and zeaxanthin (red dashed line) in a qE-relevant binding site that is made from violaxanthin by VDE. C) Fraction of total qE quenching sites with protonated PsbS (black), zeaxanthin or antheraxanthin (green/red dashed line) and active qE quenching pathways (orange solid line), assuming equation 3.1. The rate of qE induction is slower than the rate of qE relaxation because, in our model, qE induction is limited by VDE activity, whereas PsbS is de-activated rapidly, turning qE off.

## 1.7 Concluding remarks

We have presented a model of rapidly-reversible feedback-activated NPQ in photosynthetic organisms (qE). Our model accurately simulates the changes in the quantum yield of chlorophyll fluorescence that arise from NPQ pathways at low and high light intensities; accurate simulation of the system governing qE at low and high light intensities is an important step towards quantifying the role of qE in protecting PSII in fluctuating light conditions. Currently there is interest in engineering photosynthetic organisms to maximize photosynthetic efficiency, both to increase crop yields and to produce biofuels. Because of the interconnectedness of photosynthetic processes, a systems approach to modeling the properties of photosynthesis is necessary. We have described a model that treats Photosystem II as a system with feedback and that incorporates a mechanistic model of qE. Our model suggests that qE quenching, which is activated by the pH of the thylakoid lumen, does not affect the lumen pH in plants and therefore does not regulate linear electron flow in steady state conditions.

It would be interesting to use the model to explore the range of parameter values for which qE does not affect the lumen pH, the proton motive force, and linear electron flow in order to assess the robustness of the qE feedback mechanism to variation in parameter values. Because the model we have presented contains a mechanism for qE that enables an assessment of the effect of physiological parameter values (e.g.  $pK_a$ s of protein residues) on the amount of qE, it can serve as a tool for assessing how changes in the components of the qE mechanism would affect photosynthetic yield. In the future, it seems likely that this model, in conjunction with systematic measurements of available *Arabidopsis* mutants at various light intensities, will be valuable for estimating the effect of qE on internal physiological parameters of the thylakoid that are difficult to measure directly *in vivo*. In particular, examining the NPQ at different light intensities in the *npq1* mutant, which lacks VDE, the *lut2* mutant, which lacks lutein [70], and the *npq1lut2* mutant, which lacks both zeaxanthin and lutein, will provide insight into the contribution to qE from VDE-dependent and VDE-independent components. Lastly, analysis of the robustness of the model to parameter variation, as well as an examination of the structure of the feedback loops that control qE, should inform on the regulatory requirements faced by any light-harvesting systems that exist in conditions where light intensity fluctuates.

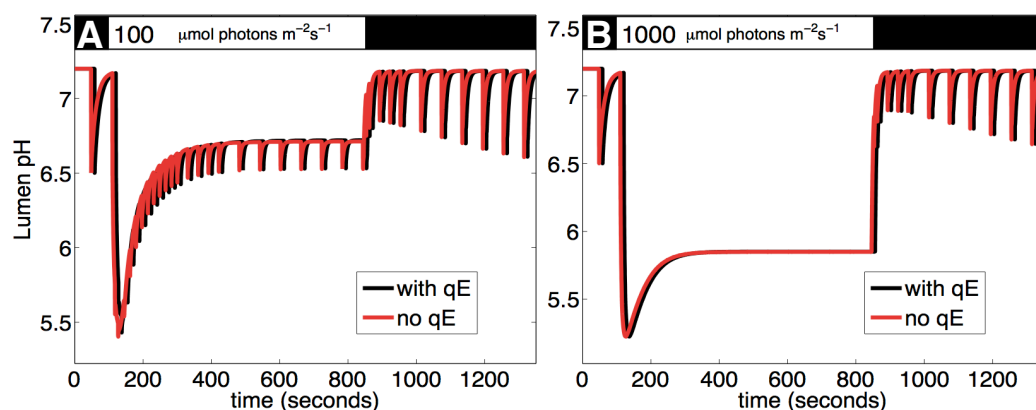


**Figure 1.11:** Effect of qE on pH of thylakoid lumen at A) 100 and B) 1000  $\mu\text{mol photons/m}^2/\text{second}$ . For the values for qE activation given in Table 1.2, the model predicts that qE has minimal effect on the pH of the lumen, suggesting that qE quenching does not lead to a significant reduction in Linear Electron Flow (LEF). This result indicates that qE only quenches excitations that do not contribute to *pmf* and ATP synthesis, suggesting that qE does not waste useful energy. The black bar at the top indicates times when the plant is darkened, and the white bar indicates actinic light illumination.

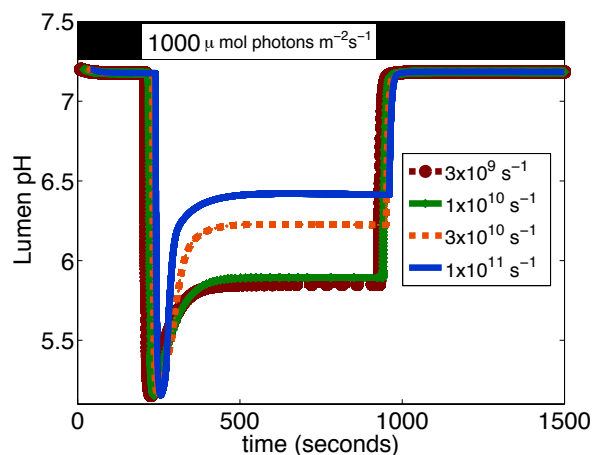


**Figure 1.12:** Effect of varying the rate  $k_Q$  on the lumen pH at 1000  $\mu\text{mol photons/m}^2/\text{second}$ . For quenching rates of  $3 \times 10^9$  and  $1 \times 10^{10}$ , corresponding to timescales for quenching of 300 ps and 100 ps, the lumen pH is essentially unaffected by qE (see also figure 1.11 B). At faster rates of quenching, the feedback quenching of qE is strong enough that it affects the value of the lumen pH, which is the trigger for qE.

## 1.8 Appendix: Model structure

Matlab code containing the equations used in the simulations can be found at the URL

<http://www.cchem.berkeley.edu/grfgrp/jzaks/supp/html/index.html>

Overall, the structure of the model has the following form:

$$\begin{aligned}\dot{\mathbf{X}} &= BG(I(t); p) + \sum_{k=1}^8 A_k^T F_k(A_k \mathbf{X}, u_k; p) \\ u_k &= C_k \mathbf{X}\end{aligned}\tag{1.9}$$

The variables in the model are vertically concatenated in vector  $\mathbf{X}$ . Each  $F_k$  consists of a module that propagates some subset of the variables in vector  $\mathbf{X}$ .  $G(I(t); p)$  is a scalar function relating the input (light intensity) to the evolution of light harvesting variables, and  $B$  is a  $2 \times 1$  matrix relating the inputs to components of vector  $\mathbf{X}$  that represent light harvesting chlorophylls in PSII and PSI, contained in the functions  $F_1$  and  $F_5$ .  $G(I; p)$  does not depend on any components of  $\mathbf{X}$ , which means that the model assumes that the rate of light absorption by antenna chlorophylls is independent of the state of the photosynthetic apparatus. This assumption may need to be relaxed in the future if processes such as state transitions, which remove light harvesting complexes from PSII, are incorporated. The qE component of the model comprises a feedback loop because the input to qE is the lumen pH and qE itself is an input to the light harvesting module. A summary of the modules in the model is given in Table 1.1.

Because many variables are shared between modules, the differential equation at each time step for a given variable is determined by adding the contributions of differential equations from each module that affects that variable. For example, the number of protons in the lumen is affected by three modules: PSII, cytochrome  $b_6f$ , and ATP synthase; the resulting time-evolution of protons in the lumen is the sum of the contributions from these three modules.

Formally, to keep track of the distribution of variables into modules, we introduce the matrix  $A_k$  for each module  $k$ .  $A_k$  is a  $m \times n$  matrix, where  $n$  is the length of  $\mathbf{X}$  and  $m$  is the number of variables that are propagated by the function  $F_k$ . The matrix  $A_k$  has a 1 in each of its  $m$  rows to select the components of  $\mathbf{X}$  that are propagated in module  $F_k$ . To sum the contributions from individual modules, each differential value  $\dot{X}_k = F_k(X_k)$  is multiplied by the transpose of  $A_k$ . In the current implementation of the model, these matrices are generated automatically during the initiation phase (see file `initChloroplastSim` and `getIndices`)

Each module may require inputs of system variables in addition to those that are propagated by that module. For example, qE quenching is activated by lumen pH but does not itself affect the pH, so the pH is an input to the module ( $F_2$ ) for qE rather than a variable that is propagated by that module. Each module accepts an additional vector  $u_k$  that contains inputs for function  $F_n(X_n)$ . To calculate  $u_k$  at each time point in the simulation, the vector of variables  $X$  is multiplied by a matrix  $C_k$  of size  $p \times n$ , where  $p$  is the number of inputs to module  $k$  and  $n$  is, as before, the length of variable  $X$ .

### 1.8.1 Running the simulation

To run a simulation, the model requires 1) a sequence of light intensities and durations of these light intensities, 2) a vector of initial conditions, and 3) a set of values to use for each parameter. The time-step taken by the differential equation solver is determined by the differential equation solver provided in MATLAB (we use *ode15s*, but any stiff solver would in principle work). The solver varies the time step of the simulation to balance efficiency of simulation with accuracy [71].

### 1.8.2 Units used in simulation

The variables for describing light-harvesting, qE quenching and electron transfer through the PSII reaction center and plastoquinone pool are expressed in terms of concentrations of number of molecules per PSII. To calculate the lumen pH and the proton motive force, we converted from number of molecules per PSII to molar concentrations.

### 1.8.3 Chlorophyll fluorescence

Wild type (ecotype Colombia) and *npq4* mutants of *Arabidopsis thaliana* were grown at 50-100  $\mu\text{mol photons m}^{-2}\text{s}^{-1}$ . Plants were dark-adapted for 30 minutes before measurements. The fluorescence yield of attached leaves of 6-week old plants was measured as described previously [66].

### 1.8.4 Simulations

The differential equations were solved using the *ode15s* solver, which is provided with the MATLAB (The Mathworks, Inc) environment for simulating stiff differential equations. Commented code containing the equations used in the model is available online, and the link and instructions are provided below.

# Chapter 2

## Manual for NPQ Systems Model

### Contents

---

<b>2.1 Setup</b> . . . . .	<b>28</b>
2.1.1 Input settings . . . . .	28
2.1.2 Running a simulation . . . . .	40
<b>2.2 Displaying and exporting results</b> . . . . .	<b>42</b>
<b>2.3 Conclusions and future work</b> . . . . .	<b>45</b>

---

To facilitate the exploration of the model for NPQ described in Chapter 1 (which will be referred to here as NPQSM, for NPQ Systems Model), I developed a GUI for the model that interfaces with the MATLAB code. A screenshot for the GUI is shown in figure 2.1. This chapter contains a manual for the GUI, which should enable users to use the model for a wide range of purposes without requiring extensive familiarity with MATLAB.

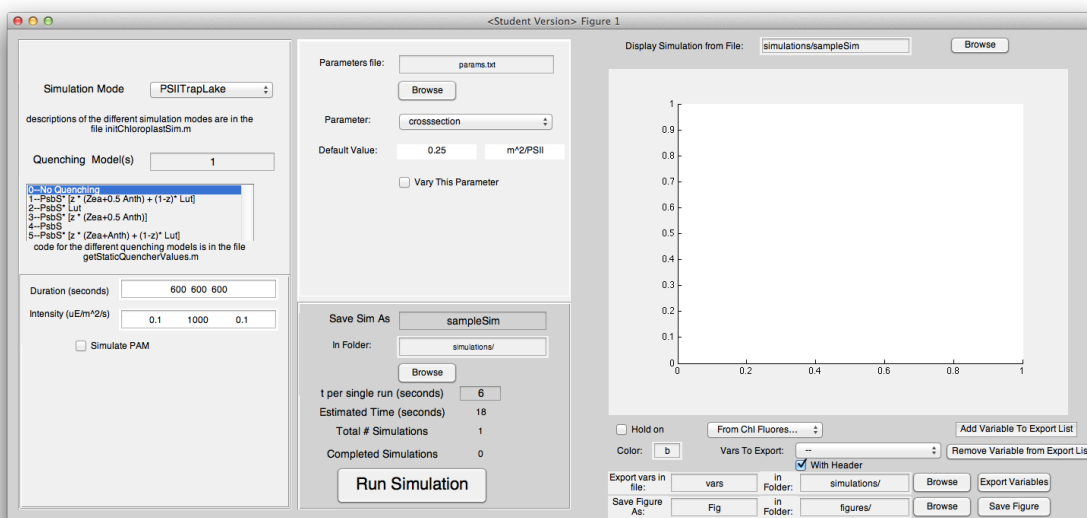


Figure 2.1: Screenshot of full NPQSM GUI.

## 2.1 Setup

### 2.1.1 Input settings

The model enables a number of different types of simulations. Currently, it is possible to control the following settings:

- simulation mode, which describes the set of modules that are included in the simulation. The modules are described in Chapter 1.
- quenching model, which describes the mathematical expression used for  $qE$
- intensity and duration of incident light
- values of model parameters

Figure 2.2 shows the inputs to the model that can be controlled by the user. In the top left panel, The “Simulation Mode” input specifies which modules are incorporated into the simulation and the “Quenching Model(s)” input specifies what model is used for  $qE$ . In the bottom left panel, the “Duration(seconds)” input specifies the duration that each segment of the model will be run in, and the “Intensity” input specifies the intensity of the actinic light for each segment. On the top right, the “Parameters file” input specifies a text file that contains the parameters needed to run the model. the “Parameter” menu bar shows all the parameters contained in the text file, and checking the box “Vary This Parameter” allow the user to input a range of values for the parameter shown in the menu. On the bottom right, the input “Save Sim As” allows the user to specify the name and location of the file to which the simulation will be saved. At the bottom, the large button “Run Simulation” starts the running simulation described by the inputs here. The inputs are described below in more detail.

The screenshot shows the NPQSM GUI with the following settings:

- Simulation Mode:** PSIITrapLake
- Parameters file:** params.txt
- Parameter:** crosssection
- Default Value:** 0.25 m<sup>2</sup>/PSII
- Vary This Parameter
- Quenching Model(s):** 1
- Quenching Models List:**
  - 0--No Quenching
  - 1--PsbS\* [z \* (Zea+0.5 Anth) + (1-z)\* Lut]
  - 2--PsbS\* Lut
  - 3--PsbS\* [z \* (Zea+0.5 Anth)]
  - 4--PsbS
- Duration (seconds):** 600 600 600
- Intensity (uE/m<sup>2</sup>/s):** 0.1 1000 0.1
- Simulate PAM
- Save Sim As:** sampleSim
- In Folder:** simulations/
- t per single run (seconds):** 6
- Estimated Time (seconds):** 18
- Total # Simulations:** 1
- Completed Simulations:** 0
- Run Simulation** button

**Figure 2.2:** The two left columns of the NPQSM GUI contain inputs to the model.

## Simulation mode

Figure 2.3 shows the different simulation modes available in the model. The “simulations mode” setting determines which modules are simulated, so each simulation mode corresponds to a different set of differential equations. The simulation mode used in the figures of Chapter 1 is “PSIITrapLake,” which has this name because the model of energy transfer in PSII that is currently implemented, and was used to generate figures in Chapter 1, is a trap-limited lake model. The other simulation modes contain different combinations of modules:

- **PSI** contains only the Photosystem I (PSI) module, which is implemented in the code `evolvePSI.m`, and is useful for troubleshooting the components of the model associated with PSI.
- **LEF** contains the modules for Photosystem II, qE, plastoquinone pool, cytochrome *b<sub>6</sub>f*, ATP synthase, and the stroma, which describe some components of linear electron flow.

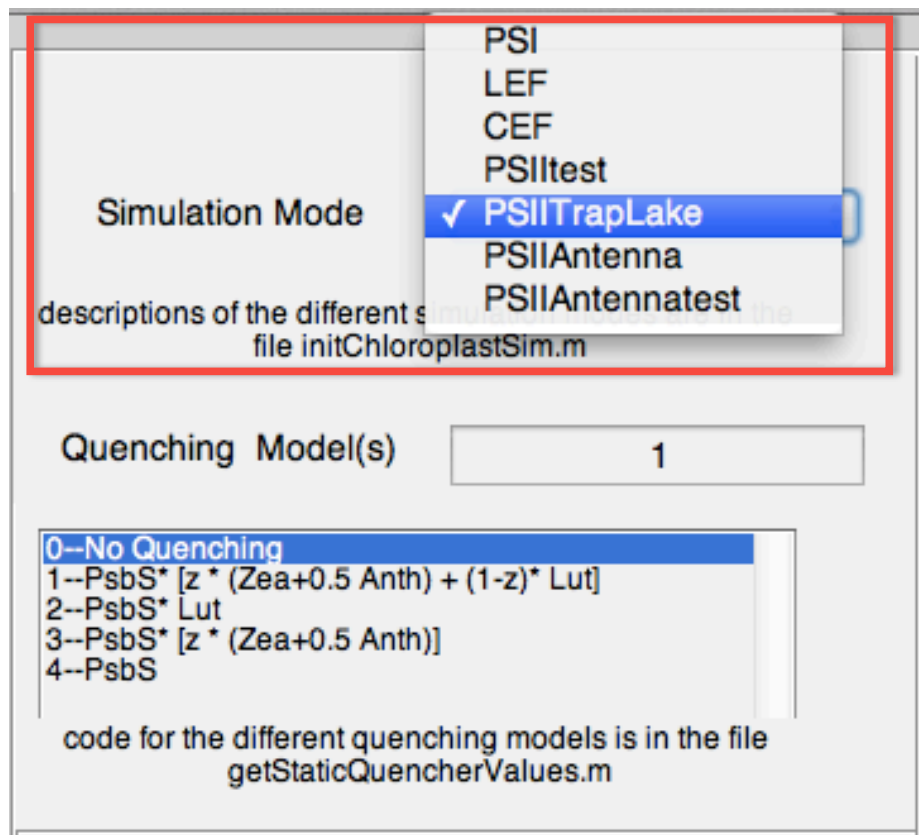


**Figure 2.3:** Screenshot of NPQ Systems Model GUI. The different simulation modes are outlined with the red rectangle.

- CEF contains all the modules in LEF, plus a module for implementing cyclic electron flow from PSI to cytochrome  $b_6f$ . This model does not currently produce reliable simulations, but would be an important extension of the model for incorporating cyclic electron flow and its role in the regulation of photosynthesis [64].
- PSIItest contains the modules PSII, qE, PQ, cytochrome  $b_6f$ , and the flow of ions across the thylakoid membrane (contained in the module `evolveLume.m`, with equations taken from reference [40]) and is useful for testing the model without PSI. In this simulation mode, all plastocyanin will be eventually reduced.
- PSIITrapLake is the default model described in Chapter 1. It contains the modules for PSII, qE, the plastoquinone pool, cytochrome  $b_6f$ , proton pumping through ATP synthase, activation of ATP synthase, and the flux of ions across the thylakoid membrane, and electron transfer through PSI.
- PSIIAntenna incorporates a model of energy transfer described in reference [72], which represents energy transfer in PSII as a hopping through many pigment-protein complexes. Currently, qE is not usefully incorporated into this model because doing so

would require an assignment of a specific quenching site to qE. This task is an important future extension. It also seems likely that the model of [72] should be eventually replaced with a model of energy transfer in PSII being currently developed by Doran Bennett in the group of Prof. Graham Fleming. This mode has split up processes in PSII into two modules, called `evolvePSIIAntenna`, which describes energy transfer, and `evolvePSIIRC`, which describes electron transfer kinetics.

- `PSIIAntennaTest` contains the modules `PSIIAntenna`, which incorporates energy transfer as hopping model between different sites, `PSIIRC`, `qE`, and flux of ions in the lumen, as a way of testing the PSII antenna energy transfer model without the added complication of cytochrome  $b_6f$  and the plastoquinone pool. It is only useful to simulate this module for a short time (few seconds) because once the initial oxidized plastoquinone is depleted, the model stops turning over.

These simulation modes are defined in the file `initChloroplastSim.m`, and new simulation modes can easily be added in that file.

## Quenching model

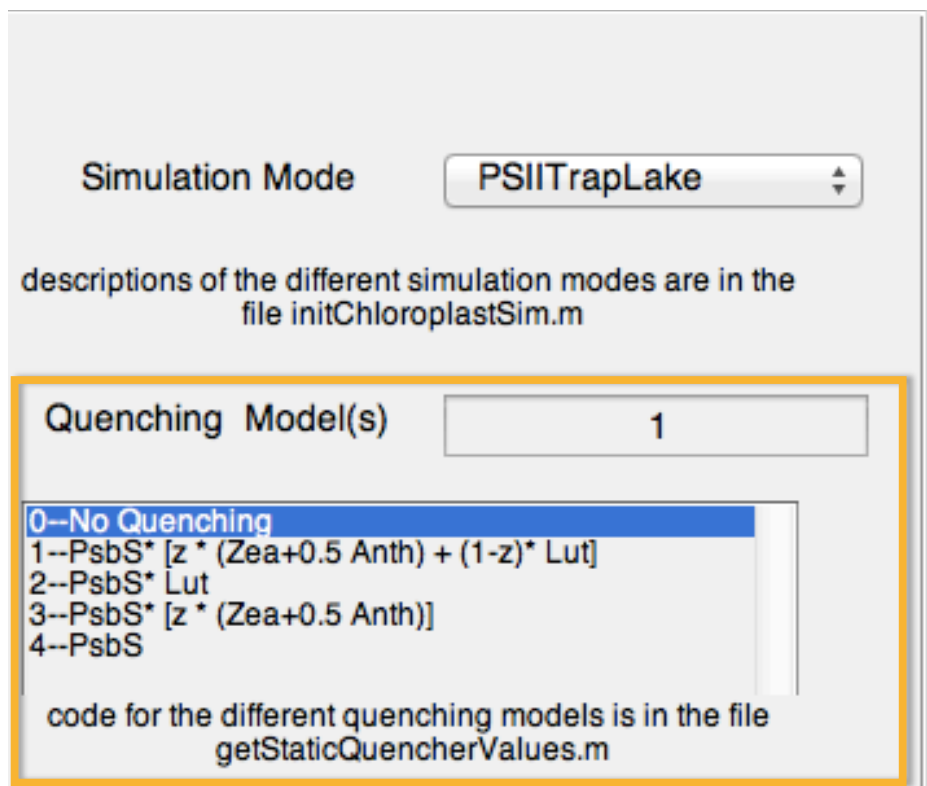


**Figure 2.4:** Screenshot of upper left portion of the NPQSM GUI. The different quenching modes are outlined with the yellow rectangle. The quenching model will only be incorporated into the simulation if the module for PSII is present in the simulation mode. These simulation modes are `PSIItest`, `PSIITrapLake`, `LEF`, and `CEF`.

The simulation mode “PSII Trap Lake” currently incorporates qE quenching as an additional dissipation pathway in Photosystem II. It is known that full expression of qE depends on both PsbS and the presence of zeaxanthin or antheraxanthin, but a complete understanding of the relative contribution of these two components, and the extent of their interdependence, remains elusive [73]. NPQSM can be used to examine the effect of various quenching models on predictions of PAM fluorescence and other model variables. The location in the GUI to select one or more quenching models for simulation is shown in Figure 2.4. Currently, the model has implemented four different quenching models:

- **Model 0: No Quenching.**

- **Model 1 : Zeaxanthin and Lutein, with PsbS**

Both zeaxanthin-dependent and zeaxanthin-independent quenching. This model is discussed in Chapter 3. The variable  $z$  is the fraction of total qE quenching that is xanthophyll-dependent, and is a parameter that can be controlled by the user. By default, it is set to be 0.5. This quenching model uses the expression

$$[Q] = [PsbS] * (z([Zea] + 0.5[Anth]) + (1 - z)[Lut])$$

Where  $[Lut]$  is the concentration of lutein in a PsbS-dependent quenching site. Studies of the lutein-deficient mutant *lut2* suggest that lutein is important for full expression of qE, [70], as discussed in Chapter 3. Mathematically, the value of  $[Lut]$  is currently set to be 1 because lutein is assumed to always be present in a qE-relevant site. This model also assumes that total quenching is proportional to the xanthophyll de-epoxidation state, which is equivalent to assuming that antheraxanthin is half as effective a quencher as zeaxanthin. This assumption may not be entirely accurate, as reports have suggested that antheraxanthin and zeaxanthin are equally good quenchers[74].

- **Model 2: Only Lutein and PsbS** Only xanthophyll-independent quenching. This model could be used to describe qE in the *npq1* mutant, which lacks Violaxanthin Deepoxidase. This model uses the expression

$$[Q] = [PsbS] * [Lut]$$

- **Model 3: Only Zeaxanthin and PSbS** Only zeaxanthin-dependent quenching. This is the model used in chapter 1, except that in this expression antheraxanthin is assumed to be half as effective at quenching as zeaxanthin. The expression is

$$[Q] = [PsbS] * (z([Zea] + 0.5[Anth]))$$

- **Model 4** Only PsbS determines quenching. Mathematically, this is currently similar to model 2 with zeaxanthin-independent quenching. In the future, it could be useful to have a model for PsbS-induced aggregation and/or dissociation, which has been suggested to play a role in qE by some studies [27, 75].

In the GUI, the existing models are described in the list box shown in Figure 2.4. The simulation can be run with one or more quenching models. To run a single quenching model, input the number of that model into the text box labeled Quenching Model(s), and to run multiple quenching models, input the number of all quenching models, separated by either spaces or commas, into that same text box. Currently, the numbers of the quenching models used in the simulation must be entered in the text box; selecting quenching models from the list box that contains descriptions of the different quenching models does not do anything, though this is something that should be improved in the future to make the GUI more user-friendly. The code that runs these different GUI expressions is in the file `getStaticQuencherValues.m`, and new quenching models could be added to this file and then run from the GUI.

### Parameter values

The NPQSM contains a large number of parameters. Some of these parameters have known values, but the values of many others are unknown or may not have well-defined values (i.e. may fluctuate from organism to organism or from leaf to leaf). One of the advantages of the large-scale systems model developed here is the ability to calculate the effect of changing one or more parameters on the behavior of the system. The GUI displays all the parameters of the model in a drop-down menu, as shown in Figure 2.5. The parameters file, which is named `params.txt` in the figure, contains all the parameters necessary for the model. The formatting for the parameters file is described in the file `getparamsfromfilename.m`. The drop-down menu under “parameter” will display all the parameter values in the parameters file, and when a parameter is selected, its value and units will be displayed in the text box labeled “Default Value”.

The GUI currently has the capability to vary the value of a single parameter at a time, as shown in Figure 2.6. It is currently possible to vary multiple parameters in code, and in the future, it will be useful to incorporate the ability to vary multiple parameters directly in the GUI.

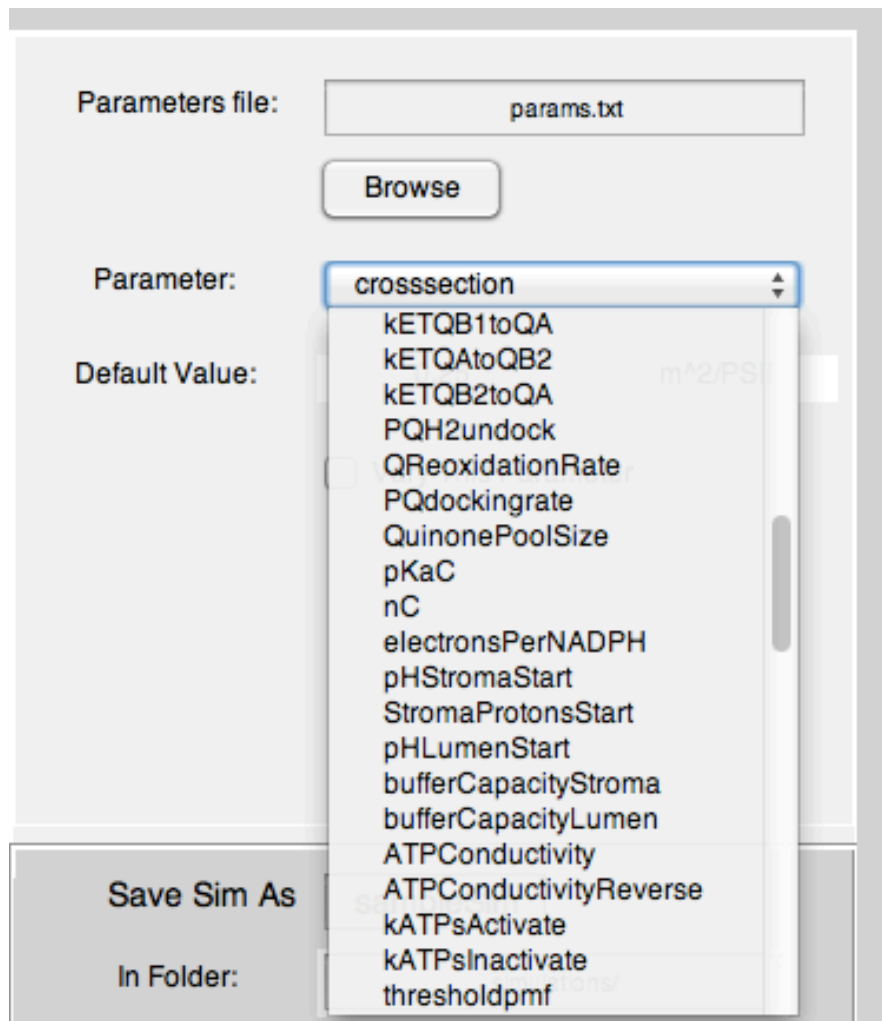
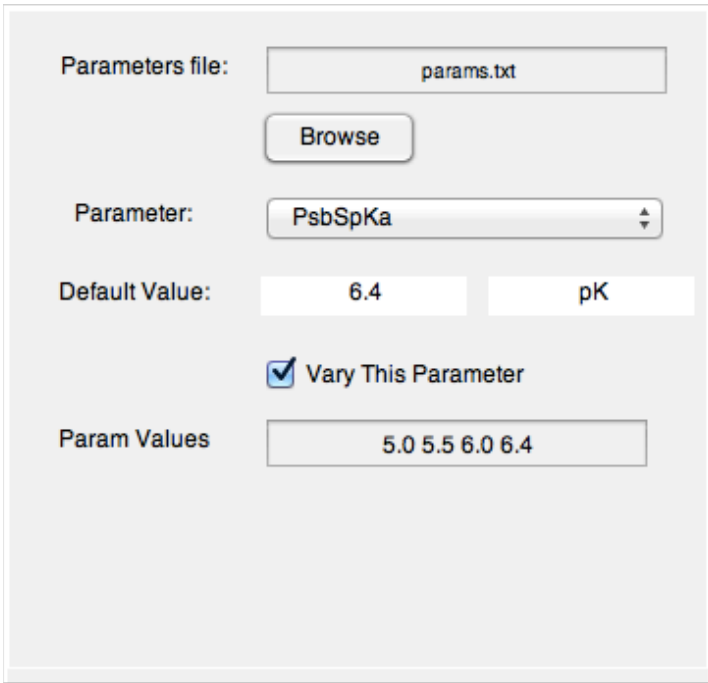


Figure 2.5: Popup menu of various parameter values.



The screenshot shows a dialog box for parameter setup. It contains the following elements:

- Parameters file:** A text box containing "params.txt" and a "Browse" button below it.
- Parameter:** A dropdown menu with "PsbSpKa" selected.
- Default Value:** Two text boxes, the first containing "6.4" and the second containing "pK".
- Vary This Parameter:** A checked checkbox.
- Param Values:** A text box containing "5.0 5.5 6.0 6.4".

**Figure 2.6:** When the box “Vary This Parameter” is checked, the input box “Param Values” becomes visible and the user can enter the desired parameter values for the selected parameter. Currently, it is only possible to vary one parameter at a time.

The figure shows two side-by-side GUI panels for setting simulation parameters. The left panel has two text boxes: 'Duration (seconds)' containing '600 ; 600 ; 600' and 'Intensity (uE/m^2/s)' containing '0.1 ; 100 1000 ; 0.1'. Below these is a checkbox labeled 'Simulate PAM' which is unchecked. The right panel has a 'Duration (seconds)' box with '125 0.5 4.5 0.5' and an 'Intensity (uE/m^2/s)' box with '0.001;7000;100 1000;7000;100 100'. It has a checked 'Simulate PAM' checkbox. Below are 'Actinic Light Intensity' (100 1000), 'Saturating Pulse Intensity' (7000), 'Flash Length (seconds)' (0.5), and 'Flash Positions' (a file path). A 'Browse' button is below the path, and a 'Load PAM Intensity and Duration' button is at the bottom.

**Figure 2.7:** There are two ways to input light intensity to the model: directly enter intensity and duration into text boxes (left) or specify intensities for PAM fluorescence experiment and load pulse times and actinic light on/off times from a saved file (right). The semicolon separates intensities of different segments, so the two intensities within the same segment indicate that two separate simulations at two different light intensities should be performed.

### Light intensity and duration inputs

NPQSM is able to simulate the evolution of PSII parameters at light intensities between 0 and  $2000 \mu \text{ mol photons/m}^2/\text{s}$ , which corresponds to the range of realistic terrestrial sunlight intensity. The model can also simulate very intense pulses of light (intensities of  $10,000 \mu \text{ mol photons/m}^2/\text{s}$  or more, which correspond to flashes that close all reaction centers), although running the simulation with such a high input for more than a few seconds may drive the model to give unphysiological results.

Each function call of the differential equation solver takes a single light intensity as an input.<sup>1</sup> To run the model, it is necessary to specify light intensity input in segments of constant light intensity, and the duration of each segment. This is done in the boxes labeled “Duration” and “Intensity”, shown at the top of both left and right panels in Figure 2.7.

To create multiple simulations in which some of the light intensity segments are the same but some vary, separate each segment of light intensity by a semicolon. The simplest example of this situation is the simulation sequence dark-light-dark, where the light intensity for the “dark” portion would always be the same but the light intensity for the “light” portion would vary. To run two simulations, where the light intensity for the first is 0.1- 1000- 0.1 and for the second is 0.1 -500 -0.1, the light intensity input would be 0.1; 500 100; 0.1.

PAM fluorescence [31] is a common experiment done to study NPQ in plants, so the NPQSM GUI has a separate input mode for setting up simulations to reproduce PAM fluorescence experiments. PAM fluorescence uses a combination of actinic light and saturating flashes to probe the fluorescence yield of the plant, and can probe the amount of NPQ that the

<sup>1</sup>As an improvement to the model to enable the simulation of continuously varying light intensities, it may be possible to write a function  $I(t)$  that describes light intensity as a function of time and input that function to the ode solver.

plant is able to do. To access this mode, check the “Simulate PAM” checkbox, as shown in the right panel of Figure 2.7. The PAM fluorescence experiment requires the following inputs: 1) the actinic light intensity (which ranges from 0 to 2000  $\mu\text{Mol photons/m}^2/\text{second}$ ), 2) the intensity of saturating flashes (which is typically 5,000-10,000  $\mu\text{Mol photons/m}^2/\text{second}$ ), 3) the duration of the saturating flashes, which is usually between 0.1 second - 1 second, 4) the times in the simulation when the actinic light is turned on and off, and 5) the times in the simulation when the saturating flashes are turned on and turned off. Inputs 1-3 can be input to the GUI using the text boxes that appear when the box “Simulate PAM” is checked. Inputs 4 and 5, which related to the times of actinic light turning on and the times of the saturating flashes, can be input as a text file. An example of the contents of such a text file, named `pulsetimes.txt`, is shown below.

### Contents of `pulsetimes.txt`:

```
125
actOn
130
140
160
190
220
250
280
310
340
370
401
432
493
552
612
672
732
792
852
actOff
862
882
913
943
973
1004
1034
1064
1094
1124
1185
1244.5
1305
```

### Estimating run time of model

Figure 2.8 illustrates the built in functionality of the GUI to estimate the time the program will take to run all the combinations of quenching modes, light intensities, and parameter values. The GUI calculates the number of total simulation runs for the set of quenching models and parameter value that have been provided. Figure 2.8 shows a set of inputs with two different quenching models (yellow), four parameter values for the PsbS pKa (green), and three light intensity segments for one simulation (blue), giving a total of 8 simulations (red). To estimate the time it will take the computer to run, the user should input the quantity “t per single run,” since this quantity is dependent on the speed of the processor on which the model is being run. In Matlab, it can be estimated by using the commands `tic` and `toc` around a single call of the ode solver in the script `runChloroplastSim.m`. The program multiplies the total number of runs by this input time value to get a time estimated total time. The actual time per run will vary for different parameters because of variations in how quickly the differential equation solver converges to a solution, which depends on the parameters that determine the slope of the variables being simulated.

Simulation Mode: **PSIITrapLake**

descriptions of the different simulation modes are in the file `initChloroplastSim.m`

Quenching Model(s): **2 Quenching Models**

0--No Quenching  
 1--PsbS\* [z \* (Zea+0.5 Anth) + (1-z)\* Lut]  
 2--PsbS\* Lut  
 3--PsbS\* [z \* (Zea+0.5 Anth)]  
 4--PsbS

code for the different quenching models is in the file `getStaticQuencherValues.m`

Duration (seconds):

Intensity (uE/m^2/s):

Simulate PAM

3 segments per simulation

Parameters file:

Parameter:

Default Value:

Vary This Parameter

Param Values:   
 4 parameter values

Save Sim As:

In Folder:

t per single run (seconds)	<input type="text" value="6"/>	8x3x6 = 144
Estimated Time (seconds)	<input type="text" value="144"/>	seconds total
Total # Simulations	<input type="text" value="8"/>	2x4 = 8 total simulations
Completed Simulations	<input type="text" value="0"/>	

**Figure 2.8:** Overview of the factors that affect the length of time that running a simulation will take: the number of quenching models (yellow box), number of light intensity segments (blue box), number of parameters values being varied (green box) are all multiplied by each other to give the estimated time for the simulation to run. The “Total # Simulations” (red box) shows the product of the number of quenching models and the number of parameter values.

## 2.1.2 Running a simulation

To run a simulation, press the “Run” button at the bottom center of the GUI, as shown in Figure 2.9. If the simulation is able to run successfully, the MATLAB command window will display an output similar to the one shown in the left panel of Figure 2.10, which is a set of outputs from the ODE solver. If there are problems with the simulation, they typically show up as errors in red text in the command window.

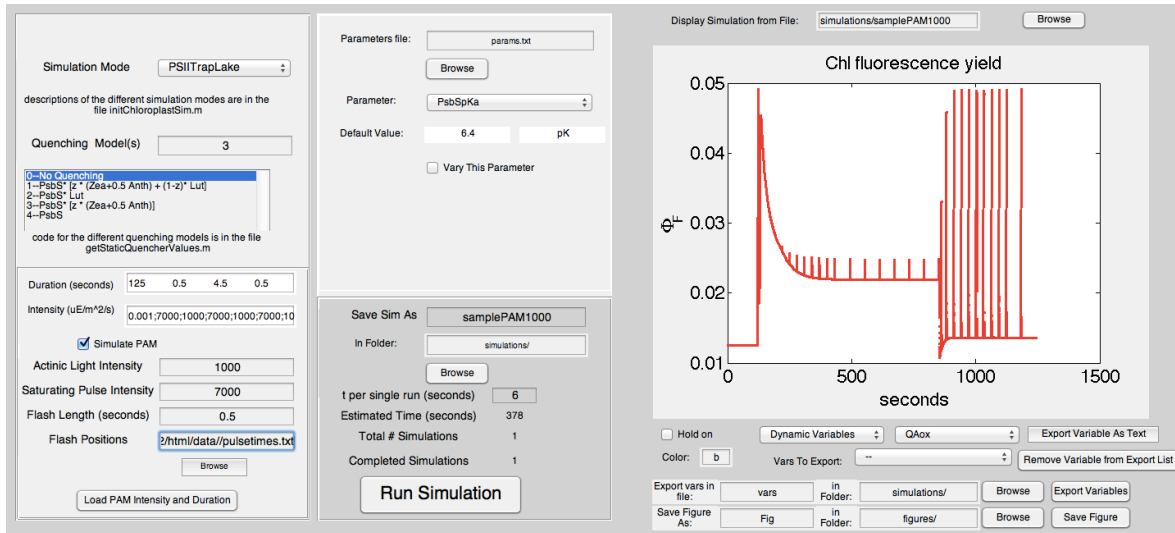


**Figure 2.9:** Sample Simulation of a PAM fluorescence measurement

After a simulation is successfully completed, it will automatically be saved so that it can be loaded and displayed in the future. The format for saving a simulation is a `.mat` file, so that the simulation can easily be loaded as a MATLAB variable. The right panel of Figure 2.10 shows the section of the GUI where the name of the `.mat` file can be specified. The yellow square circles the text box for entering the name of the file with which the simulation will be saved, and the folder in which the simulation will be saved. The “Browse” button can be used to select the folder in which to save the simulation file.

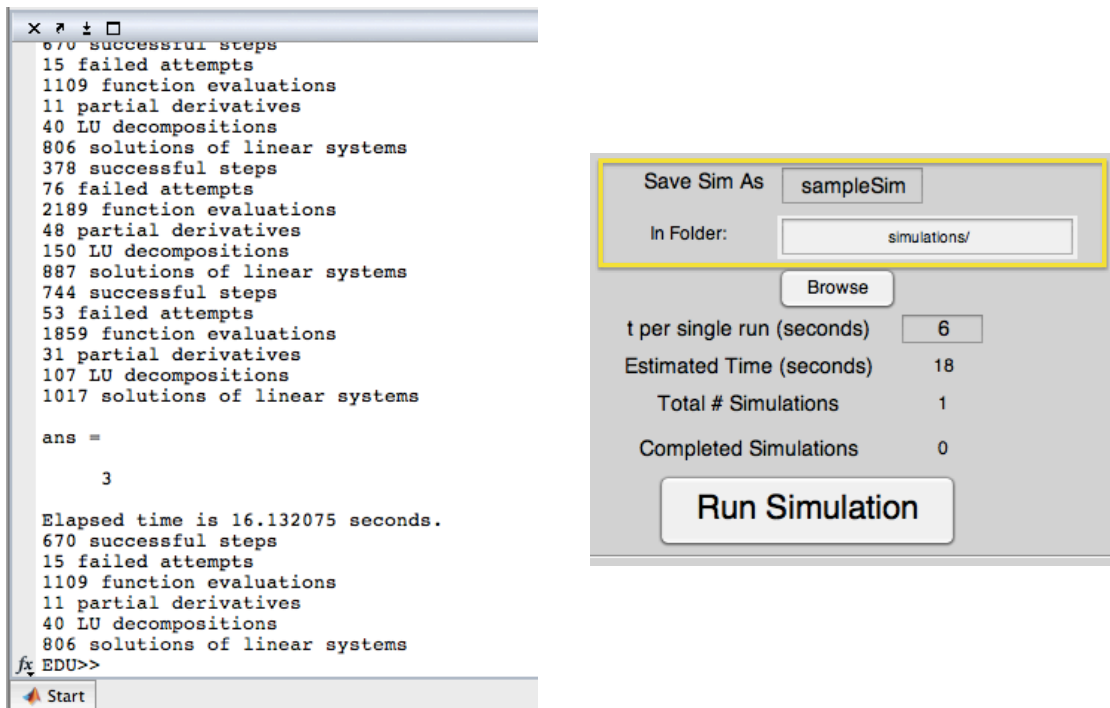


**Figure 2.10:** Left: Output from the model ode solver to the MATLAB command line when the model is running successful after the button “Run Simulation” has been pressed. Right: controls for specifying the name and location of a saved simulation.

## 2.2 Displaying and exporting results

After the simulation has been saved as a `.mat` file, it can be loaded and the simulation results can be displayed in the future and exported as a text file for further manipulation. Figure 2.11 shows the values of oxidized  $Q_A$  for a simulation of PAM fluorescence displayed in the GUI. The simulation to display can be loaded with the “Browse” button on top (green box). The type variable to display can be selected from the pop up menu (red box). The types of variables that could be displayed are grouped into three categories: quantities that are calculated from chlorophyll fluorescence (labeled “From Chl Fluorescence”), dynamic variables that have a differential equation associated with them, and static variables that are calculated from the dynamic variables. Lists of static and dynamic variables are shown in Figure 2.12. The spikes in the figure arise from the saturating flashes of the PAM fluorescence simulation.

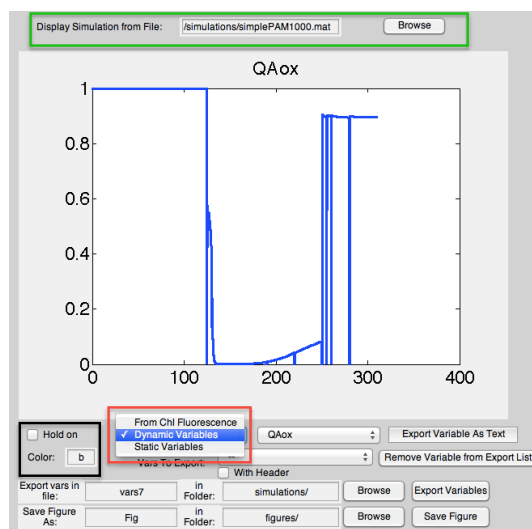


**Figure 2.11:** The right panel of NPQSM GUI displays simulated quantities from saved simulations. To retain the plot of the previous variable, check the “hold on” checkbox (black rectangle) and to change the color of the plot, enter a different color string into the color text field. The current plot color is blue (`'b'`), and the possible colors are red (`'r'`), blue (`'b'`), green (`'g'`), cyan (`'c'`), magenta (`'m'`), yellow (`'y'`), and black (`'k'`).

Figure 2.11 highlights the controls for specifying the types of variables to be displayed in the plot, along with controls about retaining the previous plot and how to specify the color of the new plot. Figure 2.12 shows the lists of the “Static Variables” and “Dynamic Variables” that can be displayed with the GUI. The Dynamic Variables are ones that have been simulated directly in the model, i.e. ones for which an explicit differential equation has been written. Some examples of Dynamic Variables are number of excited chlorophylls,  $Q_A$  redox state, and concentration of protons in the lumen. The Static Variables are quantities that are calculated from the Dynamic Variables, such as lumen pH, the electric field across the thylakoid membrane, the proton motive force, and the fraction of activated cytochrome  $b_6f$ . The Static Variables are calculated from the Dynamic Variables of the simulations in the functions `getStaticQuencherValues.m` and `getStaticThylakoidValues.m`.

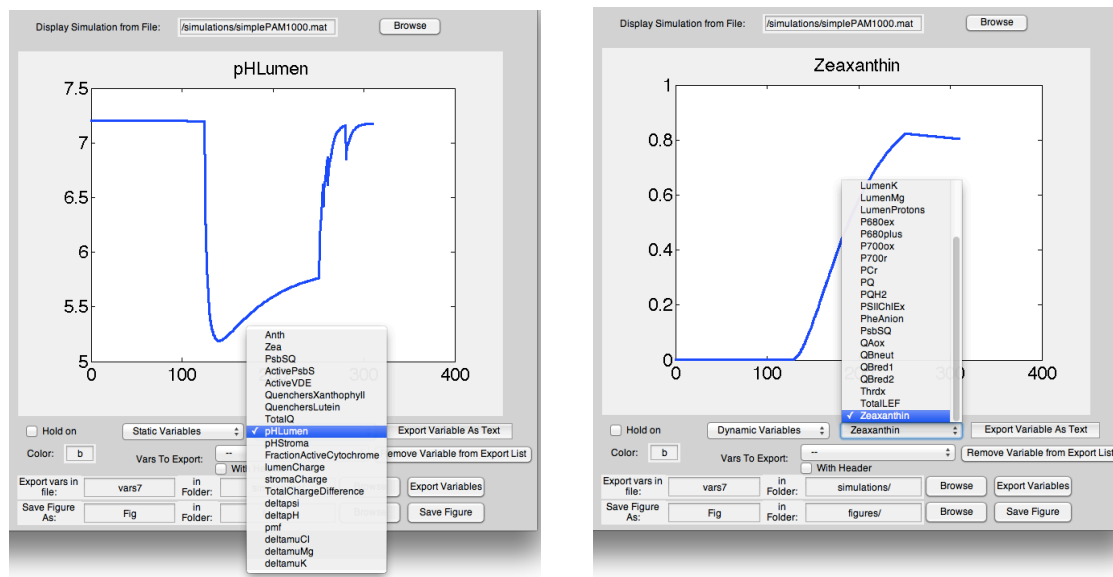


**Figure 2.12:** Lists of Static variables (left) and Dynamic variables (right) of the model.

The GUI can export figures as `.eps` files and lists of variable values as text files. Figure 2.13 shows the controls on the GUI for saving the plots of variables as `.eps` files. Specify the name of the saved figure file in the first text field (currently set to “Fig”) and the target location of the file in the second text field (currently set to “figures/”, and can be navigated with the “Browse” button). To export the figure, push the “Save Figure” button. This will open the figure in a new window and save it to the specified location.

Figure 2.14 highlights the controls for exporting variable values as text files. Select the variable to be exported in the variable menu (black box), the press “Add Variable to Export List” (red box). Note that the quantities associated with chlorophyll fluorescence can not currently be exported. The variable to be exported will be added to the “Vars to Export” list (green box). To remove a variable from the list of variables to be exported, select that variable and press “Remove Variable from Export List (Right Panel, magenta box). To export the variables into a text file (blue box), enter the name of the text file in the first text field (currently set to “vars”), the location in the second text field (currently set to “simulations/”) and press Export Variables. To include the names of the variables in the text file, check the “With Header” box.

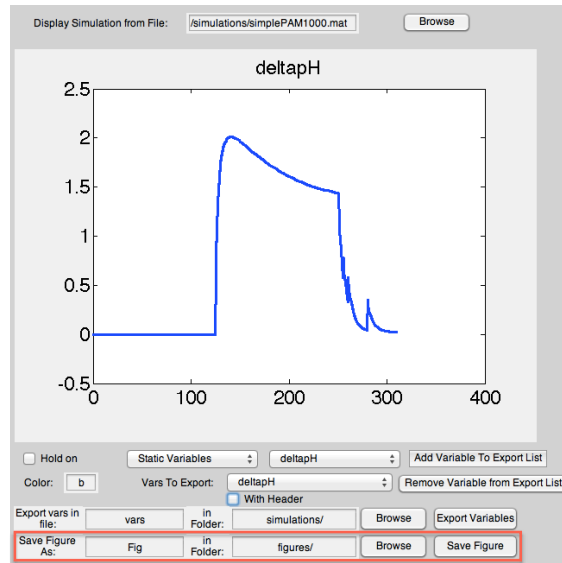


**Figure 2.13:** The controls for exporting the figure as an image file are outlined with the red box.

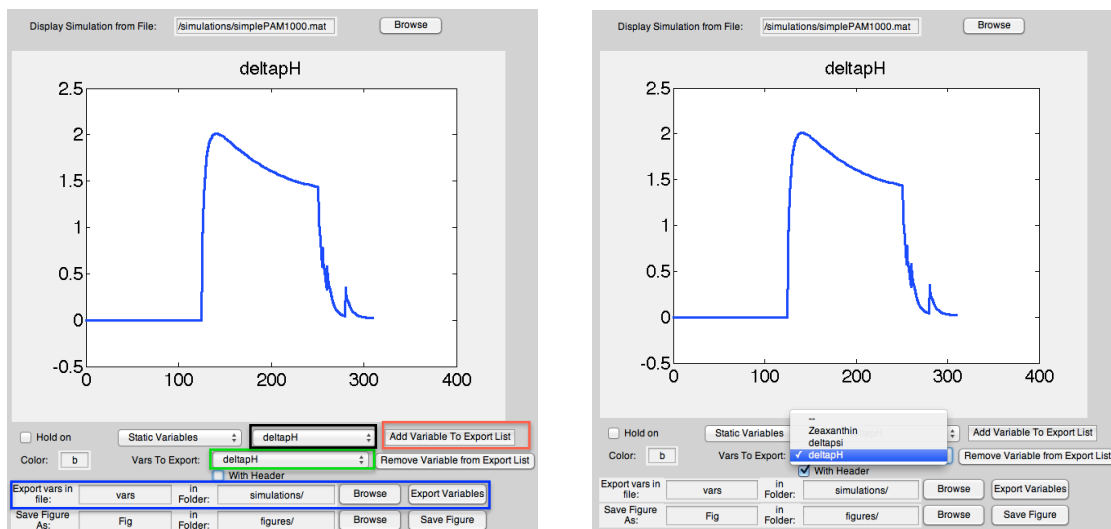


**Figure 2.14:** The GUI can export the numerical values of simulated quantities (Static or Dynamic Variables), along with the time axis, into a text file.

## 2.3 Conclusions and future work

The GUI for the NPQ Systems model should prove to be useful to computational researchers, physical chemists, and plant biologists who are interested in learning how to use and extend the model. Using the model for more complicated computational projects will require integration with the MATLAB code, but the GUI should still act as a useful introduction to the capabilities and limitations of the model.

There are numerous changes to the GUI that would increase its functionality and ease of use. To improve the GUI's functionality, it would be useful to:

- Enable the variation of multiple parameters in a given simulation
- Make it possible to specify light intensity as a continuous function of time, rather than as discrete segments

To improve the GUI's ease of use, it would be useful to:

- Separate the simulations inputs (first two columns) and the display (last column) into separate tabs.
- Allow the user to enter an expression for the quenching model from the GUI.
- Make it easier for the user to obtain information directly from the gui about the different simulations modes. One way in which this could be done is by incorporating popup boxes with more detailed information.
- Add a legend onto the figure for situations when more than one curve is displayed in the figure axes.
- Replace the “Vars To Export” popup menu with a list box to make the process of adding and removing variables from the Vars to Export List more intuitive.
- Combine the file name and folder in the inputs for exporting variables and figures.
- Enable exporting quantities derived from chlorophyll fluorescence, namely chlorophyll fluorescence and simulated NPQ.

# Chapter 3

## Modeling the role of carotenoids and PsbS in qE

### Contents

---

<b>3.1</b>	<b>Lutein in qE model</b>	<b>48</b>
<b>3.2</b>	<b>PsbS dosage effect</b>	<b>50</b>
<b>3.3</b>	<b>Light-intensity dependence of model</b>	<b>58</b>
<b>3.4</b>	<b>Conclusion</b>	<b>61</b>

---

The model presented in Chapter 1 was developed in order to study the role and mechanism of rapidly-reversible nonphotochemical quenching. In this chapter, we discuss extensions of the model to explain the role of lutein, zeaxanthin, and PsbS levels in rapidly-reversible nonphotochemical quenching.

Over the past two decades, numerous mutants of *Arabidopsis thaliana* with altered lutein [70], xanthophyll cycle [76, 22] and PsbS [20, 13] compositions have provided a great deal of information about the components of qE. It appears that the PsbS protein is required for all rapidly reversible NPQ in physiological conditions, and that increasing the expression level of PsbS increases the capacity for qE [13, 51]. The carotenoids lutein and zeaxanthin are needed for full expression of qE, but qE appears to some extent in the presence of only one carotenoid [16] and it has been shown that lutein can substitute for zeaxanthin in some cases [77].

It is not clear whether there is only one PsbS-dependent quenching site or whether there are several sites that interact with PsbS and are activated by low lumen pH. It has been proposed that there are two qE quenching sites—one in the antenna and one in the minor complexes [78]. It is also not clear whether zeaxanthin and lutein bind to the same site, or to different sites. If zeaxanthin and lutein affect different sites, it is not clear if the quenching at each of the two sites is independent of the other, or if the two sites interact with each other in some way.

Figure 3.1 (left) plots the difference in NPQ between the *npq1* and *lut2* mutants and the

*npq4* mutant, which lacks PsbS. The data are taken from reference [16].<sup>i</sup> The appearance of NPQ has different kinetics in the *npq1* (no VDE) and *lut2* (no lutein) mutants, which could suggest that lutein and zeaxanthin bind to two independent quenching sites. The sum of the qE from these two mutants is close to, but slightly lower than the qE from wild type. Figure 3.1 (right) shows the NPQ levels of wild-type and the L17 mutant, which has elevated levels of PsbS [13].

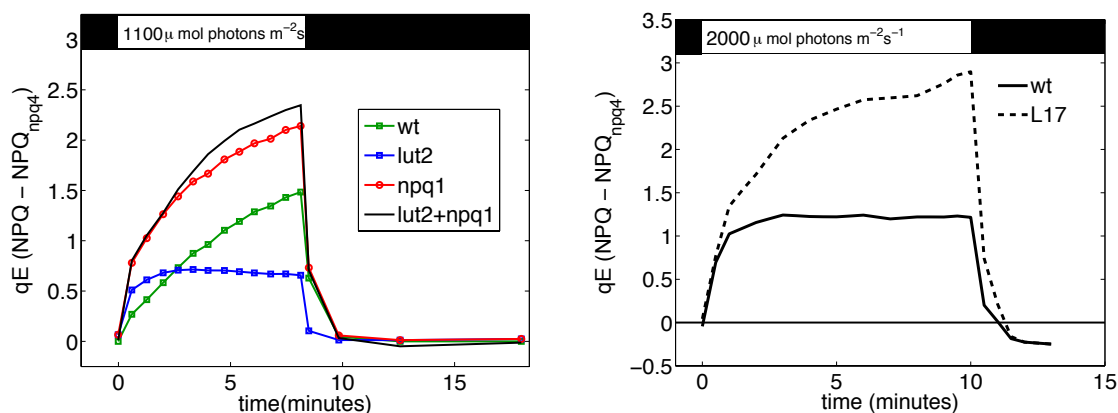


**Figure 3.1:** Left: Rapidly reversible component of qE in *npq1* and *lut2* mutants of *A. thaliana* leaves, from Figure 2A of reference [16]. The value of the actinic light is 1100  $\mu$  mol photons/m<sup>2</sup>/s. The qE levels in the *npq1* mutant (blue squares), *lut2* mutant (green squares) and the sum of these *npq1* and *lut2* mutants (red circles) are lower than the rapidly-reversible NPQ in wild type (black line). Right: qE in wild type (solid line) and L17 mutant (dashed line), which has elevated levels of PsbS, taken from reference [13]. The difference in wild type levels between the right and left plots are probably related to differences in growth conditions, as the plants were grown in two different laboratories and were illuminated with different intensities of actinic light.

The appearance and disappearance of qE occur more rapidly in *npq1* than in *lut2*. One possible interpretation of these distinct kinetics is that there is a lutein-dependent site that is rapidly activated, and a zeaxanthin-dependent site in which quenching appears as zeaxanthin is made from violaxanthin. The decay of qE is also faster in the *npq1* mutant than in the *lut2* mutant, further supporting the idea that zeaxanthin-dependent qE and lutein-dependent qE occur at different sites.

If zeaxanthin-dependent and lutein-dependent qE were independent of each other, the sum of the qE of the two components should match the qE from wild type. The slightly lower qE levels in the sum of the two components shown in Figure 3.1 compared to wild type suggests that there could be an interaction between zeaxanthin-dependent qE and lutein-dependent qE that contributes more to quenching than the individual components. On the other hand, this discrepancy is small, so this data could also be plausibly interpreted to suggest that zeaxanthin-dependent quenching and lutein-dependent quenching act independently.

Examining the kinetics of qE mutants at lower light intensity also contains information about the relative contributions of lutein and zeaxanthin to qE. Figure 3.2 shows qE of wild type, *npq1*, and *lut2* at a light intensity of 100  $\mu$  mol photons/m<sup>2</sup>/s. In contrast to the situation

<sup>i</sup>In the following paragraphs we will refer to the difference in NPQ between a mutant and *npq4* as qE, because of the assumption that all qE is PsbS-dependent.

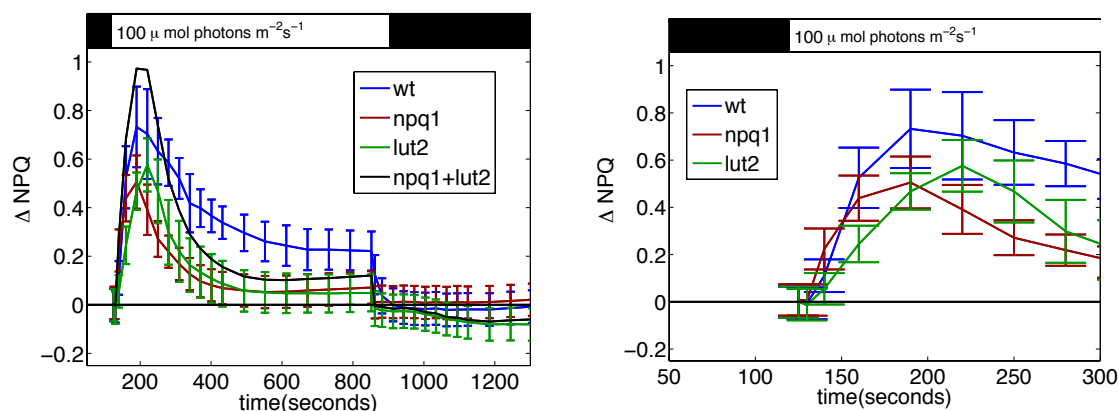


**Figure 3.2:** qE of wild type (blue), *npq1* (red) and *lut2* (green) in  $100 \mu \text{ mol photons m}^{-2}\text{s}^{-1}$ , which is below levels that saturate photosynthesis. The plants were grown in the lab of K. Niyogi and the PAM measurements were collected by me. The black line shows the sum of qE in *npq1* and *lut2*; the sum rises to a higher level than wild type, then falls to a lower level, suggesting that the qE in these two mutants cannot be simply added to give the qE of wild type. Following exposure to light, the qE of all mutants rises initially, the plateaus. The qE in wild type has a higher level than the mutants throughout. The qE in the *npq1* mutant and the *lut2* mutant is similar, although the qE in *npq1* appears to rise slightly sooner than the qE in *lut2* (right panel, zoom).

at high light intensity shown in Figure 3.1, the qE profile of *npq1* and *lut2* at low light intensity are similar to one another in that a transient qE is formed and then dissipated as the plant adapts to light. The slightly faster rise of qE in the *npq1* mutant compared to *lut2* could also support the hypothesis that lutein and zeaxanthin facilitate qE at different sites.

### 3.1 Lutein in qE model

The simple model of qE that was used in chapter 1 assumes that all qE quenching is dependent on both zeaxanthin and PsbS, and is modeled mathematically as

$$[Q] = F_{PsbS} \cdot [PsbS]^* \cdot ([Z] + [A]) \quad (3.1)$$

While it seems that all rapidly-reversible quenching in physiological conditions is dependent on the presence of the PsbS protein[20], the role of zeaxanthin and antheraxanthin is less clear. Some rapidly-reversible quenching does occur in the *npq1* mutant, which lacks zeaxanthin [16]. This quenching is likely due to lutein for two reasons: 1) the *lut2* mutant, which lacks lutein but has the same amount of chlorophyll as wild type, has reduced levels of qE [70] and 2) the *npq1lut2* mutant, which lacks zeaxanthin and lutein, has no rapidly-reversible quenching, and has the same total NPQ as the *npq4* mutant [79].

A diagram for modeling the PSII antenna that incorporates the contribution of lutein is shown in Figure 3.3. In this model, PsbS is required for qE, but some PsbS-dependent qE is caused by lutein and some is caused by zeaxanthin. Mathematically, this model can be expressed as

$$[Q] = F_{PsbS} \cdot [PsbS]^* \cdot (z([Z] + [A]) + (1 - z)[L]) \quad (3.2)$$

where  $z$  is a fraction specifying the amount of quenching due to zeaxanthin or antheraxanthin. This model assumes that lutein-dependent quenching can occur instantaneously following activation of PsbS.

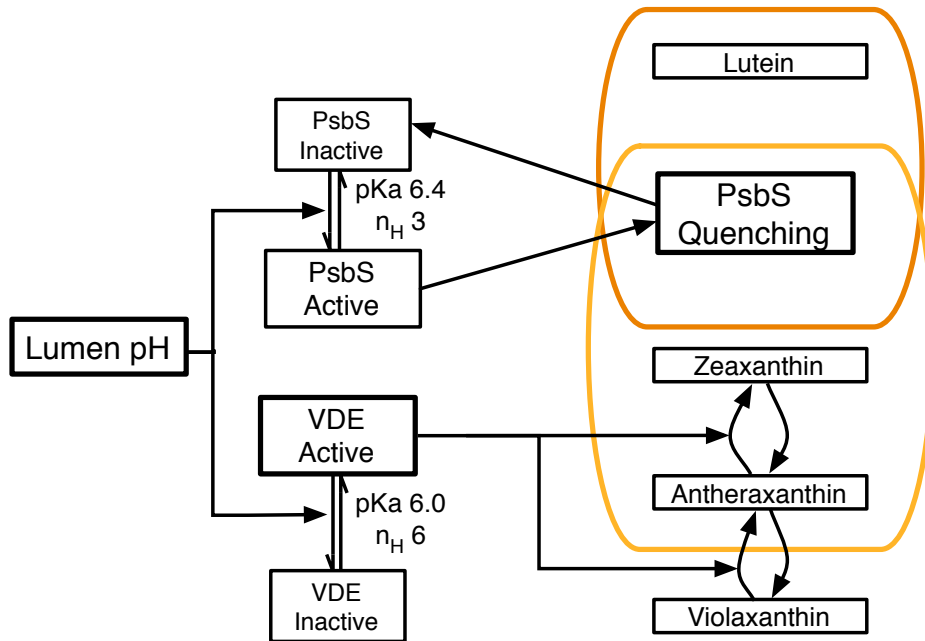


**Figure 3.3:** Extended model of qE with zeaxanthin and lutein. In this schematic, the only element shared by lutein-dependent quenching and zeaxanthin-dependent quenching is active PsbS.

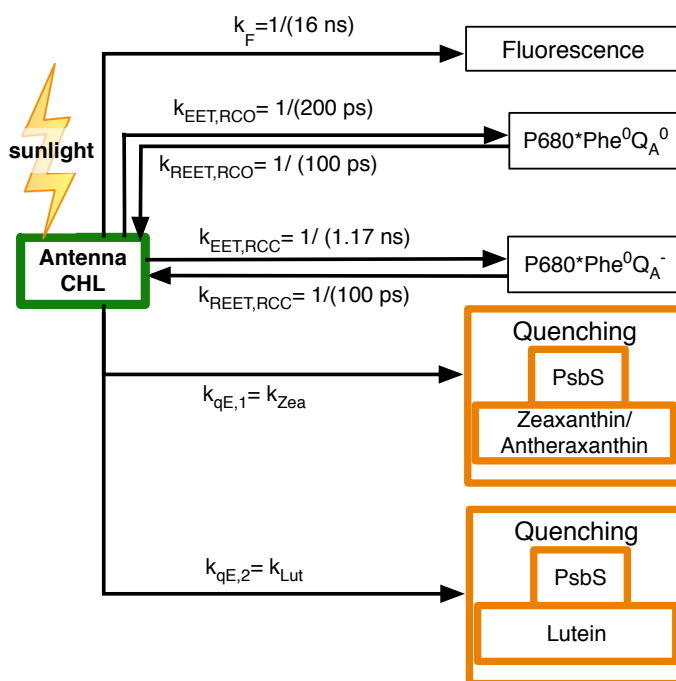


Figure 3.4: Diagram of model of PSII in which there are multiple qE quenching sites.

## 3.2 PsbS dosage effect

The PsbS protein has been shown to be required for all rapidly-reversible nonphotochemical quenching in physiological conditions [20], and overexpression of PsbS leads to elevated levels of qE in plants [13]. Increasing PsbS concentration to levels above the levels found in wild-type increases qE up to a saturating level, as shown in Figure 3.5, where the experimental data are taken from Figure 4 of reference [51]. The role of PsbS in facilitating qE is still unclear, and the available experimental data regarding the effect of PsbS expression levels on qE should inform on the interaction of qE sites with carotenoids and PsbS. Much of the work examining effects of PsbS over expression has been done with mutant line L17, which possesses elevated levels of PsbS and exhibits approximately twice as much qE as wild type [13].

Recent experimental results (Zhirong Li, personal communication) have surprisingly shown that increasing PsbS levels in the *npq1* and *lut2* mutants, which mostly lack zeaxanthin and lutein, respectively, does not result in elevated levels of qE, as shown in Table 3.1. These results suggest that in the presence of only one of either zeaxanthin or lutein, the capacity for PsbS-dependent quenching is not limited by PsbS, whereas in wild-type, PsbS levels do limit qE. We note that other groups have reported conflicting results, as shown in Table 3.1 [80, 81], so there is not currently a consensus regarding the experimental results on the effect of elevated PsbS levels on qE.

Here we present several schemes in an attempt to explain the experimental results obtained by Zhirong Li in the laboratory of Prof. Krishna Niyogi. To make a quantitative

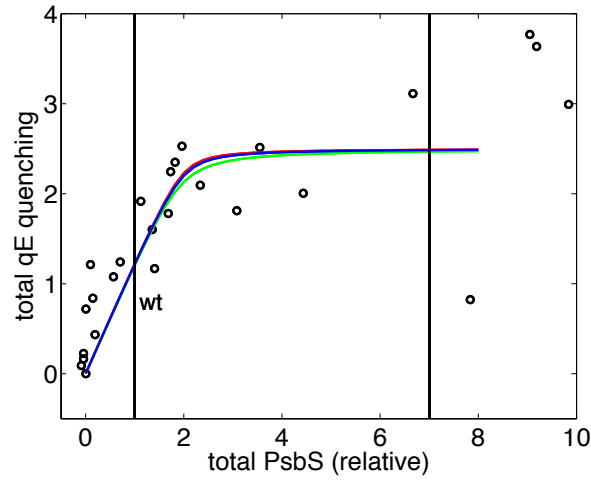


**Figure 3.5:** Measured effect of PsbS dosage on qE (black circles, from reference [51]) compared with prediction of schemes A (red line), B (blue line), and C (green line).

**Table 3.1:** Effect of PsbS levels on qE in zeaxanthin and carotenoid mutants after 12 minutes of illumination by saturating actinic light.

mutant	Max qE wt PsbS Levels	Max qE L17 PsbS levels	reference
wild-type	2.5	4.5	[13] and Z. Li, personal communication
<i>lut2</i>	2.3	2.3	Z. Li, personal communication
<i>npq1</i>	1.2	1.2	Z. Li, personal communication
<i>npq1lut2</i>	1.0	1.0	Z. Li, personal communication
<i>npq1</i>	0.5	0.8	[80]
wild-type/DTT	0.5	1.0	[81]

comparison of these different schemes, it will be important in the future to fit numerical predictions of qE models to experimental data. The experimental data available from mutants can be summarized in the following constraints:

1. the steady-state qE level in the *npq1* mutant is 0.2, where qE is calculated from Table 3.1 by subtracting the NPQ value of the *npq1lut2* mutant from the NPQ value of the mutant. Steady state qE levels in wild-type are 1.5, giving a constraint

$$qE_{npq1} = \frac{0.2}{1.5} qE_{wt} = 0.13 qE_{wt} \quad (3.3)$$

2. the steady-state qE level in the *lut2* mutant is 1.3, giving, analogously to constraint 1,

$$qE_{lut2} = \frac{1.3}{1.5} qE_{wt} = 0.87 qE_{wt} \quad (3.4)$$

3. the qE level in the L17 mutant shown in Table 3.1 is 3.5 yielding the constraint

$$qE_{L17} = \frac{3.5}{1.5} qE_{wt} = 2.3 qE_{wt} \quad (3.5)$$

4. qE levels in the *npq1L17* mutant are the same as in the *npq1* mutant, giving

$$qE_{npq1L17} = qE_{npq1} \quad (3.6)$$

5. qE levels in the *lut2L17* mutant are the same as in the *lut2* mutant, giving

$$qE_{lut2L17} = qE_{lut2} \quad (3.7)$$

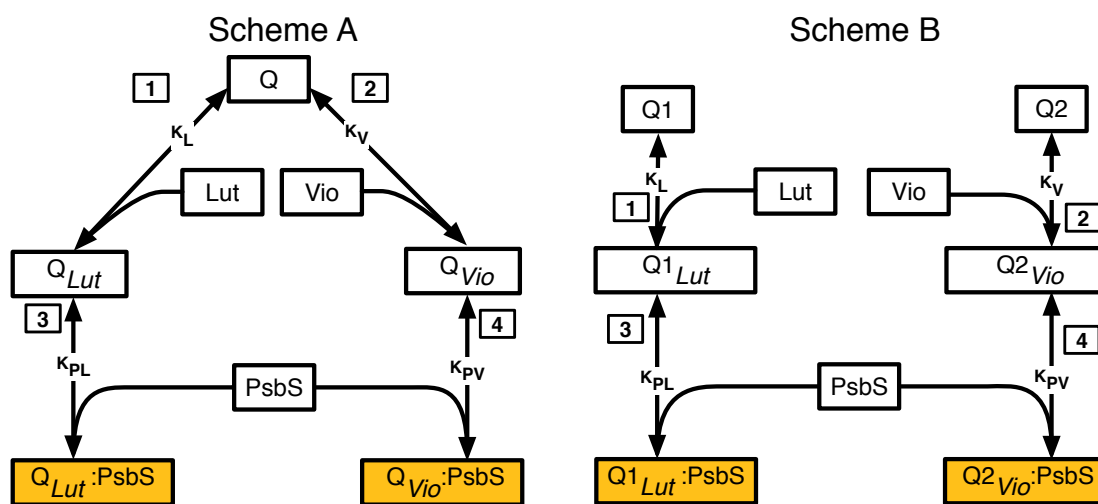


**Figure 3.6:** Two possible models to explain the effect of *PsbS* dosage. In scheme A, there is one quenching site can bind either violaxanthin or lutein. Both schemes assume that the *PsbS* protein is “smart,” meaning that it only interacts with a quenching site that has already bound a qE-capable carotenoid and does not interact with qE sites that do not have a carotenoid bound to them. The sites indicated in orange are capable of doing qE when *PsbS* is protonated. In scheme B, there are two quenching sites,  $Q1$  and  $Q2$ .  $Q1$  binds only lutein and  $Q2$  binds only violaxanthin, and both require *PsbS* in order to be capable of performing qE.

Figure 3.6 shows two possible models that could explain the effect of increasing total *PsbS* abundance on qE. The scheme in Figure 3.6A assumes that there is one qE site that can bind either lutein or violaxanthin, with equilibrium constants  $K_L$  and  $K_V$ . In the case when violaxanthin is bound, it must be converted to zeaxanthin by violaxanthin deepoxidase in order for quenching occurs at the site, so the quenching site with violaxanthin should be considered as “qE-capable” sites. The timescale of converting violaxanthin to zeaxanthin is not included in these schemes, since the schemes predict total capacity for qE as a function of *PsbS* rather than the timescale of the appearance of full qE capacity. The equilibrium constants  $K_L$  and  $K_V$  are measures of the probability that the carotenoids will bind to the site. This site then interacts with *PsbS* with equilibrium constants  $K_{PL}$  (if lutein is bound) and  $K_{PV}$  (if violaxanthin is bound). Because the quantity of interest in these schemes is an equilibrium concentration of quenchers, these schemes apply equally to the situation where *PsbS* must be protonated before binding to a qE site, and to the situation in which *PsbS* binds in the dark, before lumen acidification.

Scheme B of Figure 3.6 assumes two qE sites, one of which binds violaxanthin and the other binds lutein. The difference between schemes A and B is that in scheme A, all qE sites could in principle bind either carotenoid, whereas in scheme B, each carotenoid has a specific binding site. In both models, no assumptions are made about the types of interactions between the qE site and PsbS, nor about where the site(s) are located in the PSII antenna. The nature of the interaction between qE sites, carotenoids, and PsbS would affect the values of the equilibrium constants  $K_L$ ,  $K_V$ ,  $K_{PV}$  and  $K_{PL}$ , but for the purposes of understanding the effect of changing PsbS dosage we treat the equilibrium constants as fit parameters and assume that they do not change as PsbS dosage and carotenoid composition vary; this assumption is necessary at this point to make the problem tractable.

To determine if the schemes of Figure 3.6 can predict the observed dependence of qE on PsbS dosage levels in wild type and mutants, it is necessary to solve for the overall concentrations of qE-capable sites (shown in orange in the figure). Although it is possible to find analytical solutions for these schemes, doing so would involve solving many quadratic formulas and would yield solutions that are too complicated to provide useful insight. Given the speed of modern computer technology and the availability of tools such as MATLAB, it is easier to solve for equilibrium concentrations of quenching sites by simulating differential equations with ratios of rates given by the equilibrium constants between states. It is also possible to solve directly for equilibrium concentrations of each scheme using a nonlinear solving technique implemented in the MATLAB function `fsolve`, which is computationally faster, but could converge to a non-physical solution that has negative values of concentrations because there are multiple mathematical solutions for each equilibrium concentration.

In both schemes A and B,  $K_L$  and  $K_V$  are assumed to be equilibrium constants of carotenoids binding into the qE sites. The absolute magnitude of  $K_L$  and  $K_V$  are measures of the probability that the carotenoids will bind to the qE site rather than remaining unbound or binding to some other site in the thylakoid membrane, and the relative magnitude of  $K_L$  and  $K_V$  is a measure of the relative probability of the qE site binding lutein rather than violaxanthin. Since the model presented here does not attempt to derive the values of the quantities  $K_L$  and  $K_V$ , these would be treated as fit parameters for the purposes of this analysis.

For scheme A, the equilibrium between the qE site and lutein and violaxanthin is given by

$$\begin{aligned}\frac{Q_{Lut}}{Q \times L} &= K_L \\ \frac{Q_{Vio}}{Q \times V} &= K_V\end{aligned}\tag{3.8}$$

The equilibria between carotenoid-bound qE sites (shown in orange) and qE-capable sites, which also have bound PsbS and are denoted  $Q_{Lut} : PsbS$  and  $Q_{Vio} : PsbS$ , are given by

$$\begin{aligned}\frac{Q_{Lut} : PsbS}{Q_{Lut} \times PsbS} &= K_{PL} \\ \frac{Q_{Vio} : PsbS}{Q_{Vio} \times PsbS} &= K_{PV}\end{aligned}\tag{3.9}$$

The total number quenching sites, total PsbS, total violaxanthin, and total lutein are con-

served, giving the following conservation laws:

$$\begin{aligned}
Q + Q_{Lut} + Q_{Vio} + Q_{Lut} : PsbS + Q_{Vio} : PsbS &= Q_{tot} \\
Q_{Lut} + Lut + Q_{Lut} : PsbS &= Lut_{tot} \\
Q_{Vio} + Vio + Q_{Vio} : PsbS &= Vio_{tot} \\
PsbS + Q_{Lut} : PsbS + Q_{Vio} : PsbS &= PsbS_{tot}
\end{aligned} \tag{3.10}$$

For scheme B, there are two quenching sites instead of one, so there are two equations arising from the conservation of quenching sites: the following equilibrium and conservation laws apply:

$$\begin{aligned}
Q1 + Q1_{Lut} + Q1_{Lut} : PsbS &= Q1_{tot} \\
Q2 + Q2_{Vio} + Q2_{Vio} : PsbS &= Q2_{tot}
\end{aligned} \tag{3.11}$$

The other equations of scheme B are similar to those of scheme A:

$$\begin{aligned}
\frac{Q1_{Lut}}{Q1 \times L} &= K_L \\
\frac{Q2_{Vio}}{Q2 \times V} &= K_V \\
\frac{Q_{Lut} : PsbS}{Q_{Lut} \times PsbS} &= K_{PL} \\
\frac{Q_{Vio} : PsbS}{Q_{Vio} \times PsbS} &= K_{PV} \\
Q1_{Lut} + Lut + Q1_{Lut} : PsbS &= Lut_{tot} \\
Q2_{Vio} + Vio + Q2_{Vio} : PsbS &= Vio_{tot} \\
PsbS + Q1_{Lut} : PsbS + Q2_{Vio} : PsbS &= PsbS_{tot}
\end{aligned} \tag{3.12}$$

Figure 3.7 shows the equilibrium concentrations of total quenchers from schemes A and B plotted as a function of total PsbS dosage  $P_{tot}$ , with  $K_L = K_V = 3$  and  $K_{PL} = K_{PV} = 100$ , which were chosen because they appeared to give somewhat good agreement with experimental data as shown in Figure 3.5. The vertical lines are drawn at two different levels of PsbS that could represent PsbS dosage in wild-type and in the L17 mutant. Because the sum of possible quenching sites is normalized to 1 (i.e.  $Q_{tot} = 1$  in scheme A and  $Q1_{tot} + Q2_{tot} = 1$  in scheme B), the value of the x-axis, representing the ratio of total PsbS protein compared to D1 protein, is, when applied to schemes A and B, a measure of the abundance of PsbS protein relative to the total number of quenching sites. The number of PsbS proteins per PSII reaction centers (D1 proteins) has been measured to be 2 [82, 51], but since the number of quenching sites per PSII is unknown, the PsbS levels in schemes A and B to levels corresponding to wild-type and L17 can be adjusted to give good agreement with experiments.

Because violaxanthin and lutein can substitute for one another in scheme A, removing lutein had very little effect on the total concentration of qE sites in scheme A. In scheme B, lutein-dependent and violaxanthin-dependent qE sites are distinct, so removing lutein caused

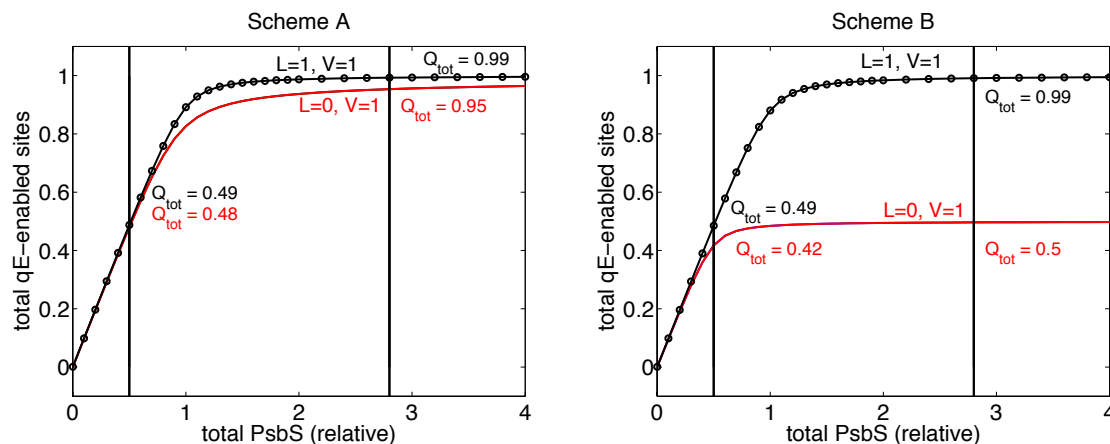


**Figure 3.7:** Sum of equilibrium concentrations of lutein-dependent and violaxanthin/zeaxanthin-dependent quenching sites in schemes A and B of figure 3.6 for  $L_{tot} = 1$  and  $V_{tot} = 1$  (blue circles) and  $L_{tot} = 1$  and  $V_{tot} = 0$  (red line). The PsbS equilibrium constants are the same for all quenching sites ( $K_{LP} = K_{VP}$ ) and the violaxanthin and lutein equilibrium constants are the same ( $K_{car} = K_{L1} = K_{L2} = K_{V2} = K_{V3}$ ). In scheme A, the PsbS-dependence of total qE sites is almost the same in the presence and absence of lutein, whereas in scheme B, removing lutein causes the number of quenching sites to saturate at a lower PsbS-dosage than wild-type. In scheme B, sites  $Q1$  and  $Q2$  are present in equal abundance, so  $Q1_{tot} = Q2_{tot} = 0.5$ .

the total number of quenching sites to go down, which is consistent with the *npq1* and *lut2* phenotypes [70, 22].

In scheme B, setting  $L_{tot} = 0$  caused the total concentration of sites to saturate at a lower PsbS value than when both carotenoids were present. This feature of scheme B could explain the lack of effect of PsbS dosage on qE levels in the *npq1* and *lut2* mutants noted in Table 3.1. The two black bars in the plots of Figure 3.7 illustrate two PsbS levels. At a lower level of PsbS, corresponding to 0.5 on the x-axis, the total concentration of qE sites with both carotenoids present is 0.49, and with only one carotenoid, the total concentration of qE sites is 0.42. At elevated levels of PsbS, the total concentration of qE sites in the presence of both carotenoids is 0.99, but in the presence of only one carotenoid, the total concentration of qE sites remains at 0.5, because half of the total qE sites require the carotenoid that is missing. In this scheme, increasing the PsbS abundance in the presence of both carotenoids increases qE capacity by a factor  $0.99/0.49 \approx 2$ , whereas increasing PsbS abundance in the presence of only one carotenoid increases qE capacity by only a factor of  $0.5/0.45 = 1.1$ , which may not be experimentally detectable.

Although scheme B appears to describe the saturation of qE with respect to PsbS abundance in the *lut2* and *npq1* mutants, it is not very effective at explaining the effects of the *lut2* and *npq1* mutants themselves. In the *npq1* mutant, qE is reduced to less than half of wild-type levels, and in the *lut2* mutant qE is reduced to approximately 3/4 of wild-type levels. However, in scheme B, the one-carotenoid qE level is 0.45, which is nearly 80% of the wild-type level. It is possible that there exists a combination of parameters that would fit scheme B to the experimental data described earlier, and these constraints could be found by fitting the predictions of scheme B to the data.

To consider a scheme that incorporates a site that depends on both lutein and zeaxanthin

into scheme B, we consider scheme C, which is illustrated in Figure 3.8. This scheme may be plausible because, as indicated by the data in Figure 3.2A, zeaxanthin-dependent and lutein-dependent qE do not seem to be completely independent of one another. In scheme C, sites  $Q1$  and  $Q2$  are the same as in scheme B, but lutein and violaxanthin (which is converted to zeaxanthin) are also able to bind to a third site,  $Q3$ , that requires both carotenoids to be capable of qE. The equations describing conservation of total qE sites in scheme C is:

$$\begin{aligned} Q1 + Q1_{Lut} + Q1_{Lut} : PsbS &= Q1_{tot} \\ Q2 + Q2_{Vio} + Q2_{Vio} : PsbS &= Q2_{tot} \\ Q3 + Q3_{Vio/Lut} + Q3_{Vio/Lut} : PsbS &= Q3_{tot} \end{aligned} \quad (3.13)$$

The equations describing the binding of carotenoids to the quenching sites are

$$\begin{aligned} \frac{Q1_{Lut}}{Q1 \times L} &= K_L \\ \frac{Q2_{Vio}}{Q2 \times V} &= K_V \\ \frac{Q3_{Vio/Lut}}{Q3 \times V \times L} &= K_{VL} \end{aligned} \quad (3.14)$$

The first two equations are the same as for schemes A and B, but the equation for carotenoids binding to  $Q3$  assumes that violaxanthin and lutein bind simultaneously, i.e. both carotenoids must be present for this “site” to be active. While this process seems unlikely to accurately describe an actual kinetic binding scheme, the quenching site  $Q3$  might possibly describe a site of aggregation-dependent quenching that only occurs in the presence of both carotenoids. It is also possible that the quenching ascribed to  $Q3$  might be located at the same site as quenching due to  $Q1$  or  $Q2$ , but is enhanced in the presence of both zeaxanthin and lutein compared to quenching by only one carotenoid.

The other conservation laws in scheme C are

$$\begin{aligned} Q1_{Lut} + Q3_{Lut/Vio} + Lut + Q1_{Lut} : PsbS + Q3_{Lut/Vio} : PsbS &= Lut_{tot} \\ Q2_{Vio} + Q3_{Lut/Vio} + Vio + Q2_{Vio} : PsbS + Q3_{Lut/Vio} : PsbS &= Vio_{tot} \\ PsbS + Q1_{Lut} : PsbS + Q2_{Vio} : PsbS + Q3_{Vio/Lut} : PsbS &= PsbS_{tot} \end{aligned} \quad (3.15)$$

Figure 3.9 shows the equilibrium concentration of total quenching sites for scheme C for the case when the abundance of sites  $Q1$ ,  $Q2$ , and  $Q3$  is equal (left) and when  $Q3$  is more abundant than  $Q1$  or  $Q2$  (right). The equilibrium concentration of quenchers in the presence of both carotenoids is very similar to that for schemes A and B, as shown in Figure 3.7. Similarly to the results for scheme B, qE in scheme C saturates at a lower *PsbS* dosage in the presence of only one carotenoid than in the presence of both carotenoids. In Figure 3.9 (right), the abundance of violaxanthin-binding sites is higher than that of lutein-binding sites, giving a higher qE value when lutein is missing (blue dashed line, which would correspond to the *lut2* mutant) than when violaxanthin is missing (red line, which would correspond to the *npq1* mutant).

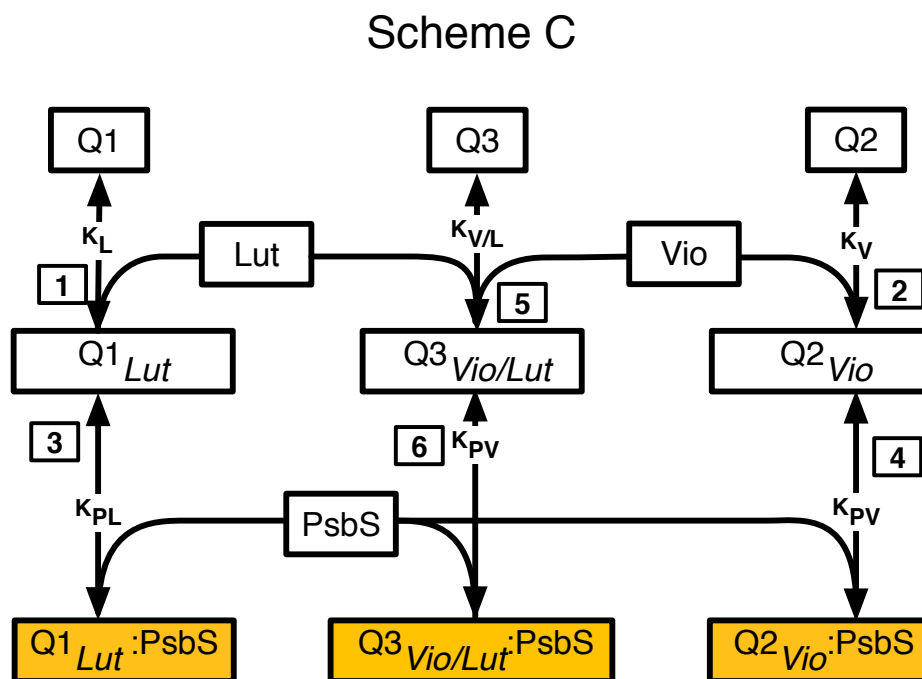


**Figure 3.8:** Scheme C, which includes a lutein-dependent qE site (Q1) a violaxanthin/zeaxanthin-dependent qE site (Q2) and a site that depends on both lutein and violaxanthin/zeaxanthin (Q3).

Figure 3.5 compares the calculated “qE capable” sites as a function of PsbS dosage with measured qE levels in *A. thaliana* mutants containing varying levels of PsbS, with data taken from reference [51]. The calculated effect of PsbS dosage on qE-capable sites is very similar for schemes A, B, and C. The x axis of the calculated results has been scaled by 2 and the y axis has been scaled by 2.5 in order to achieve the agreement with experimental data, which is reasonably good given the large noise level of the experimental data. The black lines are located at PsbS levels of 1 and 7, and could correspond to PsbS levels of wild-type and L17. In order to determine which scheme among schemes A, B, and C, is most likely to accurately describe the interaction between lutein, xanthophylls, qE sites, and PsbS, it would be useful to fit the free parameters in each scheme to the constraints described in equations 3.3 through 3.7 and to assess both how well each scheme could be fit to the constraints, as well as the robustness in free parameters to these fits. Doing such a fit is outside the scope of the current chapter but could be done using the curve fitting capabilities of MATLAB.

Identifying a scheme that accurately describes the dependence of qE expression on lutein, xanthophylls, and PsbS is useful in two ways: 1) such a scheme provides a framework for testing specific hypotheses of qE mechanism. 2) a model for interaction of PsbS, zeaxanthin, and lutein with qE sites enables the assessment of the role of qE in plant fitness [12]. For example, an accurate model for qE would enable a computational determination of the timescales over which qE is maximally beneficial to plants. It is not currently known whether the timescale over which qE matters most is seconds or minutes, and whether there is one characteristic timescale or multiple timescales. Because zeaxanthin-dependent quenching

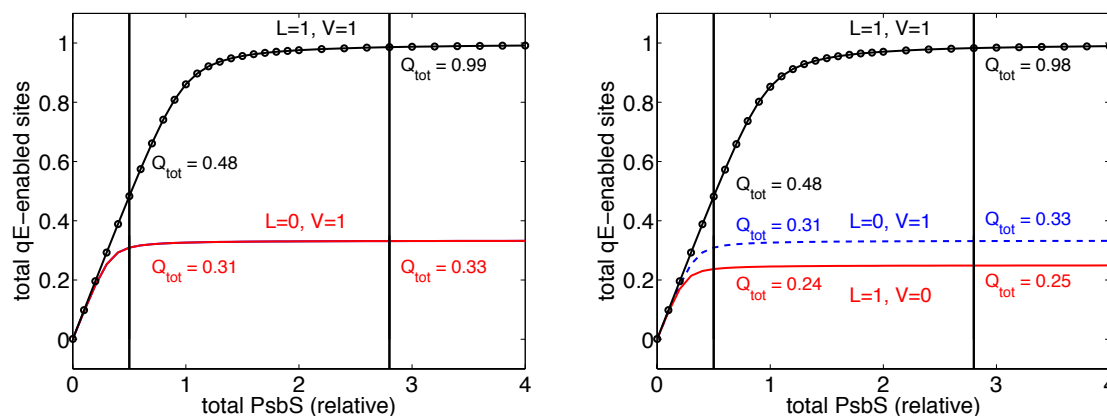


**Figure 3.9:** Sum of equilibrium concentrations of sites  $Q_{1_{tot}} : PsbS$ ,  $Q_{2_{vio}} : PsbS$ , and  $Q_{3_{vio/Lut}} : PsbS$  from scheme C for (left)  $Q_{1_{tot}} = Q_{2_{tot}} = Q_{3_{tot}} = 1/3$  and (right)  $Q_{1_{tot}} = 1/4$ ,  $Q_{2_{tot}} = 1/3$ , and  $Q_{3_{tot}} = 5/12$ . Binding constants for PsbS and carotenoids are the same as in figure 3.7. In the presence of only one carotenoid, qE levels are attenuated and saturate at a lower PsbS level than in the presence of both carotenoids.

relies on the conversion of violaxanthin to zeaxanthin, it will have a lag in its appearance compared to lutein-dependent quenching, which could give rise to two or more characteristic timescales of qE.

### 3.3 Light-intensity dependence of model

In order to develop such a quantitative understanding of the behavior of qE in fluctuating light conditions, it is necessary to be able to accurately calculate the behavior of the thylakoid membrane system at all light intensities. Because qE has been shown to be maximally useful in fluctuating light conditions, rather than in constant high light, accurately simulating the response of qE to a range of light intensities is crucial for quantifying the role qE plays in plant productivity. To this aim, in this section we present the light-intensity dependence of some quantities calculated by the model described in chapter 1 and compare the predictions of the model with experimental measurements.

Figure 3.10 (Left) shows the values of reduced  $Q_A$  that are calculated by the model at a range of light intensities and time delays after illumination. Reduced  $Q_A$  is a measure of closed reaction centers [53]. Figure 3.10 (Right) shows the values of reduced  $Q_A$  with and without qE for selected times after the onset of illumination. At 50 and 400 seconds, after qE has had time to turn on, the level of reduced  $Q_A$  is lower in the presence of quenching than in the absence of quenching. The observation that qE reduced excitation pressure at a given light intensity is consistent with excitation pressure measurements of the *npq4* mutant, which lacks PsbS and exhibits higher excitation pressure than wild type [13].

Currently, the way in which excitation pressure is measured is by using “light curves.” in which the actinic light intensity is set to a level and the qE level is measured after the system has equilibrated for 5 minutes. An example of such a light curve is given in Figure 6B of reference [13].

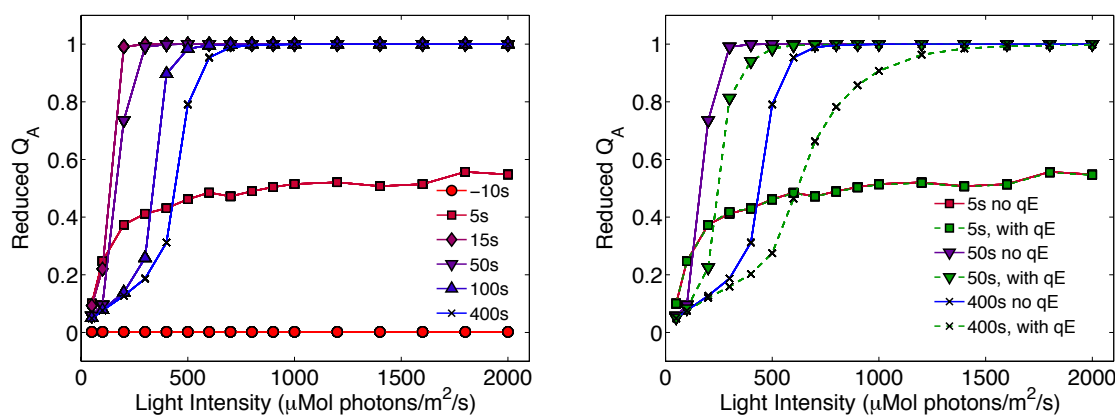


**Figure 3.10:** Left: Fraction of  $Q_A$  that is reduced, as predicted in the model described in chapter 1, at various times after transitioning from darkness to light. Right: Reduced  $Q_A$  at 5, 50, and 400 seconds after moving from dark to light, with (green dashes) and without qE. A reaction center with reduced  $Q_A$  is considered to be closed, so the fraction of reduced  $Q_A$  plotted here is proportional to the excitation pressure  $1 - qP$ [53].

Measuring excitation pressure in this way does not give an exact comparison of the predictions of the model because the initial starting point at each light intensity is the total accumulated NPQ of all previous light intensities. During the duration of the “light curve” measurement nonphotochemical quenching processes that evolve more slowly than qE[14] build up. These additional processes complicate quantitative analysis of the data. To compare the calculations shown in Figure 3.10 with experimental data, it would be necessary to measure the quantum yield of PSII (qP parameter) at 5 minutes after the onset of illumination, starting with a dark-adapted leaf for each light intensity.

If measuring excitation pressure from dark-adapted leaves gives the same result as the light curves, then the major discrepancy between model and experiment lies with the inflection point in the model that is not present in the experiment. This inflection point could be caused by an underestimation of closed reaction centers at low light intensities. One possible reason for the underestimation could be that the rate of diffusion of reduced plastoquinol through the thylakoid membrane is not incorporated directly into the model, causing the availability of oxidized plastoquinol at the reaction center to be overestimated. Another possibility is that the model for turning on the carbon cycle and ATP synthase is overly simplified, and is not completely accurate at low light intensities.

Figure 3.11 (left) shows the lumen pH predicted by the model of chapter 1 for a range of light intensities. In the first five seconds, the lumen pH drops to below 5.5 for all light intensities above  $\sim 50 \mu\text{mol photons/m}^2/\text{s}$ , then rises as ATP synthase activity turns on and dissipates the pH gradient across the thylakoid membrane. The lumen pH saturates with increasing light intensity, and the value at which this saturation occurs shifts from  $\sim 100 \mu\text{mol photons/m}^2/\text{s}$  to  $\sim 450 \mu\text{mol photons/m}^2/\text{s}$ . Figure 3.11 (right) shows a comparison of lumen pH with and without quenching at several delay times after the transition from dark to light. The model predicts that qE affects the lumen pH in a small range of light intensities between 200 and 500  $\mu\text{mol photons/m}^2/\text{s}$ , and only at longer times. Direct measurement of the lumen pH are difficult. The lumen pH has been measured in thylakoids by monitoring

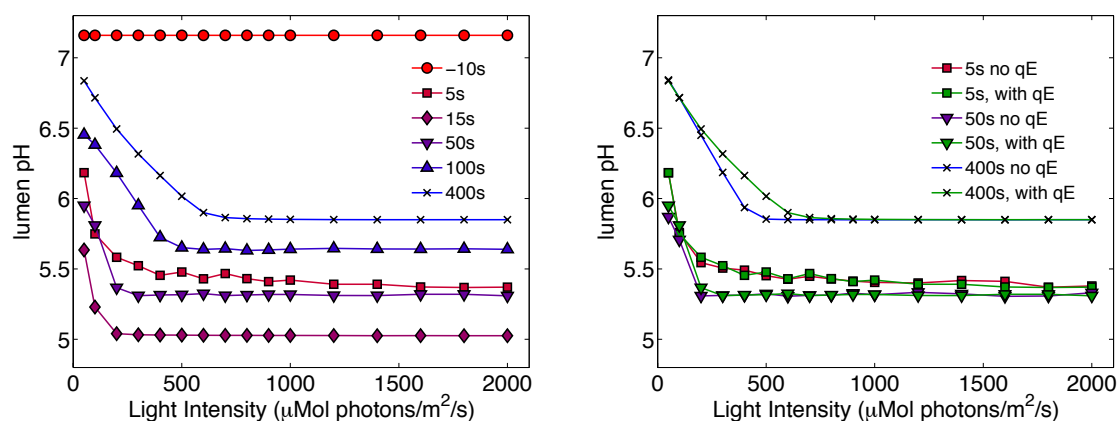


**Figure 3.11:** Left: Lumen pH, as predicted by the model presented in chapter 1, at 5, 15, 50, 100, and 400 seconds after transitioning from darkness to light. The time point at -10 s (red circles) provides a reference point for the lumen pH in the dark. Right: Comparison of lumen pH with and without quenching at 5, 50, and 400 seconds after the transition from dark to light. The lumen pH in the presence of qE is shown in green. The model predicts that qE only affect the lumen pH in a small range of light intensities between 200 and 500  $\mu\text{mol photons}/\text{m}^2/\text{s}$ , and only at longer times.

the quenching of the dye 9-aminoacridine. The  $\Delta\text{pH}$  across the thylakoid membrane can be measured indirectly by using a technique based on the measurement of the electrochromic shift across the thylakoid membrane [45], and could provide experimental data with which predictions of the model could be compared.

Figure 3.12 shows the fraction of qE sites that are active after illumination for the same illumination times as in Figure 3.11 for two qE models. Although the absolute values of qE are slightly higher in the left panel, which incorporates both zeaxanthin and lutein dependent quenching, the light intensity dependence for both qE mechanisms is that qE saturates above 500  $\mu\text{mol photons}/\text{m}^2/\text{s}$ . This model can be compared with experimental measurements of “light curves” of qE, as shown in Figure 3.13, with data taken from Figure 6A of reference [13]. In the experimental data, the saturation of qE is not as steep as in the model predictions, though this could be due to differences between how the simulation is performed and how the light curve experiment is made.

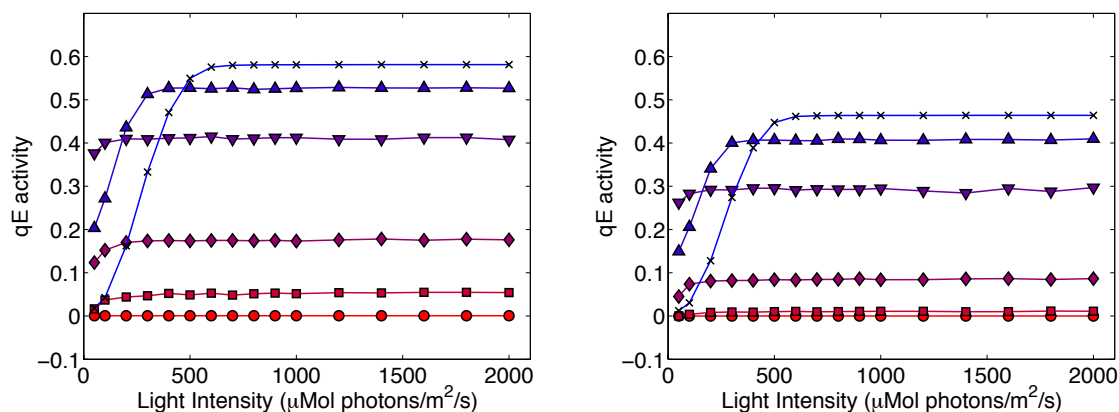


**Figure 3.12:** Values of total active quenchers at various times after illumination for a range of light intensities. The illumination times are the same as in Figure 3.11. Left: Model where qE is due to zeaxanthin and lutein, with a ratio of 1:1. Right: model where qE is only due to zeaxanthin.

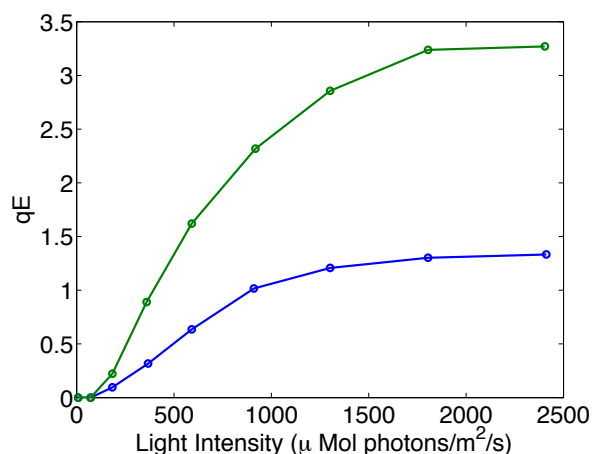


**Figure 3.13:** qE for different light intensities for wt (blue) and L17 (green), as measured by a “light intensity curve” using a PAM fluorometer. Data taken from figure 6B of reference [13], and the qE value shown in the figure was calculated by subtracting the light curve for the *npq4* mutant from the light curves for wild type and L17.

### 3.4 Conclusion

In this chapter we have presented several schemes that could provide a model for qE that can account for qE in mutants with altered carotenoid and PsbS compositions. At this point, these schemes are highly speculative and only provide a possible theoretical approach to understanding the interaction of carotenoids and PsbS to facilitate qE. Any attempt to discriminate between the schemes presented here would need to reconcile conflicting experimental data [80, 81]. We have also presented the light-intensity dependence of closed reaction centers, lumen pH, and qE calculated from the model in Chapter 1, and have compared these calculated results with experiments.

# Chapter 4

## Transient Absorption Spectra of a pH-Sensitive Dye

### Contents

---

4.1	Introduction . . . . .	62
4.2	Transient absorption measurement . . . . .	65
4.3	Results . . . . .	68
4.4	Discussion . . . . .	69

---

### 4.1 Introduction

The regulation of light harvesting that is successfully done in photosynthetic organisms has recently been implemented in an artificial biomimetic system [18]. An array of porphyrins was covalently bonded to a pH-sensitive dye, as illustrated in Figure 4.1. In low pH, the dye effectively quenches fluorescence from the porphyrin, whereas in high pH the dye does not affect the lifetime of the five porphyrins. In their unquenched state, the porphyrins are able to participate in electron transfer with fullerenes [83].

pH-activated nonphotochemical quenching (NPQ) in photosynthetic organisms protects photosystem II from photoinhibition [13]. Analogously, a regulated quencher of excited states of porphyrins or other light harvesting molecules should protect the light harvesting molecules from inhibition due to long-lived excited states. In order to be effective at avoiding damage due to long-lived excited states, it is necessary for the quencher dye itself to rapidly dissipate energy, and to do so in a manner that does not lead to degradation. In this chapter, we present transient absorption measurements of the pH-sensitive dye used in reference [18] as a quencher of excitation energy, with the aim of characterizing its excited state dynamics to inform on its suitability for increasing the lifetime and stability of organic light harvesting devices.

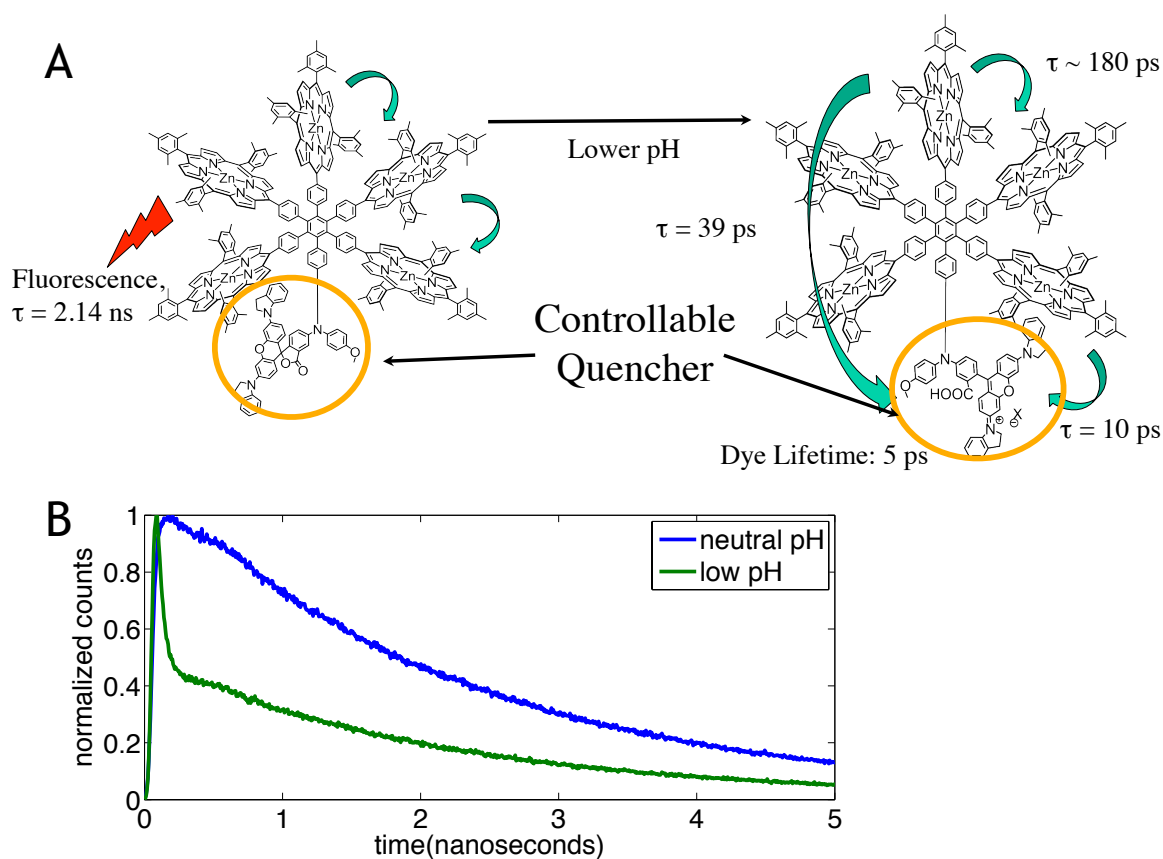


**Figure 4.1:** a) Schematic of hexad molecule [18] that can reversibly transition from a state with a long lifetime (2 ns) to a state with a short lifetime (<50 ps) by changing the pH of the solvent. The transition is accomplished by the quenching dye (circled in orange) which is colorless in neutral solution and blue in acidic solution. b) Time-resolved fluorescence of the porphyrin moiety in neutral (blue) and acidic (green) solution.

Figure 4.2 shows the structure of the pH-sensitive dye in its spirolactone form, which it assumes at neutral pH, and open, absorbing form, to which it converts when the pH is lowered. Figure 4.3 shows the linear absorption of the dye in acidic conditions, during which the lactone ring is open and the dye is chemically similar to rhodamine dyes [84]. In this form the dye absorbs visible light and is able to quench excitation energy from other excited molecules such as porphyrins [18].

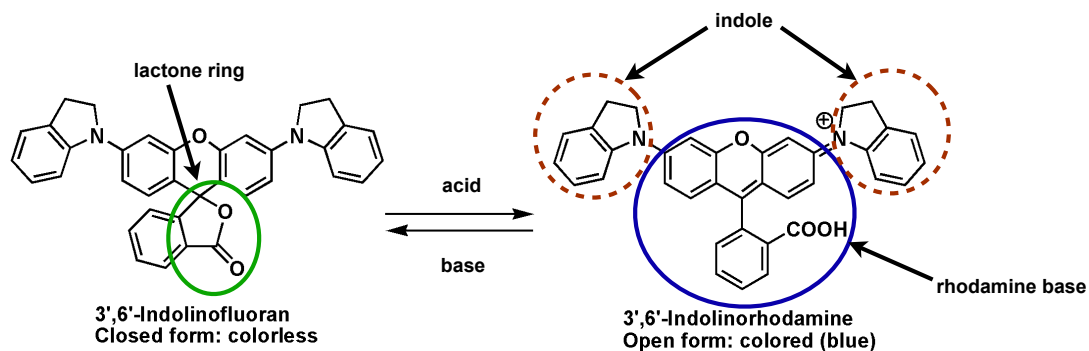


**Figure 4.2:** Chemical structure of pH sensitive dye. The rhodamine and indole groups of the colored form are circled .

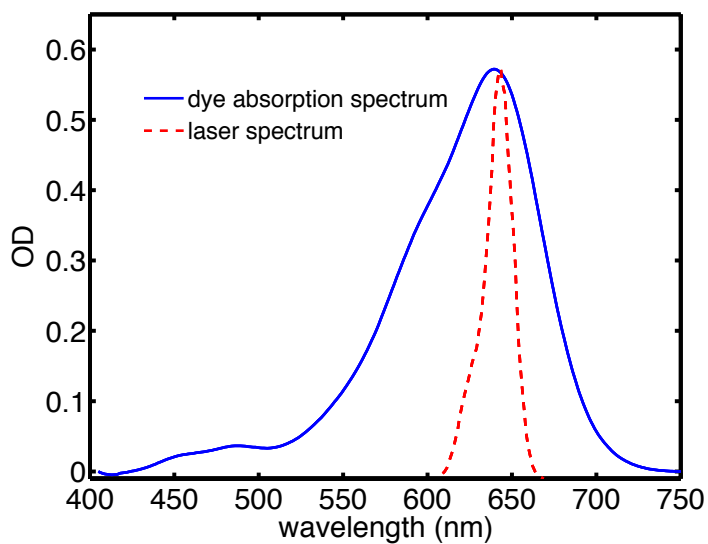


**Figure 4.3:** Linear absorption of indolinorhodamine dye (solid blue line) and of spectrum of the pump pulse (dashed red line).

## 4.2 Transient absorption measurement

Transient absorption experiments on the open form of the dye were conducted with a 640 nm pump and a broadband probe. The pump spectrum is shown along with the linear absorption of the sample in figure 4.3. A schematic of the experimental layout is shown in Figure 4.5. The source for the pump was an optical parametric amplifier (Coherent OPA 9040) pumped by a 250- kHz Ti:Sapphire regenerative amplifier (Coherent RegA 9050). The pump pulse was compressed to  $\sim 40$  fs with two SF10 prisms that largely compensated for the group velocity dispersion in the optical system. The probe was supercontinuum generated in sapphire, ranging from 460 nm to  $\sim 1200$  nm generated from focusing  $\sim 300$  mW of the 800 nm fundamental in a 2 mm sapphire crystal. The probe light was filtered with a short pass filter (SPF750 or SPF700, CVI-Melles Griot) to attenuate the intense fundamental beam. The pump and probe were spatially overlapped at the sample. The pump was focused to a spot  $200 \mu\text{m}$  in diameter and the probe was focused to a spot  $100 \mu\text{m}$  in diameter. Before the sample, a portion of the probe was split off with a beamsplitter (Thorlabs BSW16) into a reference beam, which passed through the sample but did not overlap with the pump. The probe was frequency-resolved with a spectrometer (Acton Research 300i) and detected by a CCD camera (Princeton Instruments NTE2). The integration time of the camera was typically set to 200 ms. The time between the pump and probe was controlled by translating a retroreflector mounted on an optical delay stage (Newport Nanomover). The sample was dissolved in ethanol to an optical density of 0.6 in a 0.5 mm quartz cuvette. The pump power was kept below 4 nJ /pulse.

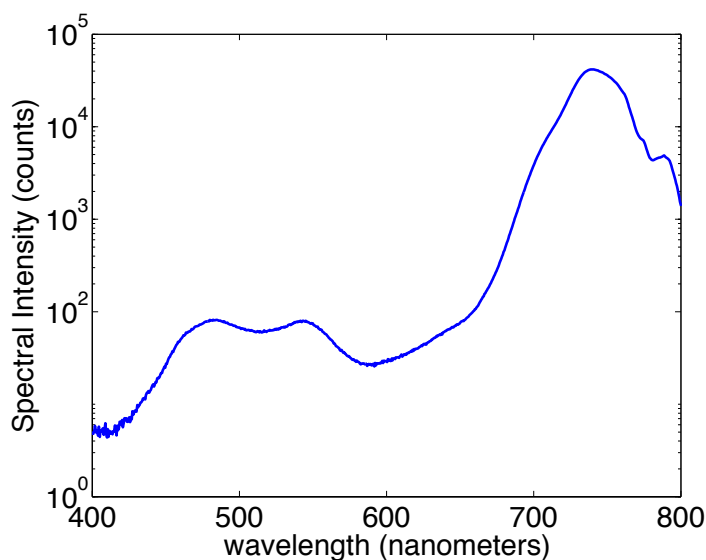


**Figure 4.4:** Spectrum of the probe light generated in a 2 mm sapphire window, without spectral filtering.

After the sample, the probe and reference filtered with a Schott KG-5 glass, which absorbs infrared light but transmit visible light. This was done to make the relative intensities of different wavelengths in the probe more uniform, which improved the signal-to-noise ratio

(SNR) at the CCD detector. The reason for this improvement is that the readout noise at the CCD camera is constant, so a higher signal level corresponds to a higher SNR because the noise due to the CCD readout is a smaller portion of the signal. Because the dynamic range of the CCD is between  $\sim 200$  counts at baseline to  $\sim 65500$  counts at saturation, variations in probe intensity by more than two orders of magnitude limit the signal to noise at any one wavelength. Because the intensity spectrum of the super continuum generated by sapphire varies over five orders of magnitude in the spectral range used for the experiment (460-750 nm), as shown in Figure 4.4, using the KG-5 glass as a “whitening filter” to smooth the probe spectrum improved the SNR.

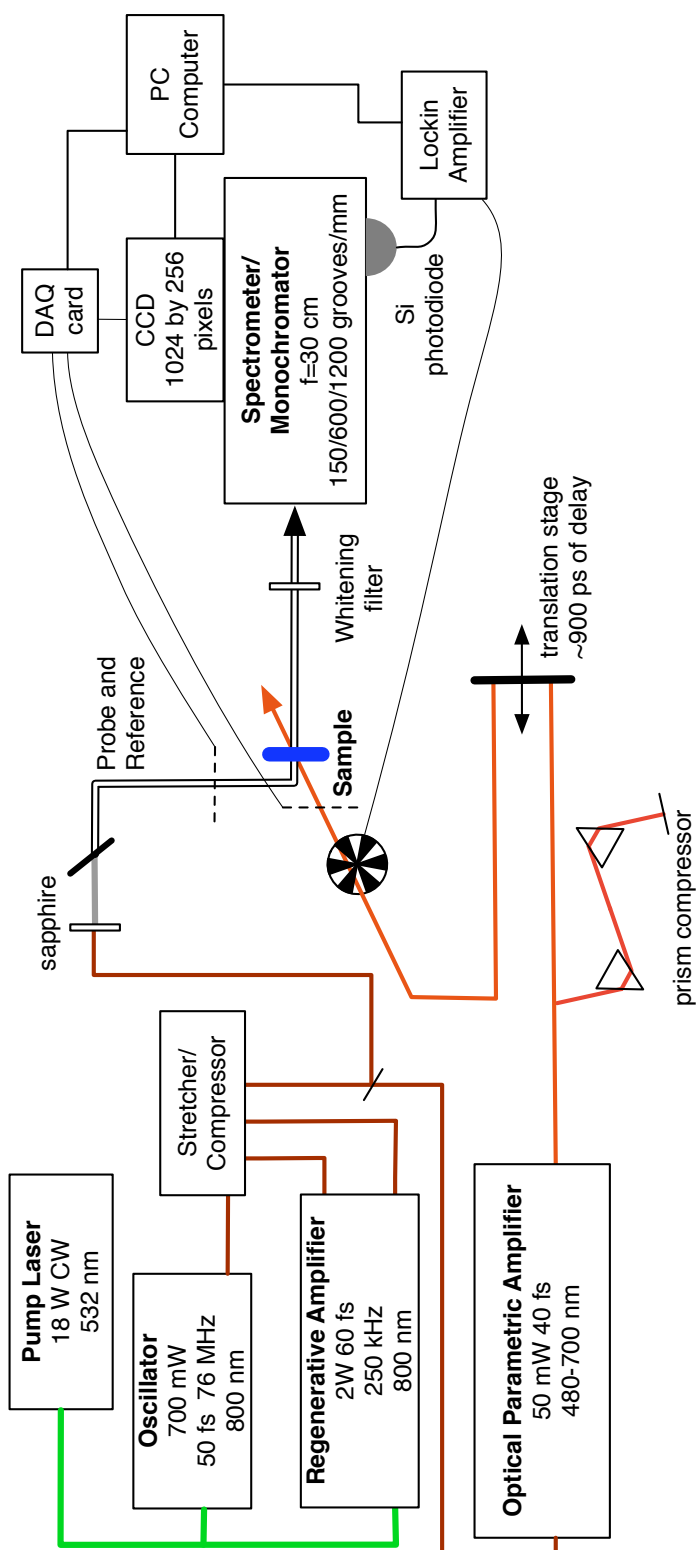
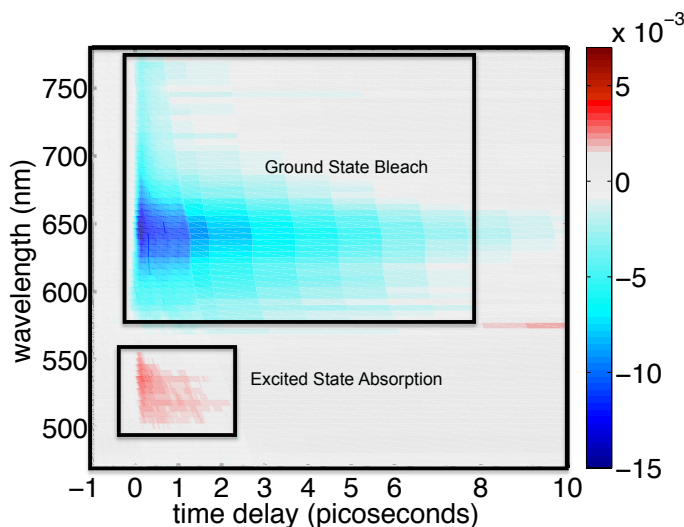


Figure 4.5: Layout of transient absorption setup used for this experiment.

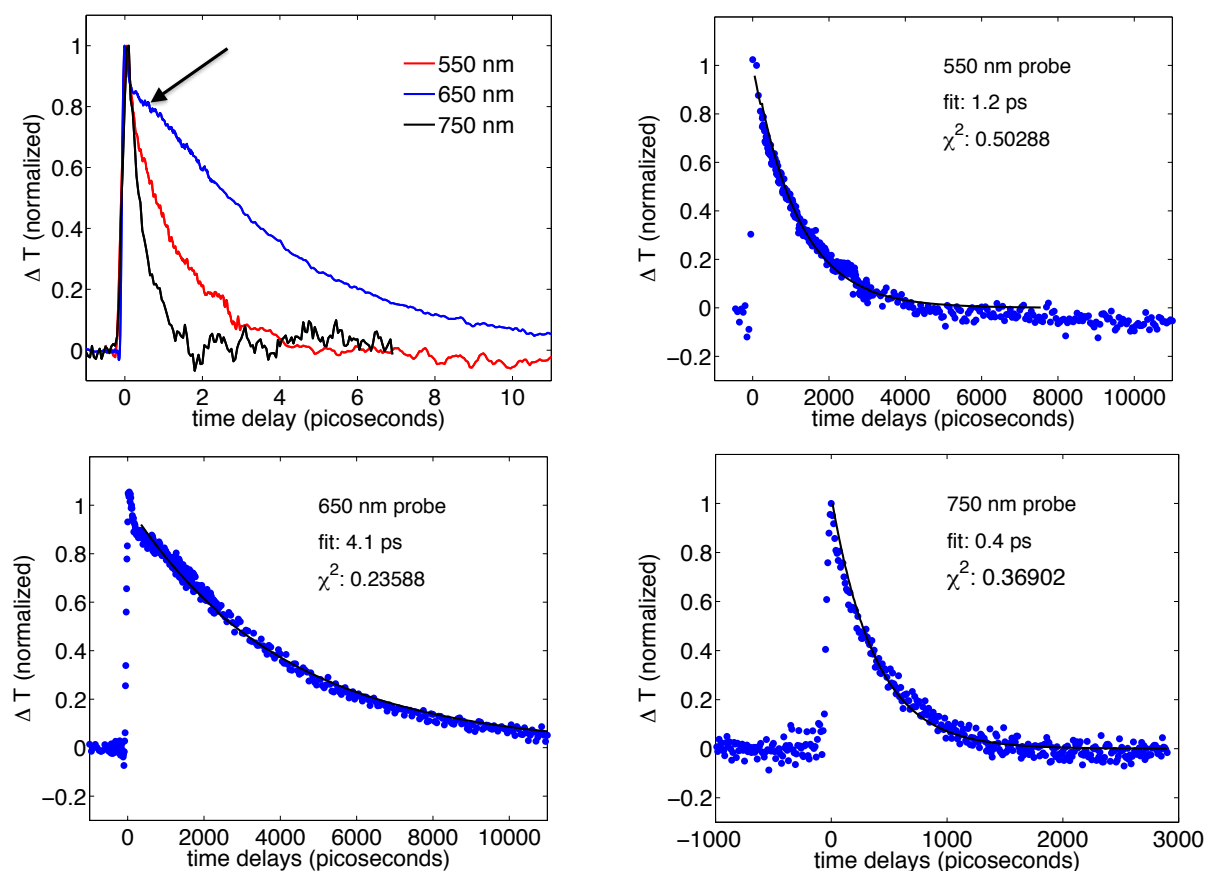
### 4.3 Results

Figure 4.6 shows the transient absorption spectrum of the open, colored form of the dye following excitation at 640 nm. The dye exhibits a negative signal corresponding to a ground state bleach (shown in blue) in the detection region from 580 nm to 780 nm, and exhibits a positive feature corresponding to an excited state absorption (shown in red) in the range from 500 nm to 550 nm. The negative signal is primarily due to ground state bleach, possibly with contributions from stimulated emission at early times. The portion of the bleach signal above 700 nm and the excited state absorption signal at 550 nm both decay much more quickly than the main bleach signal centered at 640 nm. The more rapid decays at these other wavelengths compared to the timescale of ground state recovery suggest that the excited state of the dye decays by some mechanism other than internal conversion from the first excited state to the ground state, since direct decay into the ground state should yield the same timescales for excited state dissipation and ground state recovery.



**Figure 4.6:** Transient absorption spectra of the colored form of the dye (3'-6'-indolinorhodamine). The units on the color bar are in optical density (OD). The positive signals (red) correspond to excited state absorption, and the negative signals (blue) correspond to stimulated emission or ground state bleach.

Figure 4.7 (top left) shows transient absorption traces at 550, 650, and 750 nm measured with a lock-in amplifier, which gives a better signal-to-noise ratio than the CCD camera. The solid lines are fits of the data to a single exponential. The transient absorption at 650 nm, which corresponds to the ground state bleach at the pump wavelength, decays on a timescale of 4.1 ps. The discrepancy between this measurement and the value of 5 ps we reported in reference [18] is likely due to differences in the extent to which the sample was purged with nitrogen, since we observed the dye's lifetime to decrease in air (data not shown). The signal at 650 nm (bottom left) exhibits a rapid decay at early times followed by a plateau. The rapid decay matches the decay of signals at 550 nm and 750 nm at early times, suggesting that it



**Figure 4.7:** Top left: Slices of transient absorption signal at probe wavelengths of 550 nm, 650 nm, and 750 nm. Top right: fit to data at 550 nm. Bottom left: fit to data at 650 nm Bottom right: fit to data at 750 nm.

could be due to stimulated emission from the S1 state. The decay at longer times is due to the recovery of the ground state bleach signal. The plateau could be attributed to absorption of a vibrationally hot state or to shifting of the excited state spectrum. More detailed fitting of the spectra to a kinetic model could help in assigning the plateau to a specific state, but is outside the scope of this chapter. The rapid decay of the negative signal at 750 nm compared to 650 nm could be attributed to the rise of a positive signal in that region, which has been observed in triphenylmethane dyes [85].

## 4.4 Discussion

It is striking that the colored form of the indolinorhodamine dye is chemically similar to rhodamine dyes, yet has a much shorter lifetime than most rhodamine dyes, which typically have a nanosecond lifetimes [84, 86, 87]. The features in the transient absorption spectrum of the indolinorhodamine dye, specifically the excited state absorption in the 500-600 nm region and the shorter timescale of ground state bleach in 700+ nm of the spectrum, are

similar to those observed in triphenylmethane dyes such as crystal violet and malachite green [85, 88, 89], and are also similar to the dye rhodamine 110 [90].

The timescale of decay of the excited state absorption signal (1.2 ps) is much faster than the timescale of decay of the ground state bleach signal (4.1 ps), suggesting that the excited state of the indolinorhodamine dye is dissipated through a third state rather than through internal conversion directly to the ground state. Although no excited state absorption other than the feature at 500-600 nm was observed, it is possible that the molecule relaxes to a vibrationally hot ground state whose absorption band is 680 nm. Similar relaxation to a hot ground state has been proposed as a dissipation mechanism in malachite green [85, 91]. The plateau observed at  $\sim 1$  ps in the transient absorption spectrum at 650 nm probe data (indicated with an arrow in Figure 4.7) has also been observed in the dyes malachite green and ethyl violet [92], further supporting the idea that an intermediate state is present.

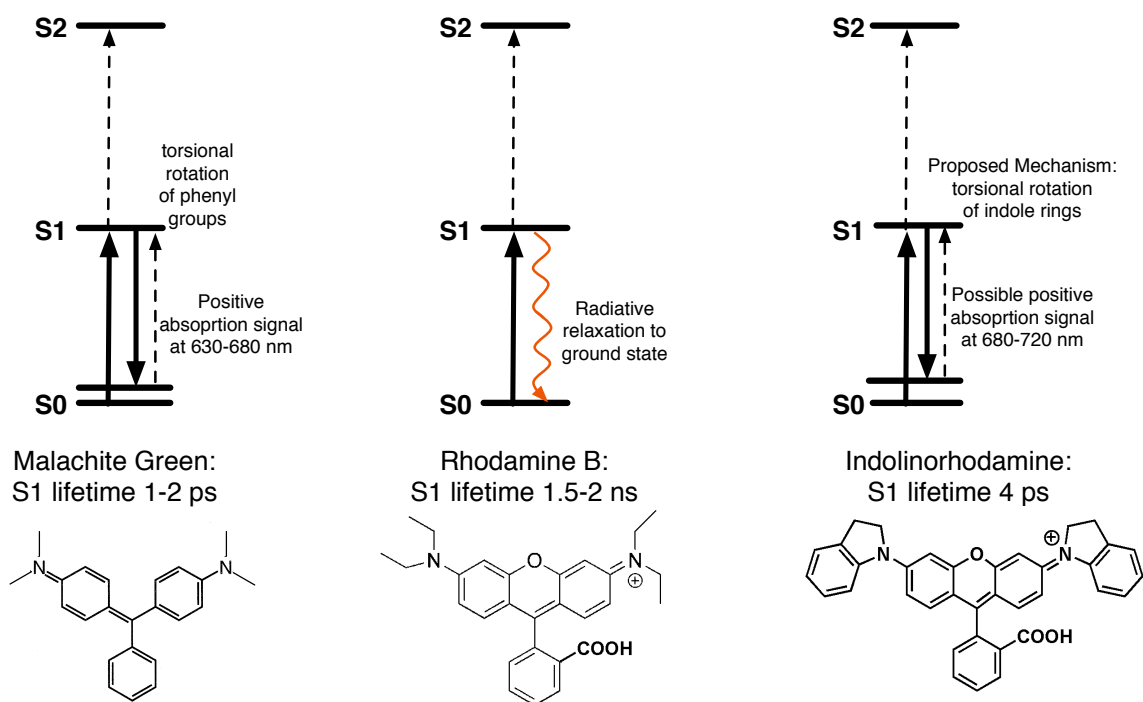


**Figure 4.8:** Molecular structures, energy levels, and lifetimes of malachite green (a representative triphenylmethane dye), rhodamine B (a representative rhodamine dye), and the indolinorhodamine dye measured here. The solid black lines represent processes in the molecules and the dashed lines represent signals that are detected in the transient absorption experiment. The positive absorption signal in malachite green between 630 nm and 680 nm is clearly seen in reference [85].

Figure 4.8 shows chemical structures and simple energy level diagrams of malachite green, rhodamine B, and the indolinorhodamine dye. It is interesting that, while the molecule measured here is chemically similar to rhodamine dyes, its excited state lifetime is closer to that of triphenylmethane dyes such as malachite green and crystal violet lactone [88].

It has been suggested that the short lifetime of triphenylmethane dyes is caused by rota-

tional diffusion of the phenyl groups [93], so by analogy it is possible that the short lifetime of the dye studied here is also due to rotation of the indole groups. This hypothesis would be supported if the dye exhibited any fluorescence at low temperature, or in a solvent of greater viscosity than ethanol, such as glycerol.

Understanding the mechanism of deactivation of these dyes is important for the long-term goal of being able to design molecules that could be switched on to protect light harvesting devices from photodamage. Triphenylmethane dyes such as malachite green and crystal violet are somewhat susceptible to degradation, as characterized by studies of their lightfastness [94], and it is possible that the indolinorhodamine dye presented here may also be susceptible to degradation by a similar mechanism. Given that the objective of integrating quenching dyes into solar cell devices is to extend the overall lifetime of the device, it will be important for quenching dyes themselves to be photochemically stable.

# Chapter 5

## Effect of Bridge on Charge Separation of Molecular Donor-Acceptors

### Contents

---

<b>5.1</b>	<b>Introduction</b>	<b>72</b>
<b>5.2</b>	<b>Methods</b>	<b>73</b>
5.2.1	Steady state measurements	73
5.2.2	Time-resolved fluorescence	74
5.2.3	Transient absorption measurement	75
<b>5.3</b>	<b>Results</b>	<b>76</b>
5.3.1	Steady state absorption and fluorescence	76
5.3.2	Time-resolved measurements	76
5.3.3	PDI and HTH components	77
5.3.4	Processes in HTH-PDI junctions	80
<b>5.4</b>	<b>Effect of bridge properties</b>	<b>97</b>
5.4.1	Kinetic scheme	97
<b>5.5</b>	<b>Conclusion</b>	<b>100</b>
<b>5.6</b>	<b>Fits of fluorescence lifetime data</b>	<b>102</b>

---

### 5.1 Introduction

Controlling charge separation on an intramolecular scale in molecular donor-acceptor junctions is important for increasing the efficiency of organic solar cell devices [95, 96]. In particular, donor- $\pi$ -acceptor molecules are gaining popularity as sensitizers in dye-sensitized solar cells owing to their low cost and strong absorption cross sections [3, 97, 98]. The effect of the connection between electron donor and electron acceptor materials on the efficiency and

yield of charge separation and charge recombination is still a topic of ongoing investigation [99]. To assess the effect of conjugation, length, and rigidity of the bridge between donor and acceptor on charge separation and recombination, we studied the excited state dynamics of molecular donor-acceptor complexes that were synthesized to have four different bridges.

Both the donor and the acceptor are popular candidates in organic photovoltaics: hexa(3-hexylthiophene) (HTH) is the donor, has high charge mobility and visible light absorption; perylene-diimide (PDI) and naphthalene-diimide (NDI) are well-known n-type semiconductors possessing high thermal and optical stability. Furthermore, PDI absorbs visible light in the spectral region where HTH does not, enhancing the total absorption cross section of the system. The nature of the bridges was conjugated (PN1: benzene ring and PN4: benzene acetylene derivative), flexible non-conjugated (PN2: ethylene,  $\text{CH}_2\text{CH}_2$ ), and rigid non-conjugated (PN3: trans-1,4-cyclohexane). The molecular structure of the molecules and absorption and emission spectra of the donor and acceptor components are shown in Fig. 5.1.

## 5.2 Methods

### 5.2.1 Steady state measurements

UV-vis spectra were measured with a Varian Cary 50 spectrometer. Emission spectra were measured with the Varian Cary Eclipse Spectrometer. Solvents used were toluene, chloroform, and N,N-dimethyl formamide (DMF). Fluorescence quantum yields following excitation at 410 nm, which is the peak of the thiophene absorption, were calculated by comparison with freshly sublimated 9,9-diphenylanthracene in cyclohexane ( $\Phi = 0.90$ ).

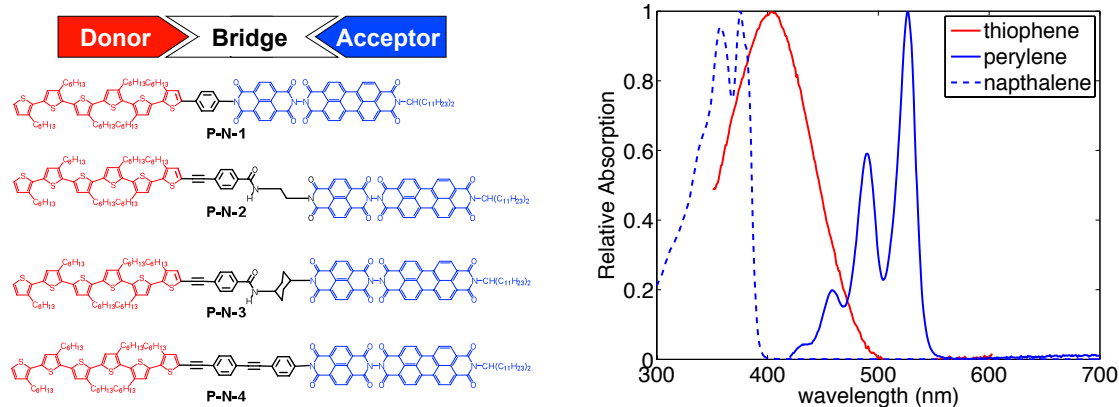


**Figure 5.1:** Left: Chemical structure of PN molecules. The electron donor (red) is a hexathiophene and the electron acceptor (blue) is a dimer of perylene diimide (solid blue line) and naphthalene diimide (dashed blue line). Right: Absorption spectra of hexathiophene donor (blue) and PDI-NDI acceptor (red). B. Fluorescence spectrum of donor (blue) and acceptor (red).

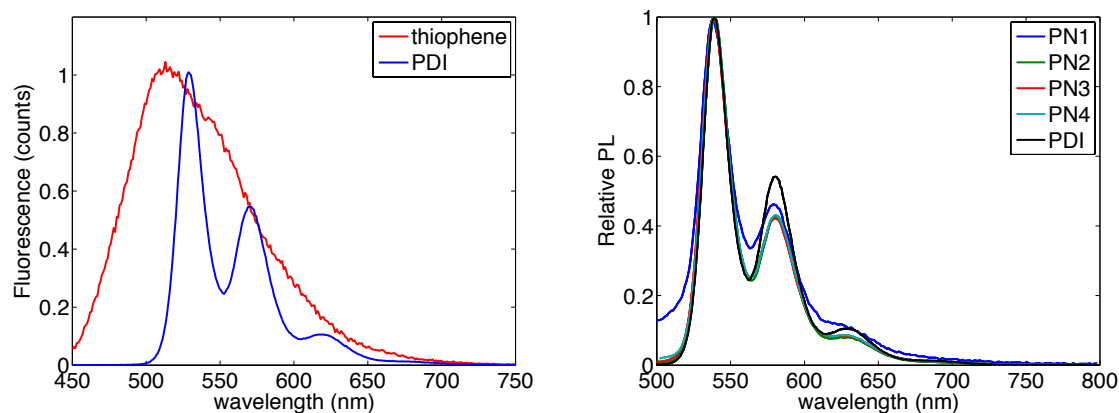


**Figure 5.2:** Left: Fluorescence of hexathiophene (HTH) and PDI. Right: fluorescence of PDI and PN molecules. The emission at the 580 nm and 630 nm peaks is attenuated in PN2, PN3, and PN4 compared to emission of the most intense peak at 540 nm. In PN1, the entire emission spectrum is broadened.

## 5.2.2 Time-resolved fluorescence

Fluorescence lifetimes of molecules PN1, PN2, PN3, and PN4 were collected using time-correlated single photon counting (TCSPC). A mode-locked Ti:Sapphire oscillator (Mira 900F, Coherent) pumped by a diode-pumped, frequency-doubled Nd:YVO<sub>4</sub> laser (Verdi V-10, Coherent) generated  $\sim 150$  fs pulses with a repetition rate of 76 MHz and was tuned to 820 nm with a full width at half-maximum (FWHM) of 12 nm. This output was frequency doubled to 410 nm using a 1-mm-thick beta barium borate (BBO) crystal. The energy at the sample was 10 pJ/pulse. The fluorescence emission was sent through a polarizer set at magic angle ( $54.7^\circ$ ). The fluorescence was then sent through a spectrograph (Newport 77400-M) and detected with a 16-channel photomultiplier tube detector (Becker-Hickl PML-16C), which was connected to a SPC-630 (Becker-Hickl) photon coating card plugged into a PC computer. The fluorescence was detected in 16 channels spaced 12 nm apart, and the center

wavelength was set to 531 nm to match the peak of fluorescence from the PDI. The spectral width of each channel was 1 nm. The detector was controlled using a DCC-100 detector control (Becker-Hickl). The FWHM of the instrument response function (IRF), measured with dilute non-dairy creamer, was 150 ps. The samples were dissolved in solvents of varying dielectric constant (toluene ( $\epsilon = 2.38$ ), chloroform ( $\epsilon = 4.8$ ), and N,N-Dimethylformamide ( $\epsilon = 38$ ) to have an optical density of 0.1 at 407 nm in a 1 cm quartz cuvette (Starna Cells).

### 5.2.3 Transient absorption measurement

TA experiments were conducted with a tunable pump and a broadband probe. The source for the 525 nm pump (to excite the PDI acceptor) was an optical parametric amplifier (Coherent OPA 9040) pumped by a 250- kHz Ti:Sapphire regenerative amplifier (Coherent RegA 9050), seeded by a Ti:Sapphire oscillator (Coherent Mira Seed) that was pumped by a diode-pumped, frequency-doubled Nd:YVO<sub>4</sub> laser (Verdi V-18, Coherent). The amplified output was frequency-doubled to produce the 400 nm pump (to excite the HTH donor). The probe was white light supercontinuum ranging from 460 nm to 1200 nm generated from focusing 300 mW of the 800 nm fundamental in a 2 mm sapphire crystal. The pump and the probe beams were focused at the sample position to a spot having a diameter of 200  $\mu\text{m}$  (pump) and 100  $\mu\text{m}$  (probe). The transmitted pump beam was blocked after the sample, and the probe was frequency-resolved with a spectrometer (Acton Research 300i) and the transient absorption signal was collected with a high-speed silicon photodiode (Thorlabs) connected to a lock-in amplifier (Stanford Research Systems). The lock-in amplifier was synchronized by an optical chopper (New Focus 3501) in the pump beam. The time delay between the pump and probe beams was controlled by translating a retroreflector mounted on an optical delay stage (Newport Nanomover).

For TA pump-probe measurements, molecules were dissolved in toluene to an OD of  $<0.5$  in a 0.5 mm cuvette and flowed by a peristaltic pump at room temperature. The energy of the pump was 5-10 nJ/pulse. Kinetic traces were collected at the following wavelengths: 540 nm, 580 nm, 680 nm, 720 nm, 750 nm, and 820 nm. The time delay was varied between -10 ps and 900 ps, which was limited by the length of the delay stage. The 525 nm pump was compressed to 40-60 fs using a pair of SF10 prisms. The 400 nm pump was not compressed. The cross correlation between the pump and the probe was not measured directly, but was evaluated by measuring a transient absorption signal in CS<sub>4</sub> at several probe wavelengths (data not shown). This measurement places an upper bound on the cross-correlation between pump and probe. We measured this upper bound to be 800 fs for the 400 nm pump. The kinetic traces were globally fit using the MATLAB statistics toolbox package.

## 5.3 Results

### 5.3.1 Steady state absorption and fluorescence

The absorption and emission spectra of molecules PN1-PN4 are shown in Figure 5.3. The fluorescence yield of the molecules at 540 nm following excitation of the thiophene at 410 nm is shown in Table 5.1. The absorption spectra of the perylene diimide portion (450 - 560 nm) of the molecules are the same for all molecules. The absorption of PN2 and PN3, which have non-conjugated bridges, are similar in toluene and DMF. PN1 and PN4 both contain conjugated bridges, so the difference in their absorption spectra is likely due to differences in bridge length.

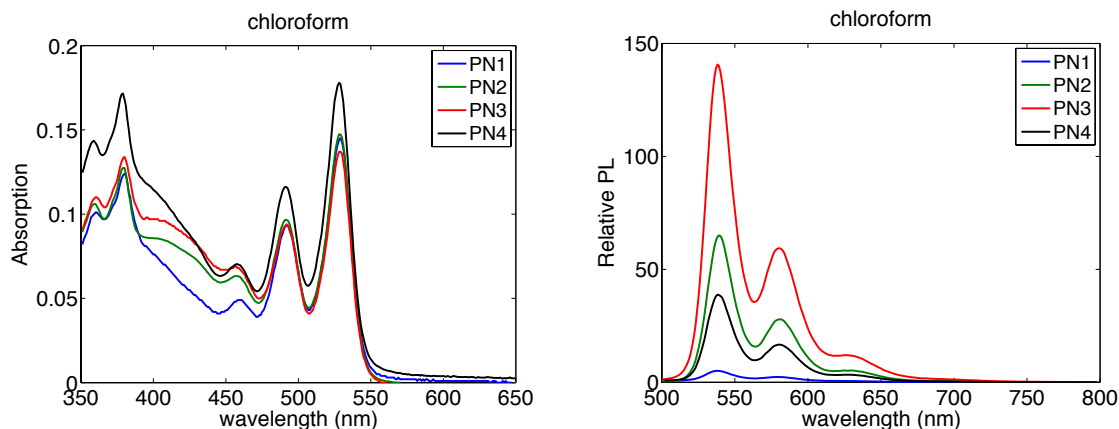


**Figure 5.3:** Absorption (left) and emission (right) of PN1, PN2, PN3, and PN4 in chloroform.

### 5.3.2 Time-resolved measurements

We performed transient absorption measurements to assess the rate and yield of formation of charge-separated states in the PN molecules. Figure 5.6 shows a schematic summarizing the excited state processes in the HTH and PDI components alone.

**Table 5.1:** Fluorescence yield of molecules PN1 - PN4 in various solvents

bridge type	toluene	chloroform	DMF
PN1	4.4 %	2.9 %	1.5 %
PN2	32.5 %	18.2 %	1.8%
PN3	67.5 %	63.4 %	2.5 %
PN4	30.3 %	14.0 %	2.1 %

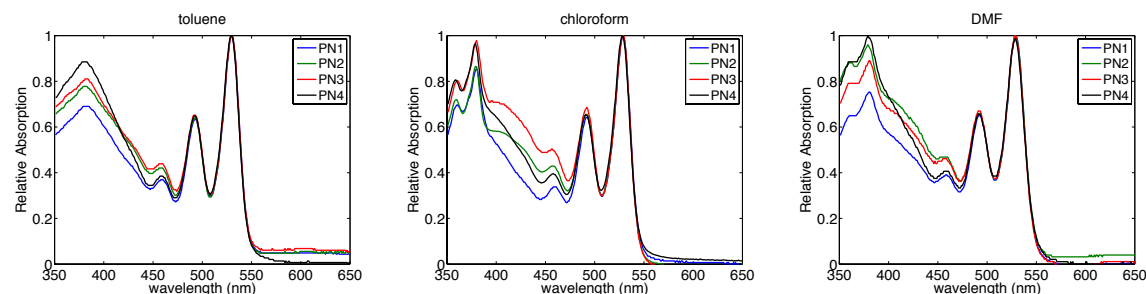


**Figure 5.4:** Normalized absorption spectra of PN1, PN2, PN3, and PN4 in toluene (left), chloroform (center), and DMF (right).

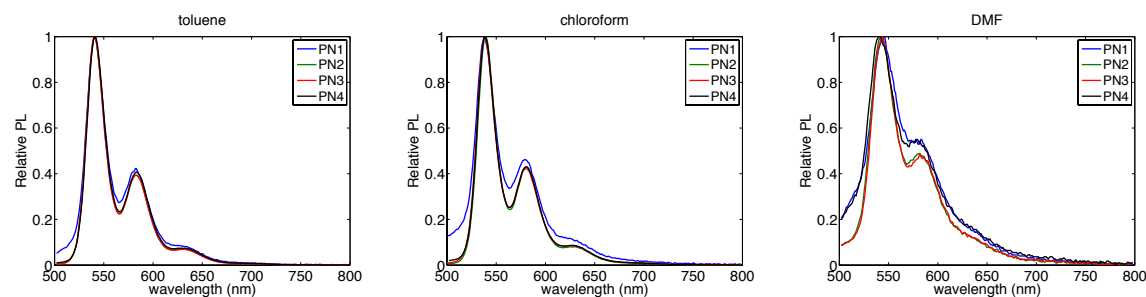


**Figure 5.5:** Normalized fluorescence spectra of PN1, PN2, PN3, and PN4 in toluene (left), chloroform (center), and DMF (right). In all solvents, PN1, which has a short conjugated bridge, exhibits a broader spectrum than other molecules. In DMF, which is the most polar of the solvents, PN4 is broadened similarly to PN1.

### 5.3.3 PDI and HTH components

The transient absorption spectra of the molecules contain contributions from ground state bleach, stimulated emission, and excited state absorption of the donor, the acceptor, and any charge transfer state that is formed. Figure 5.7 shows the transient absorption of the PDI moiety dissolved in toluene 2 ps after 525 nm excitation. There are two negative features at 540 nm and 580 nm, corresponding to ground state bleach and stimulated emission, and a broad positive feature centered at 680 nm, corresponding to excited state absorption of PDI. These features have been observed by others [100]. PDI in solution has a fluorescence lifetime of 3.6 ns (data not shown).

Unlike the excited state of PDI, the HTH excited state undergoes numerous processes on its own. Characterizing these processes before examining the dynamics of HTH-PDI donor-acceptors is needed. Reference [101] has studied the time-dependent optical properties of oligothiophenes. Although the HTH in our study contains six thiophene rings, its absorption matches the absorption of the 5T molecule in reference [101] that contains five thiophene rings rather than the 6T molecule of reference [101] that contains six thiophene rings. The 6T molecule has an absorption spectrum with a peak at 440 nm, whereas the 5T molecule has absorption with a peak at 420 nm, which is closer to the peak of the HTH. This discrepancy could be due to the fact that the thiophene oligomers in reference [101] did not contain alkyl side chains, but the HTH used here contains alkyl side chains that enhanced solubility. It is possible that steric interaction between adjacent alkyl sidechains reduced the effective

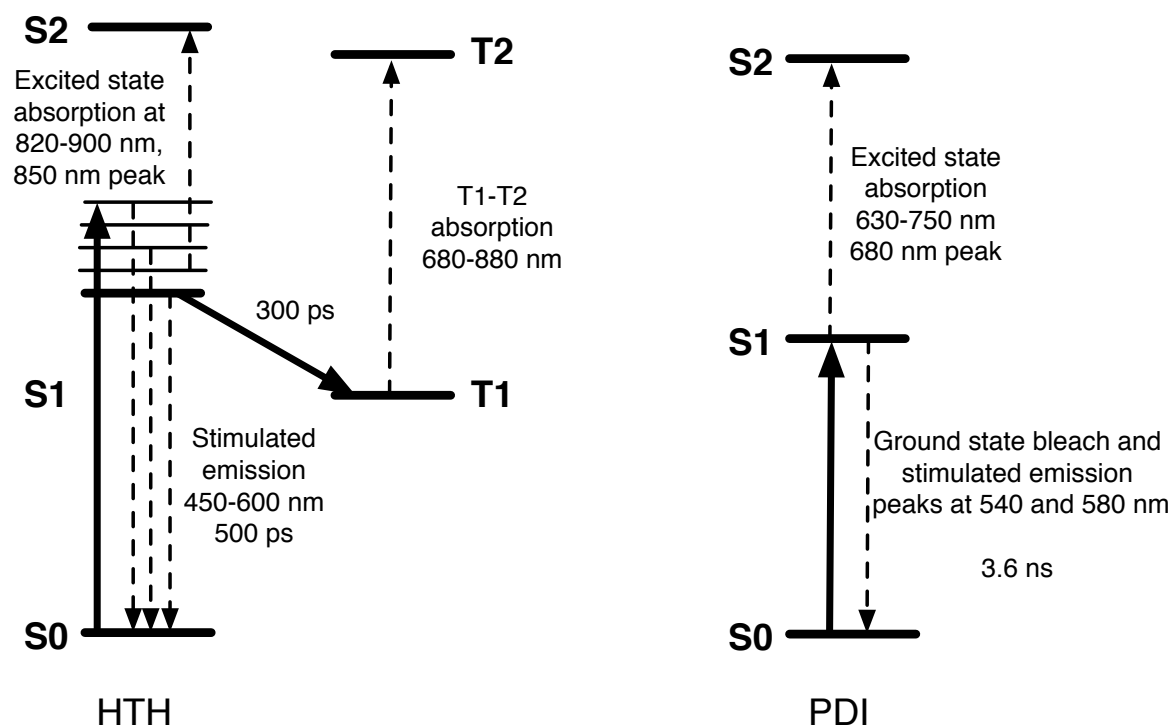


**Figure 5.6:** Processes following excitation in isolated HTH and isolated PDI that are observed in time-resolved fluorescence and transient absorption measurements. HTH exhibits a rearrangement that leads to a red-shift of its fluorescence spectrum, then undergoes intersystem crossing to the triplet state.

conjugation length of the HTH.

The peak of HTH absorption is 410 nm and peak of HTH emission is 500 nm. This large Stokes shift occurs on the timescale of several picoseconds. Figure 5.8 shows time resolved fluorescence of HTH at 459, 496, 546, 596 nm, which were fit to lifetimes of 260 ps, 380 ps, and 460 ps, and 488 ps. The fits along with residuals are shown in the appendix. The fluorescence lifetime of HTH was found to be the same in the solvents toluene, chloroform, and DMF. Because these solvents have a wide range of dielectric constants, the lack of solvent dependence suggests that charge separation is not involved in the deactivation of the isolated HTH molecule.

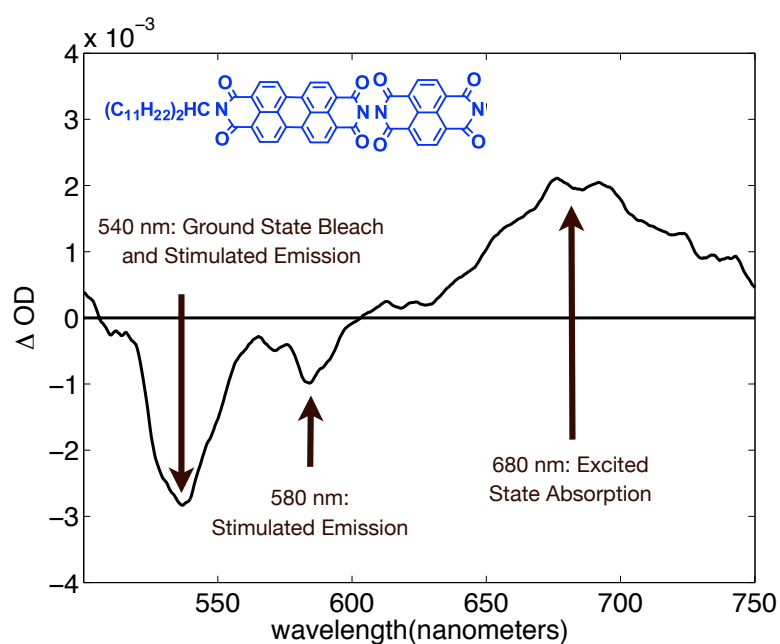


**Figure 5.7:** Transient absorption spectrum of PDI in toluene 2 ps after excitation at 525 nm.

Figure 5.9 (left) shows the transient absorption spectra of the HTH moiety dissolved in toluene after excitation at 400 nm and probed in the near-IR region between 800 nm and 900 nm at 1 ps, 5 ps, and 50 ps following excitation. The transient absorption in this wavelength region exhibits a single broad band. Initially the band has a peak at 845 nm, but within 2 ps the amplitude of the band grows and the peak shifts to 855 nm. The position of the peak does not change in the remaining 50 ps of the measurement. Transient absorption spectra were not collected for delay times larger than 50 ps. Figure 5.9 (right) shows a kinetic transient absorption trace of HTH probed at 850 nm. The trace can be fit to two rise times of 460 fs and 24 ps and one decay time of 300 ps. The 460 fs rise time could be associated with the width of the laser pulse, since the 400 nm probe was not compressed. The 24 ps rise times is probably associated with the the solvation of the excited state. The excited state absorption peak at 850 nm is consistent with the excited state absorption (A1 band) of the 5T molecule, which has five thiophene rings, observed in reference [101]. The 300 ps decay time matches the timescale of fluorescence from the HTH, and is therefore most likely the timescale of decay of the excited state, which undergoes intersystem crossing to the triplet state. The triplet state of 5T (five thiophene rings) absorbs between 550 and 680 nm, with a peak at 620 nm, as shown in Figure 4 of reference [101]. The triplet state of 6T1 (six thiophene rings with an alkyl side chain) absorbs between 600 and 800 nm, with a peak at 680 nm [101].

### 5.3.4 Processes in HTH-PDI junctions

Figure 5.10 shows the decay of fluorescence of the molecules PN1-PN4 and the HTH donor in toluene following excitation at 407 nm. Fits of these data to a sum of exponentials are given in Section 5.6. At the blue edge of the measured fluorescence (496 nm), where HTH emits,

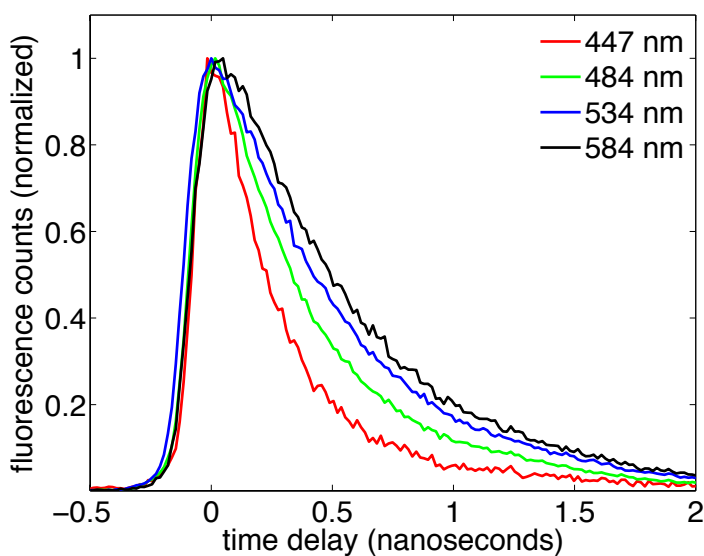


**Figure 5.8:** Normalized fluorescence lifetime curves of HTH in toluene following 410 nm excitation. Emission wavelengths are 447 nm, 484 nm, 534 nm, and 584 nm, and were fit to lifetimes of 260 ps, 380 ps, 460 ps, and 488 ps, respectively.

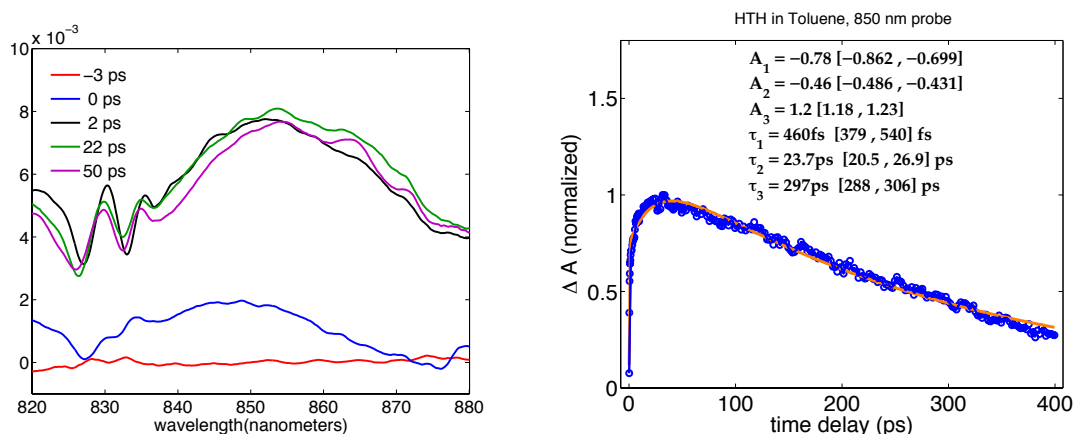


**Figure 5.9:** Left: Transient absorption spectrum of HTH in toluene 2 ps after excitation with a 400 nm pump, probed in the near-IR region. Right: transient absorption signal of HTH probed at 850 nm fit to a sum of three exponentials. The numbers in square brackets after the fit parameters are the 95 % confidence interval for those parameters.

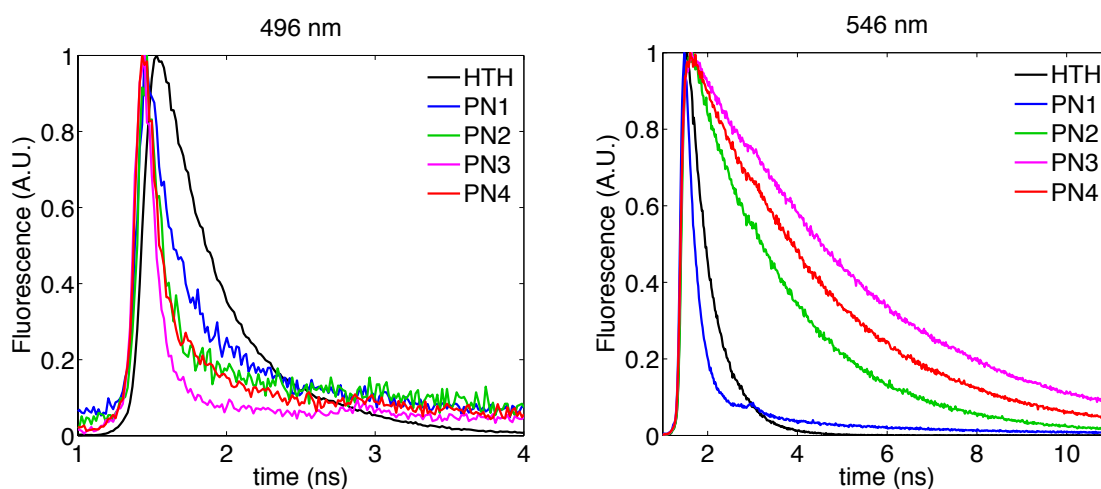


**Figure 5.10:** Time-resolved fluorescence decays in toluene of molecules PN1, PN2, PN3, and PN4, along with the hexathiophene donor (HTH), measured at 496 nm and 546 nm. The excitation wavelength was 410 nm.

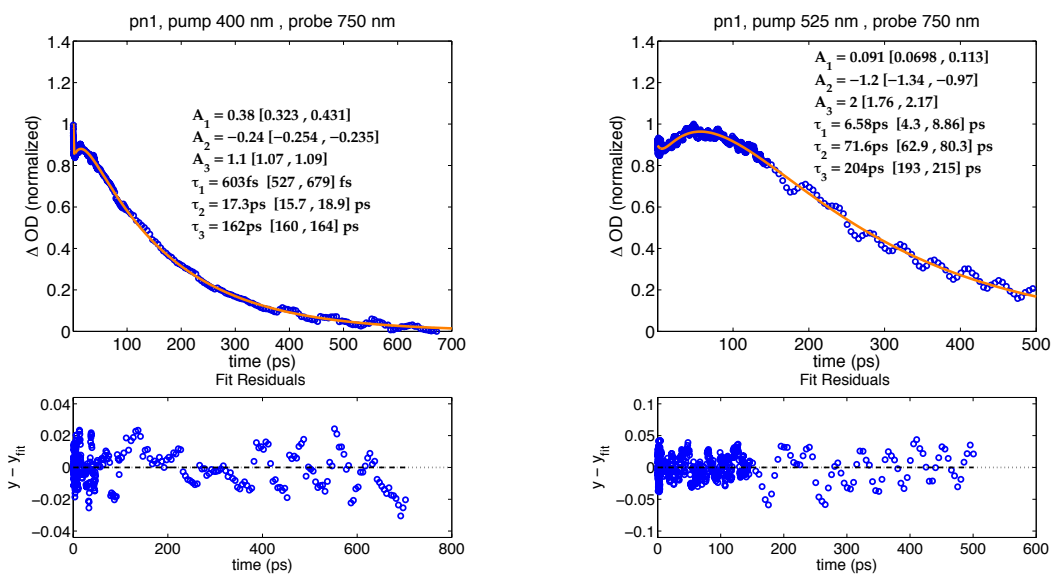


**Figure 5.11:** Transient absorption of PN1 probed at 750 nm, following excitation at 400 nm (left) and 525 nm (right).

all of the PN molecules have a shorter lifetime than HTH, suggesting that intramolecular processes such as energy transfer and charge separation occur from excited HTH to PDI. At 530 nm and higher, both HTH and PDI have some fluorescence. The fluorescence lifetime of PN2, PN3, and PN4 at 546 nm are longer than the fluorescence lifetime of the HTH, and are dominated by emission from the PDI. The fluorescence lifetime from PN1 is shorter than fluorescence from HTH, indicating that the excited state of PDI is highly quenched in PN1.

To investigate the origin of this quenching in PN1, we performed transient absorption measurements. Figure 5.11 shows the transient absorption kinetics at 750 nm of PN1 following excitation of the HTH at 400 nm and the PDI at 525 nm. The PDI anion absorbs at 750 nm [102, 103], and the amplitude of the excited state absorption of the PDI nm is low enough at 750 nm that the rise timescale, which we attribute to the PDI anion, can be clearly seen. The pump probe traces of both molecules were fit to a sum of three exponentials. Following excitation at 400 nm, the three timescales were 600 fs, 17 ps, and 160 ps. The 600 fs timescale is attributed to the decay of the HTH excited state. The 17 ps rise is attributed to the appearance of the  $\text{HTH}^+\text{-PDI}^-$  charge separated state, and the 160 ps timescale is attributed to the decay of this state. When the sample is excited at 525 nm, the pump probe signal exhibits a decay of 6 ps that has a small amplitude, followed by a rise of 70 ps and a decay of 200 ps. We assign the rise time measured here to the appearance of the PDI anion, which can be formed from either excited HTH or excited PDI. The rise times for the anion signal are faster for 400 nm excitation than for 525 nm excitation. The difference in timescales could be due to differences in reorganization energy between the charge separated and the excited states of HTH and PDI. Regardless, it is clear that the PDI anion, identified by the absorption at 750 nm, is formed both HTH and PDI excited states.

Unlike in PN1, the PDI anion does not seem to form from the excited state of PDI in PN2, PN3, or PN4. Figure 5.12 shows the transient absorption signals at 750 nm in PN2;

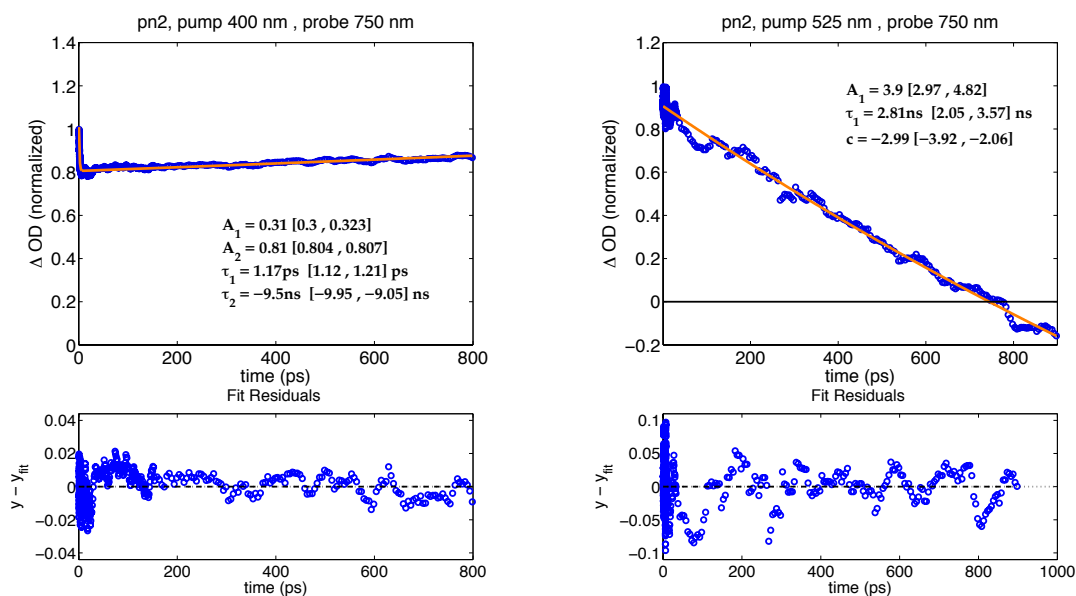


**Figure 5.12:** Transient absorption of PN2 probed at 750 nm after excitation at 400 nm (left) and 525 nm (right).

Figure 5.13 shows the transient absorption signals at 750 nm in PN3; and Figure 5.14 shows the transient absorption signals at 750 nm in PN4. In all three of these molecules, when the molecule is excited at 525 nm (right panel), the signal decays on a timescale of 1-2 ps and does not exhibit a rise that would be associated with the PDI anion. These fits clearly show that all pump probe signals following excitation at 525 nm in PN2, PN3, and PN4 decay back to the ground state and can be fit to one rapid (5-10 ps) timescale and one timescale of 1-2 ns. When excited at 400 nm, the signal at 750 nm in PN2, PN3, and PN4 initially decays on a timescale of 1.2 ps, 6 ps, and 1.5 ps, respectively, which is associated with dissipation of the HTH excited state, mostly to energy transfer from HTH to PDI. Following this rapid decay, the transient absorption signal at 750 nm in PN3 decayed with a much slower timescale of 7 ns. In PN2 and PN4 the transient absorption signal at 750 nm exhibited a slow rise which resembles the transient absorption signal of HTH alone. The signal of HTH alone is shown in Figure 5.15.

Overall, it appears that the short, conjugated bridge in PN1 facilitates charge separation from the excited state of both HTH and PDI, which have complementary absorption spectra in the visible region. The longer bridges in PN2, PN3, and PN4 do not seem to facilitate charge separation from the excited state PDI, and may also inhibit charge separation from HTH. It is notable that the lifetimes following excitation at 525 nm, which we attribute to the decay of the PDI excited state, exhibit a faster decay than the measured fluorescence lifetimes. This accelerated decay could be due to concentration quenching of the PDI, since the samples for transient absorption measurements were  $\sim 40$  times more concentrated than the samples for fluorescence measurements.

In the following sections, the available data for each molecule is summarized and discussed in the context of scheme 5.16, though the scheme does not seem to explain all of the data.

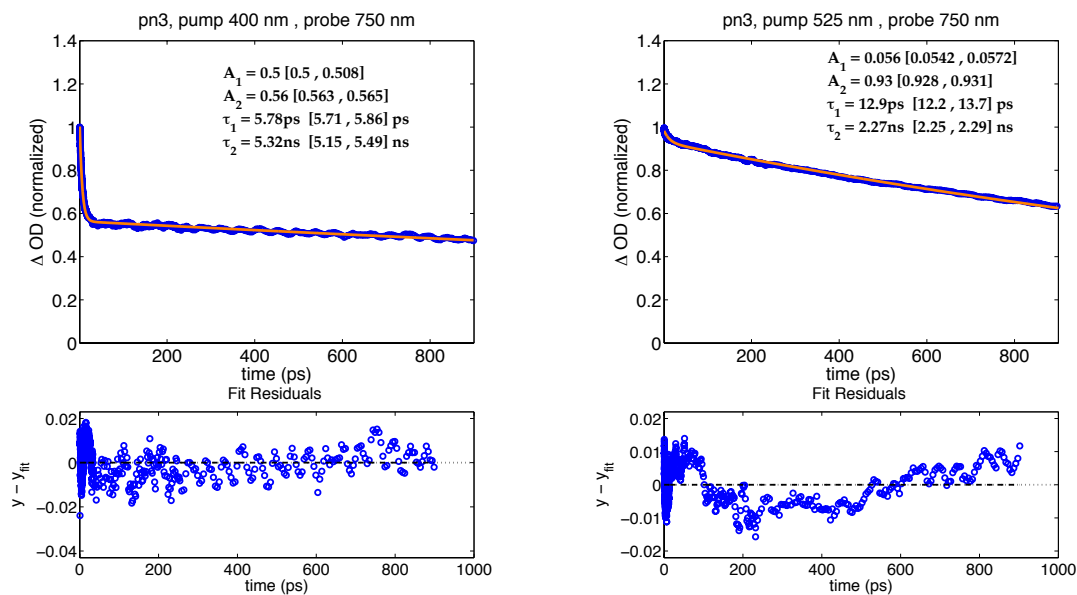


**Figure 5.13:** Transient absorption of PN3 probed at 750 nm after excitation at 400 nm (left) and 525 nm (right).

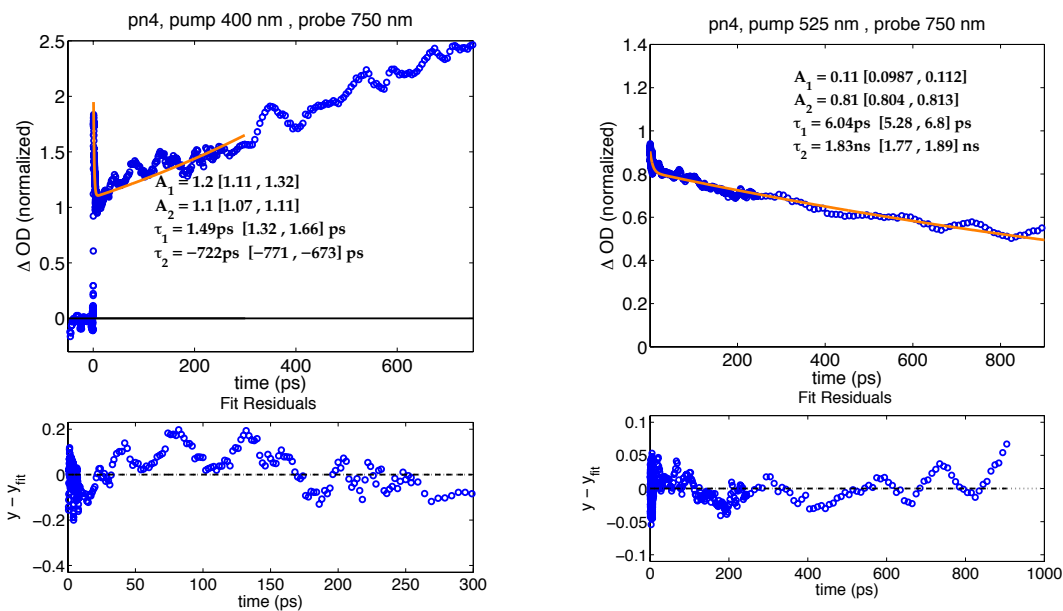


**Figure 5.14:** Transient absorption of PN4 probed at 750 nm after excitation at 400 nm (left) and 525 nm (right).

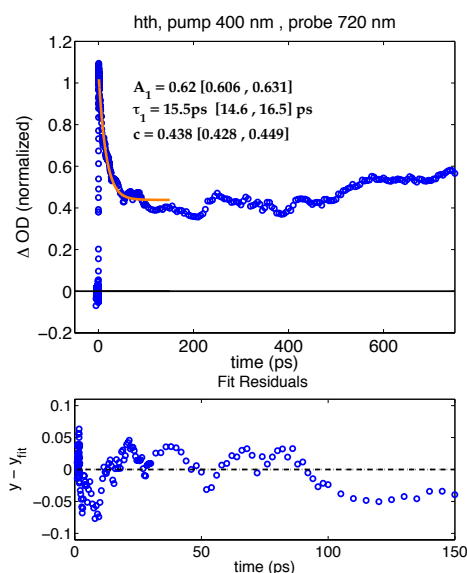


**Figure 5.15:** Transient absorption signal of HTH excited at 400 nm and probed at 720 nm.

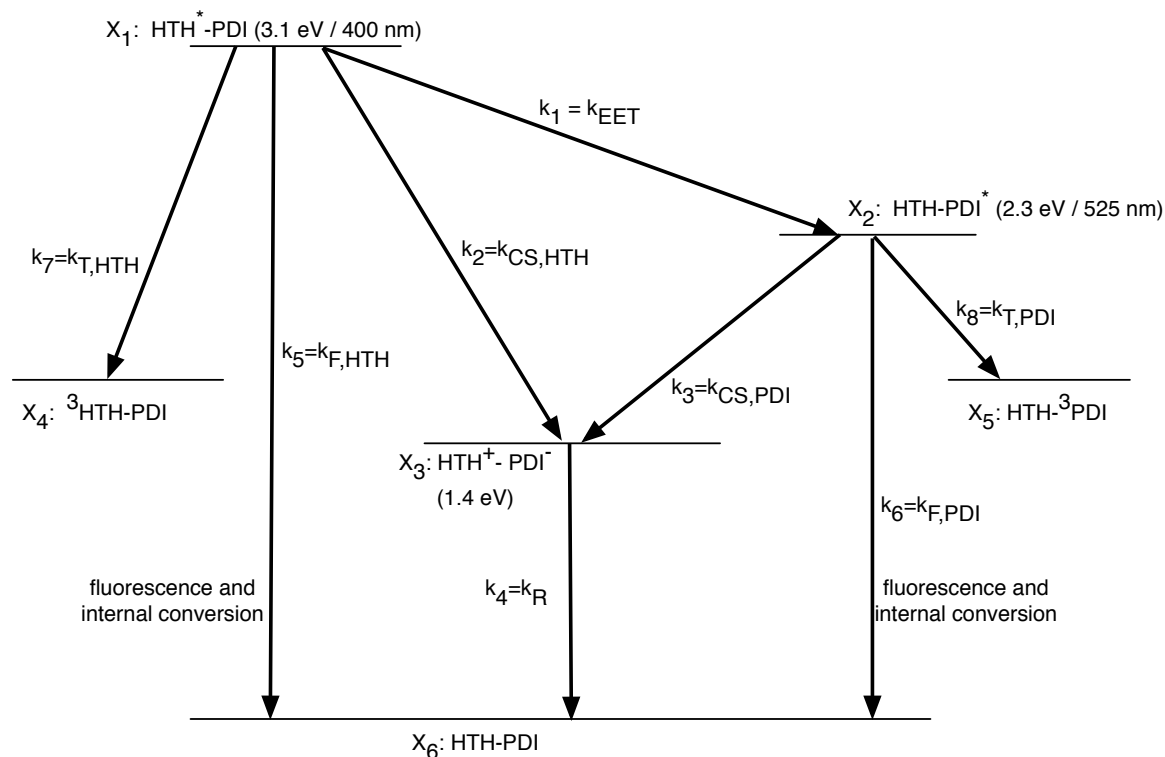


**Figure 5.16:** Decay processes within molecules following excitation. The relative rates of charge separation from HTH vs PDI depend strongly on the bridge. The energy of the charge separated state (1.4 eV) is known from cyclic voltammetry, which was performed on these molecules in chloroform, and also is discussed in reference [100]. This schematic assumes that vibrational relaxation on PDI does not affect any of the rates shown.

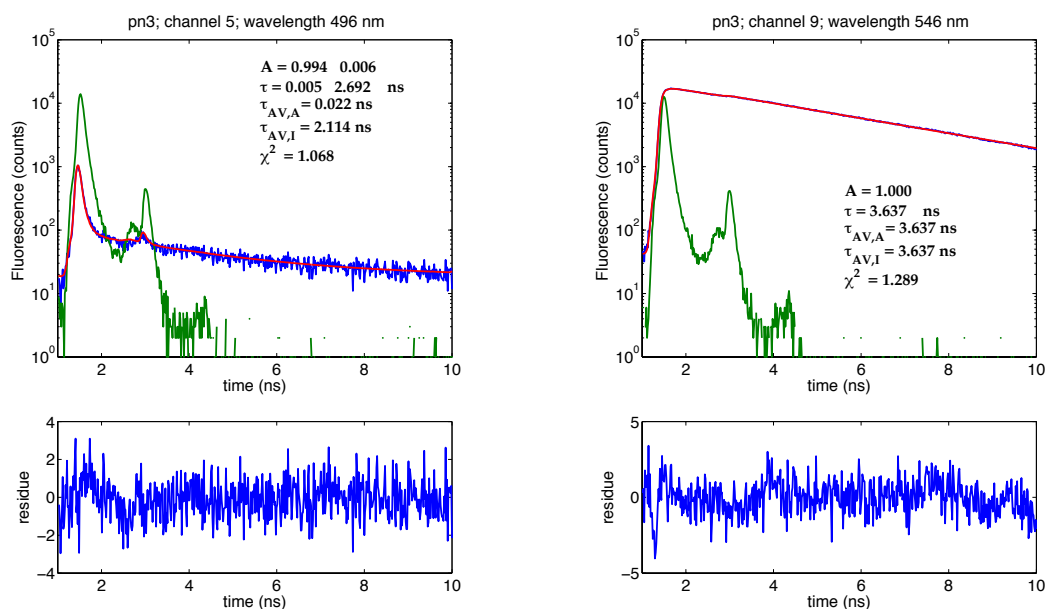


**Figure 5.17:** Fluorescence from PN3 detected at 496 nm (left) and 546 nm (right) following excitation at 410 nm.

### PN3

PN3, which has a rigid, non-conjugated bridge, exhibits the highest fluorescence quantum yield of all the molecules. Figure 5.17 shows the fluorescence lifetimes of PN3 measured at 496 nm (left) and 546 nm (right). The excited state of HTH in PN3 decayed on a timescale of 5 ps, which was the fastest decay time of all the molecules. Because the excited state of HTH alone is hundreds of picoseconds, we assign this 5 ps timescale to energy transfer to the PDI. At 530 nm and higher, PN3 decayed with a lifetime of 3.6 ns, which is equal to the excited state lifetime of PDI, suggesting that in PN3, no charge separation occurs from the PDI excited state. It is possible that some charge separation occurs from the HTH excited state in PN3.

To assess this possibility we turn to transient absorption measurements. The PDI anion absorbs at 720 nm- 750 nm, and that signal has been used by others to characterize the formation of the PDI anion [104, 100]. The HTH and PDI excited states also absorb in that region. Figure 5.18 shows the transient absorption signal of PN3 probed at 720 nm. This signal initially exhibits a rapid decay with a timescale of 5 ps. This timescale matches with the decay of the the HTH fluorescence and can therefore be attributed to energy transfer from HTH to PDI. The signal at 720 nm was also fit to a 20 ps rise and a 7 ns decay. It is possible that the 20 ps timescale corresponds to the formation of a charge separated state, and the 7 ns timescale corresponds to the decay of this state. It is also possible that part of the absorption at 750 nm is due to the HTH triplet, which does not decay on the timescale of the experiment.

The formation of a charge separated state between the HTH and PDI depletes the ground state of the PDI, and contributes to a bleach signal at 540 nm. The probe signal at 540 nm, where PDI exhibits a ground state bleach and both HTH and PDI have some emission, was

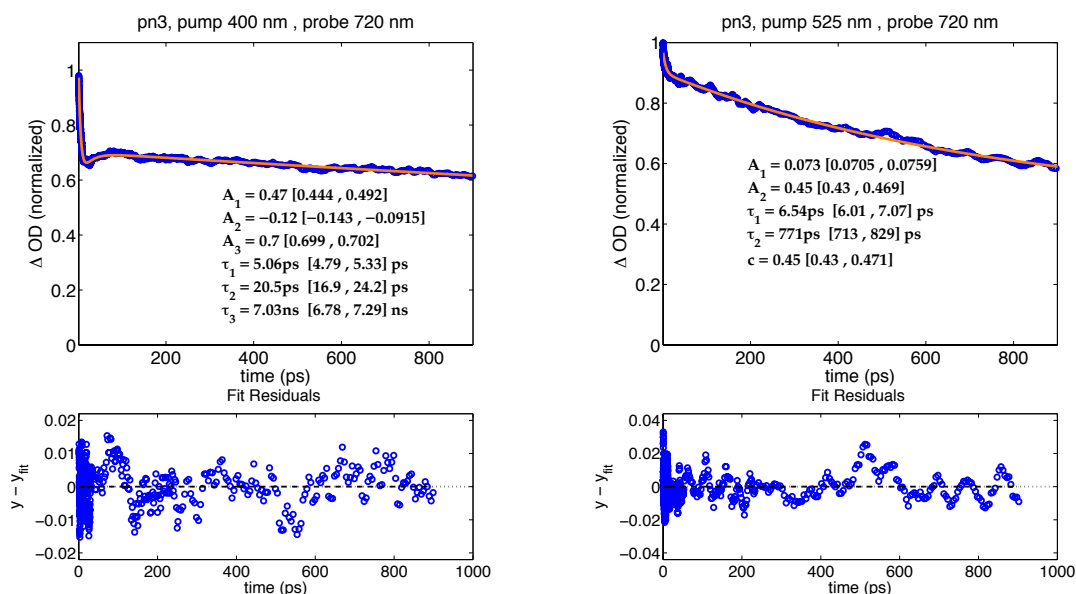


**Figure 5.18:** Transient absorption of PN3 probed at 720 nm after excitation at 400 nm (left) and 525 nm (right).

fit to a rise time of 720 fs and 10 ps, and a decay time of 6.6 ns, as shown in Figure 5.19. The 723 fs is likely due to vibrational relaxation in the HTH excited state. The 10 ps can be attributed to both energy transfer and charge separation from the HTH excited state. Energy transfer forms the PDI excited state and charge separation depletes the PDI ground state, and both give rise to transient absorption signal at 540 nm. To check the consistency of this analysis, we examine the transient absorption signal at 580 nm. The transient absorption signal at 580 nm should primarily contain contributions from the PDI excited state. At early times, the transient absorption signal at 580 nm rises with a timescale of 3 ps. This could be the timescale of energy transfer, since the 5 ps extracted from fitting the time-resolved fluorescence has a large uncertainty because of the large width of the IRF (150 ps).

Some of the data in PN3 is still difficult to explain. The transient absorption signals at 490 nm and 680 nm, shown in Figures 5.21 and 5.22 contain a rise time of 30 ps, and the origin of this process is still unclear. This timescale is not observed when PDI is excited at 525 nm, suggesting that they represent a process that originates from the HTH excited state. It is possible that these signals originate from the naphthalene diimide radical anion, which has an absorption peak at 500 nm and a smaller peak at 680 nm [105].

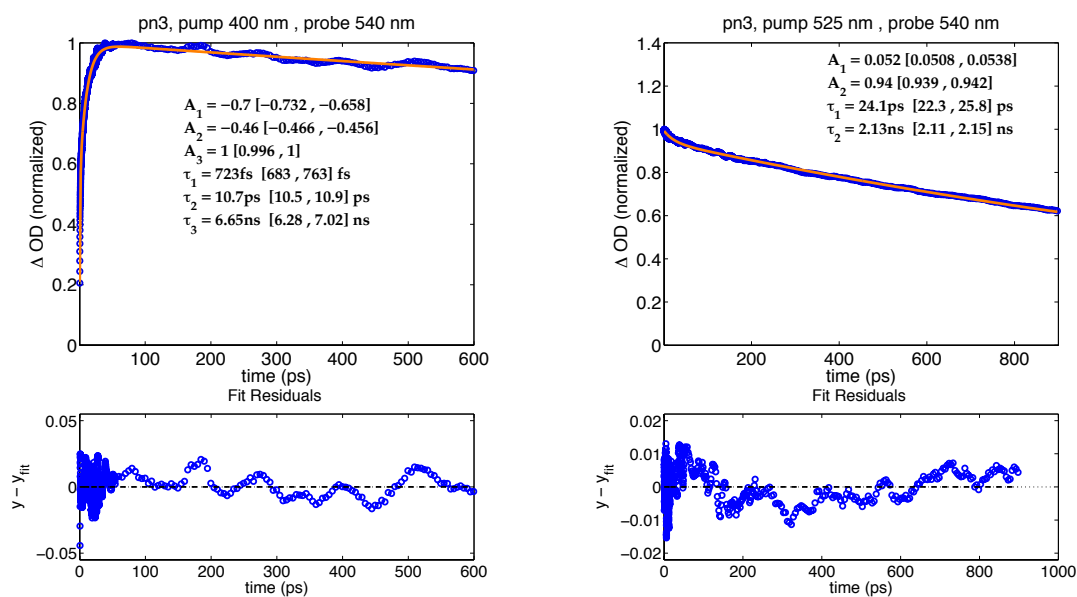


Figure 5.19: Transient absorption of PN3 probed at 540 nm after excitation at 400 nm (left) and 525 nm (right).

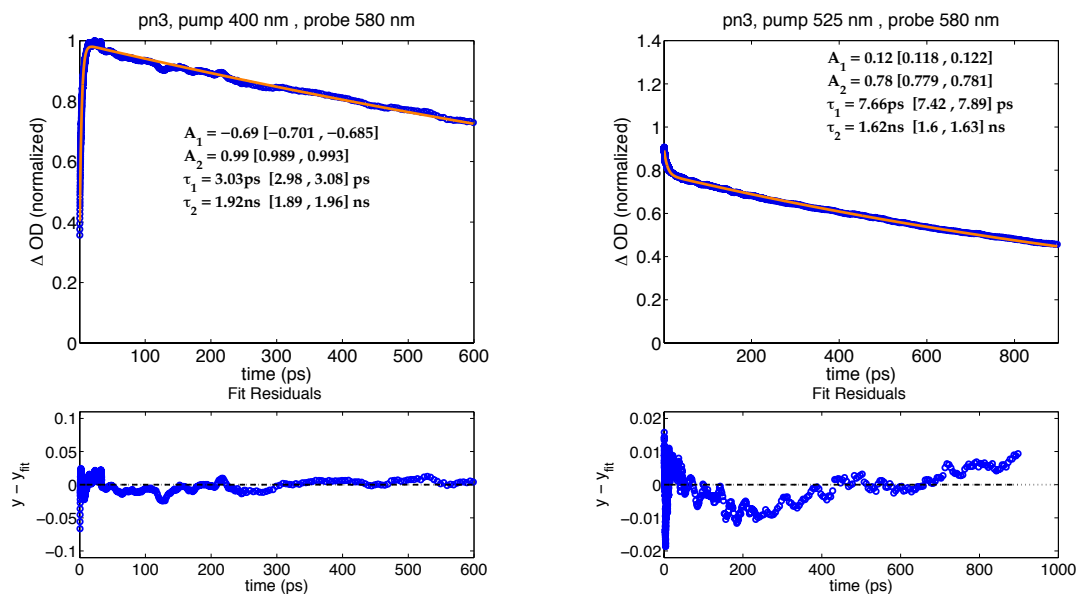


Figure 5.20: Transient absorption of PN3 probed at 580 nm after excitation at 400 nm (left) and 525 nm (right)..

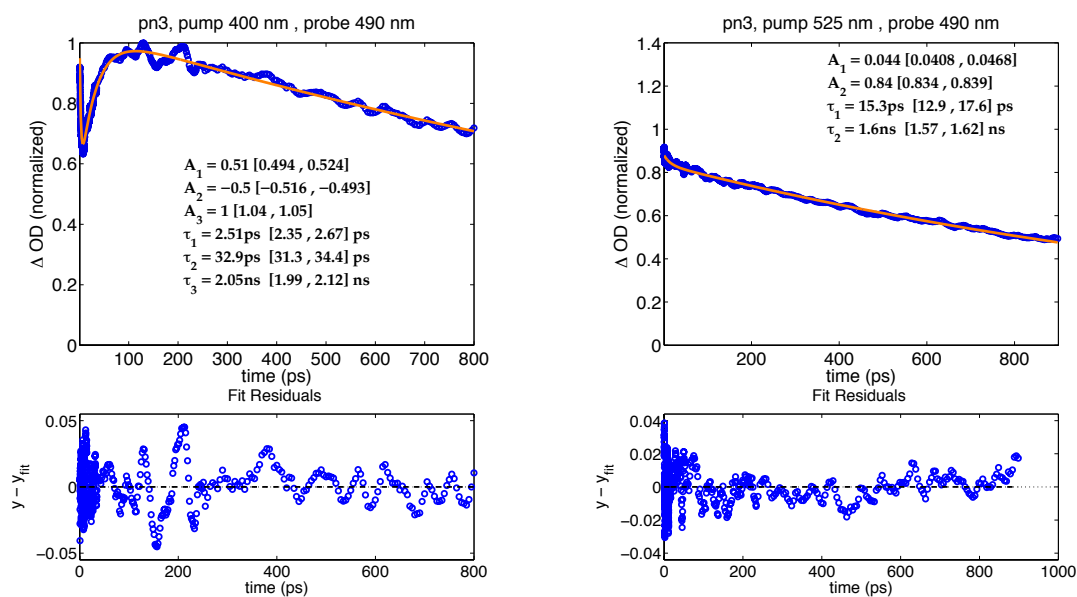


Figure 5.21: Transient absorption of PN3 probed at 490 nm after excitation at 400 nm (left) and 525 nm (right).

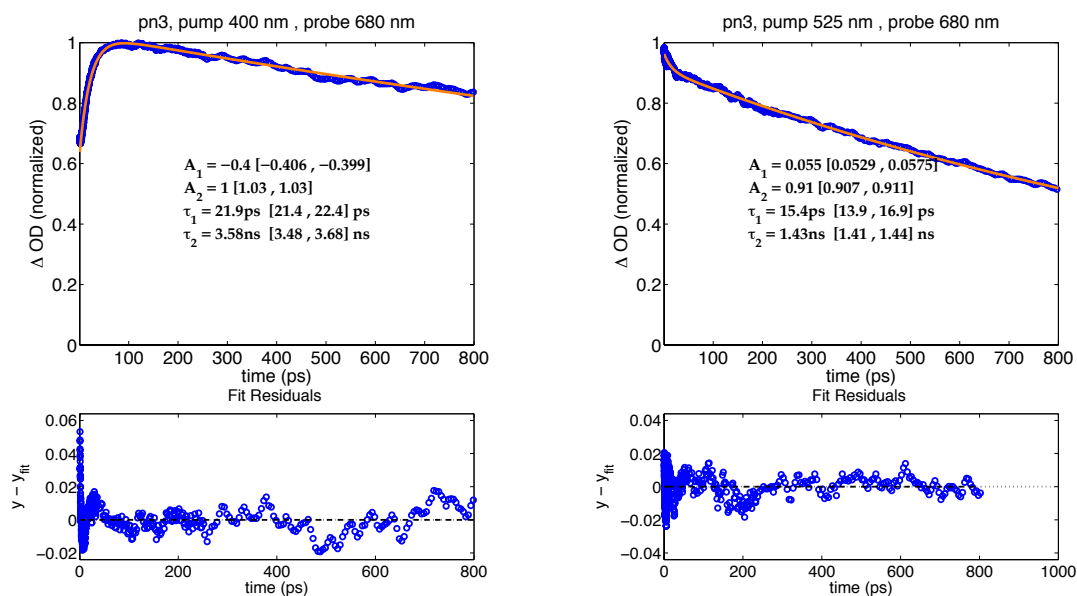
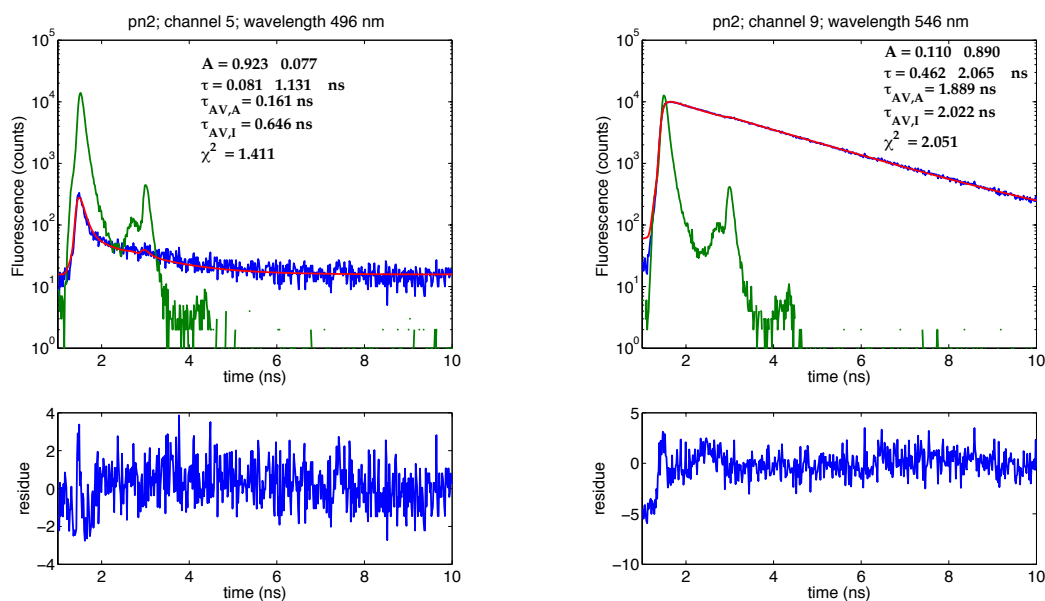


Figure 5.22: Transient absorption of PN3 probed at 680 nm after excitation at 400 nm (left) and 525 nm (right).

## PN2

Figure 5.23 (left panel) shows the fluorescence decay of the excited state of HTH in PN2, which has a flexible, non-conjugated bridge. The HTH excited state decayed on a timescale of 80 ps after excitation of the HTH at 410 nm. This timescale is slower than the timescale of 5 ps in PN3. Assigning this timescale to energy transfer from HTH to PDI is not consistent with transient absorption data in which the rise of the at 540 and 580 nm following excitation at 400 nm occurs in  $\sim 1.5$  ps, which is faster than the rise of this signal in PN3 and suggests that energy transfer from HTH to PDI is faster in PN2 than in PN3. The overall fluorescence yield of PN2 is lower than PN3, and the steady state fluorescence spectrum of PN2 resembles that of PN3.



**Figure 5.23:** Fluorescence from PN2 in toluene detected at 496 nm (left) and 546 nm (right) following excitation at 410 nm.

The transient absorption signal at 490 nm in PN2 (Figure 5.24) shows a rise of 5 ps at early times, followed by a decay of 67 ps, which matches the timescale of the fluorescence decay. It is possible that the vibronic structure of PDI in PN2 is slightly altered so that the PDI has a slightly larger emission cross section at 490 nm than it does in PN3. Because the fluorescence lifetime at all wavelengths was measured simultaneously with one multi-wavelength detector, it is also possible that HTH in PN2 is depleted so quickly that the amount of fluorescing HTH is so small as to not be detected by the TCSPC experiment in the time that it took the number of counts to reach 10,000 in the channel with the maximum number of counts.

The transient absorption signals of PN2 excited at 525 nm all decayed with a timescale of 1-2 ns, suggesting that no additional species were formed following excitation at 525 nm. The average fluorescence lifetime of PN2 at 530 nm and higher was 2 ns, and unlike PN3, two exponentials were needed to fit the fluorescence lifetime of PN2. It is possible that the flexible nature of PN2 enabled the molecule to take on multiple conformations that gave rise

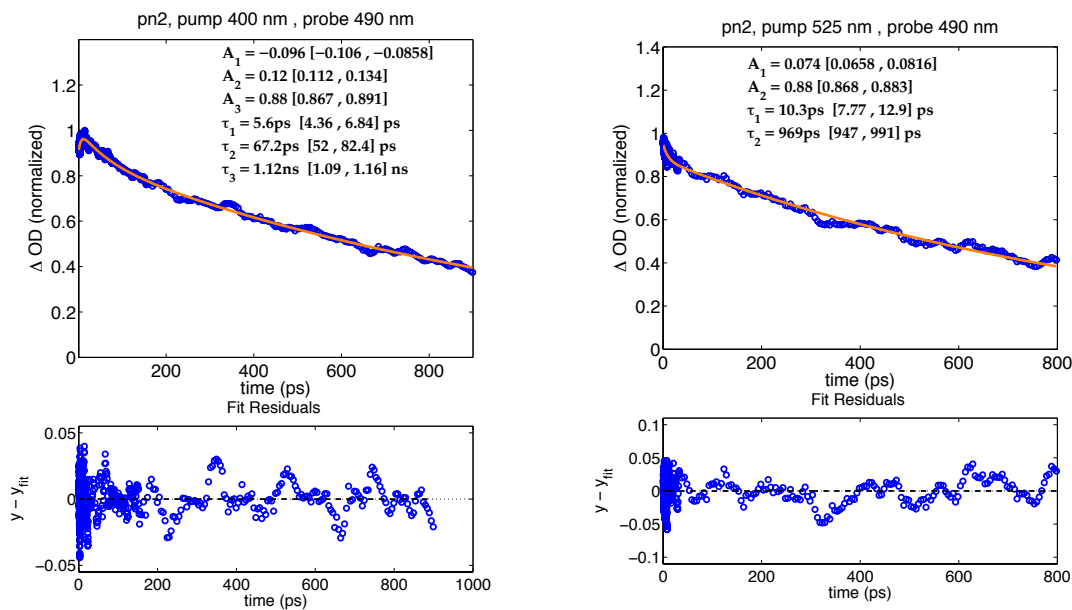


**Figure 5.24:** Transient absorption of PN2 probed at 490 nm after excitation at 400 nm (left) and 525 nm (right).

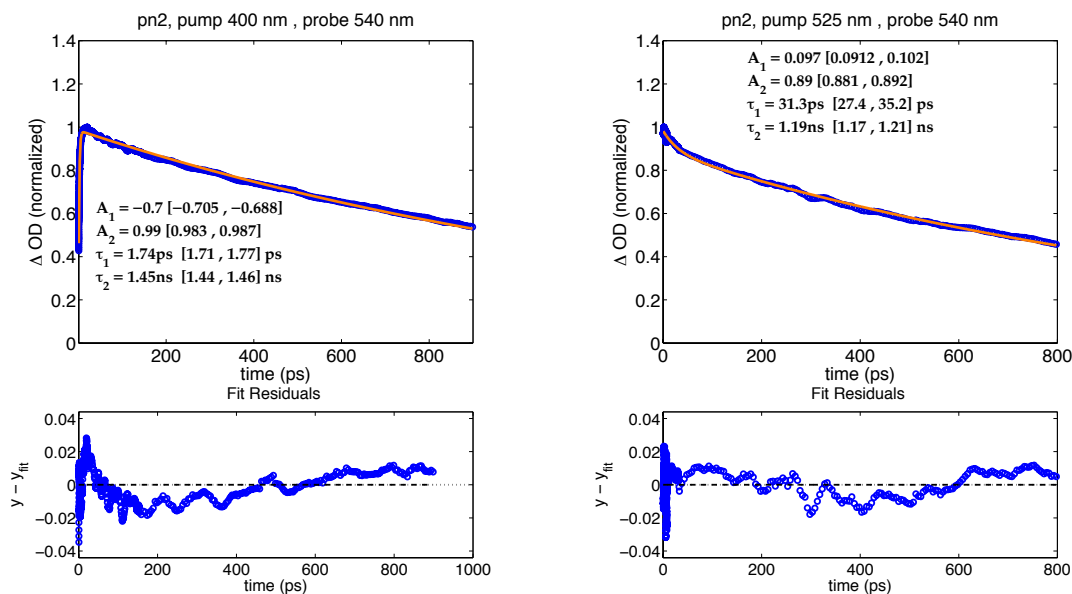


**Figure 5.25:** Transient absorption of PN2 probed at 540 nm after excitation at 400 nm (left) and 525 nm (right).

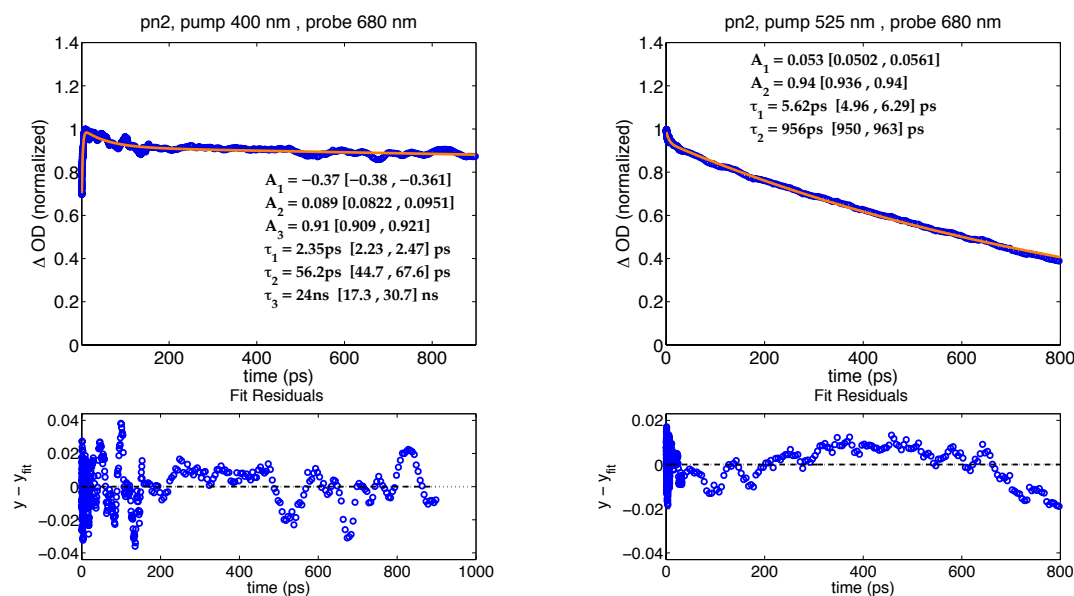


**Figure 5.26:** Transient absorption of PN2 probed at 680 nm following excitation at 400 nm and 525 nm.

to different rates of energy transfer between HTH and PDI. It is also possible that the flexible bridge in PN2 accelerated the rate of internal conversion to the ground state, reducing the fluorescence lifetime of PDI from 3.6 ns to 2 ns.

The transient absorption signals of PN2 at wavelengths between 680 nm and 960 nm exhibited a long plateau, as shown for 680 nm and 720 nm in Figures 5.26 and 5.27. This signal does not appear when PN2 is excited at 525 nm. It is likely that this plateau is a signature of the triplet state of HTH. The triplet absorption of molecule 6T in reference [101] has a peak at 680 and absorption into higher wavelengths. Although the singlet properties of the HTH in our study are more similar to the 5T molecule of reference [101], it is possible that the triplet state properties are more similar to 6T when the HTH is bound with a bridge to the NDI-PDI molecule.

The other alternatives would be a charge separated state: either  $\text{HTH}^+ \text{-PDI}^-$  or  $\text{HTH}^+ \text{-NDI}^-$ . However, both of these are unlikely. The PDI ground state bleach at 540 nm decays in 1.5 ns after excitation at 400 nm suggesting that a charge-separated state does not persist for longer than the timescale of the PDI excited state. The signal at 490 nm, where the NDI anion would absorb [105], also decays within 1.2 ns. Overall, it appears that PDI has a high triplet yield from excited HTH, but there does not appear to be any evidence for photoinduced charge separation in PN2.

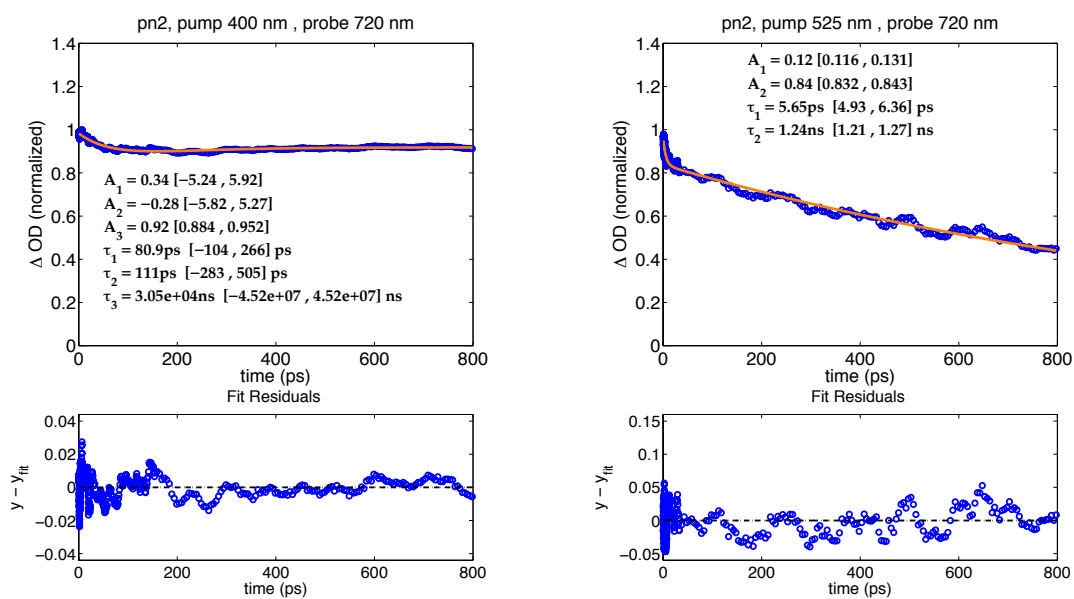


**Figure 5.27:** Transient absorption of PN2 probed at 720 nm following excitation at 400 nm (left) and 525 nm (right).

## PN4

The time-resolved fluorescence of PN4 at 496 nm is similar to that of PN2, with a short lifetime component of 80 ps. At wavelengths where the PDI emits, the fluorescence lifetime of PN4 could be fit to a single exponential with a lifetime of 2.8 ps, which is shorter than the lifetime of PN3 at these wavelengths but longer than the lifetime of PN2. The transient absorption signals of PN4 at all probe wavelengths following excitation at 525 nm decayed with a timescale of 1.6-2.5 ns, suggesting that the excited state of PDI in PN4 decays directly to the ground state.

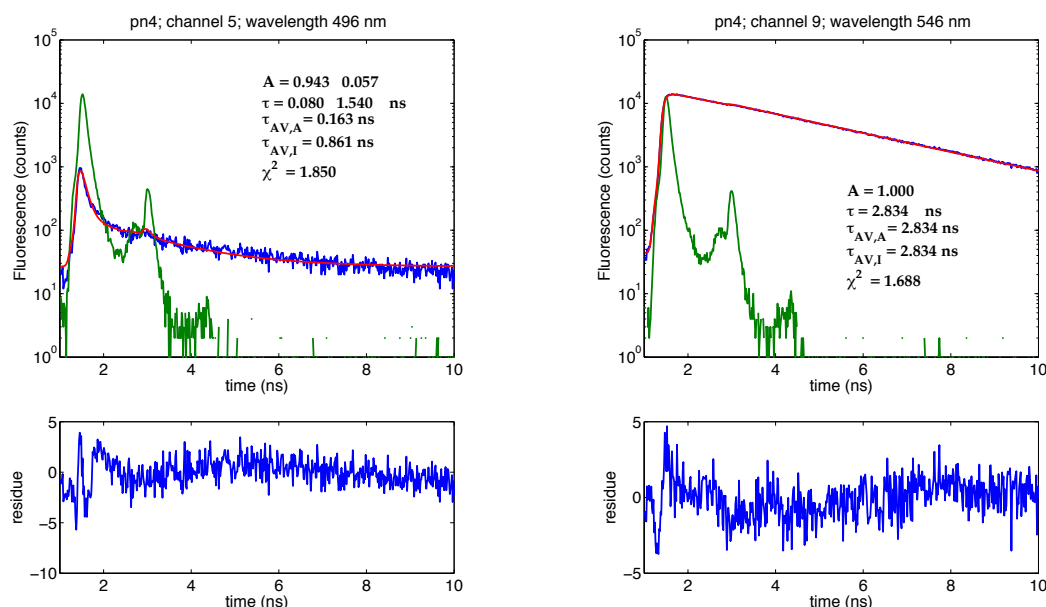


**Figure 5.28:** Fluorescence emitted from PN4 in toluene detected at 496 nm (left) and 546 nm (right) after excitation at 410 nm.

When excited at 400 nm, PN4 exhibits a rise between 680 nm and 820 nm that has a much greater amplitude than PN2, and is consistent with the absorption spectrum of an HTH triplet [101]. Figures 5.29 and 5.30 shows transient absorption of PN4 at 680 nm and 820 nm, and Figures 5.31 and 5.32 show transient absorption signals of PN4 probed at 490 nm and 540 nm, where PDI has a ground state bleach. The transient absorption signals at 490 nm and 540 nm decay with a timescale of 2.7 ns and 3.6 ns, which is slower than the decay of these signals following excitation at 525 nm. Because PDI exhibits a bleach at these wavelengths, it is possible that some  $\text{HTH}^+\text{-PDI}^-$  is formed in PN4 in parallel with the HTH triplet. Quantifying the amount of  $\text{HTH}^+\text{-PDI}^-$  would require fitting to a kinetic scheme such as the one in Figure 5.16.

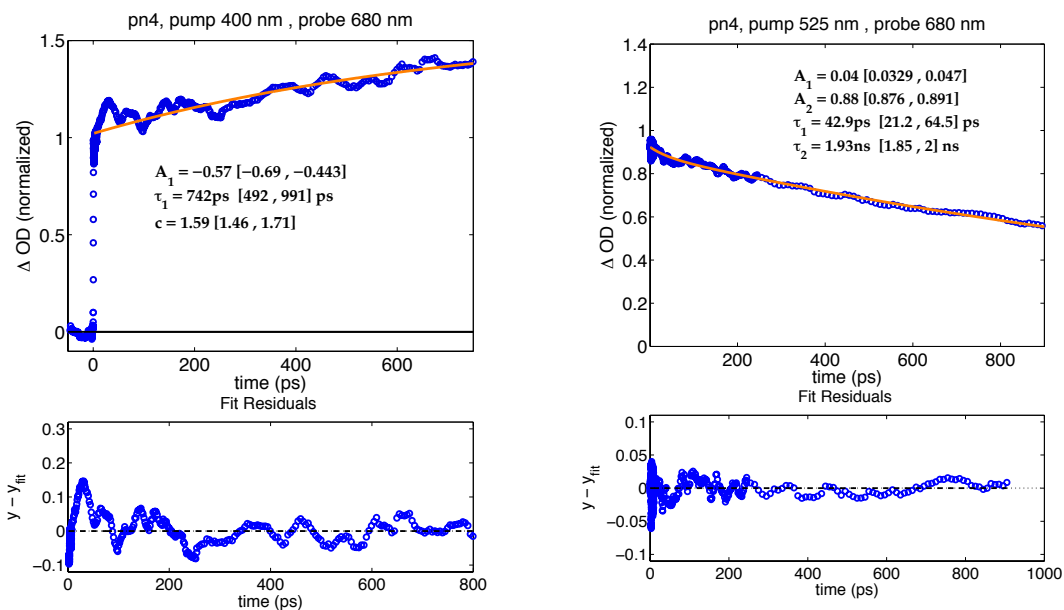


**Figure 5.29:** Transient absorption of PN4 probed at 680 nm following excitation at 400 nm (left) and 525 nm (right).

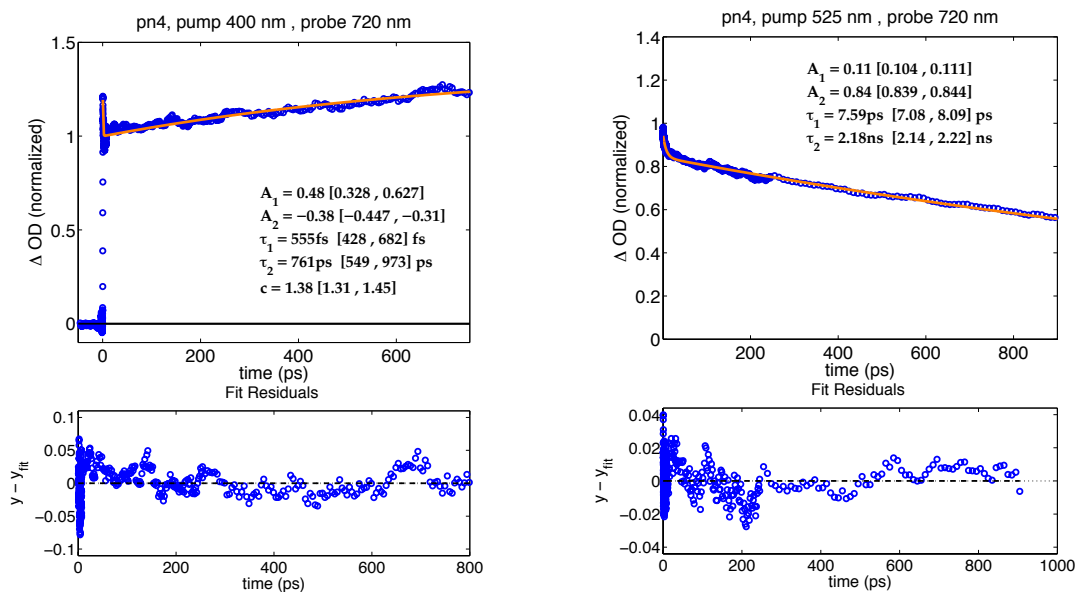


**Figure 5.30:** Transient absorption of PN4 probed at 720 nm following excitation at 400 nm (left) and 525 nm (right).

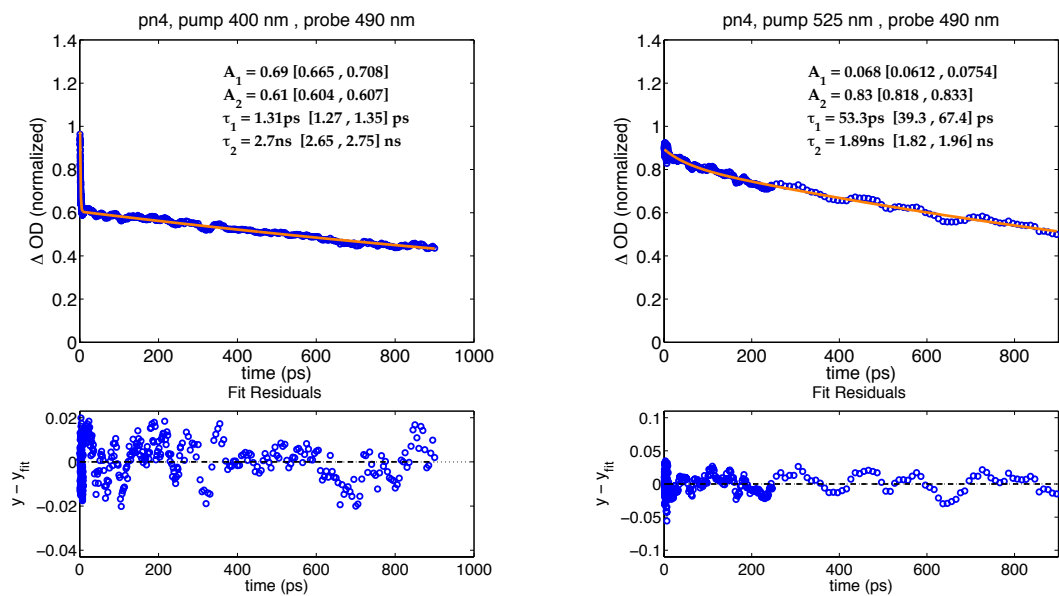


**Figure 5.31:** Transient absorption of PN4 probed at 490 nm following excitation at 400 nm (left) and 525 nm (right).

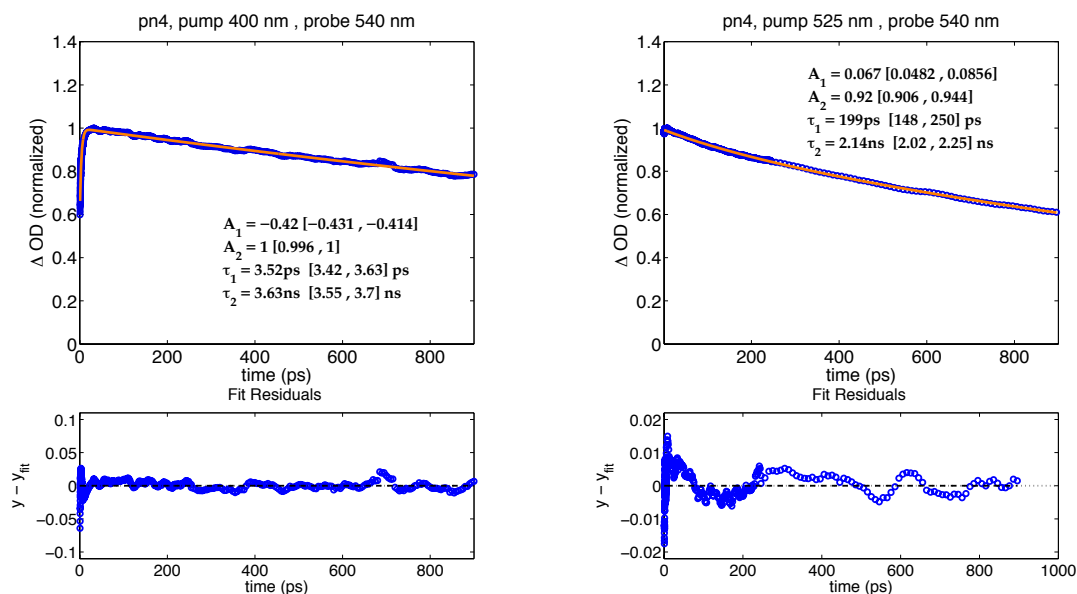


**Figure 5.32:** Transient absorption of PN4 probed at 540 nm following excitation at 400 nm (left) and 525 nm (right).

## 5.4 Effect of bridge properties

### Effect of bridge length

A short bridge appears to be necessary for charge separation to occur. The PDI-HTH systems is attractive because the combined absorption spectrum of the PN molecules covers a larger range of the visible spectrum than HTH alone. However, the work presented in this chapter suggests that the absorption of photons by the PDI does not contribute significantly to any sort of charge-separated state unless the bridge is short, as in PN1. Furthermore, because energy transfer readily occurs from HTH to PDI, the presence of the PDI in PN2, PN3, and PN4 appears to act as an unproductive sink for excitation energy. Previous work on thiopheneperylene molecules that observed a high yield of charge separation had short bridges similar to PN1 [104]; also, molecules with a short, flexible bridge has a higher charge separation rate than a molecule with a longer, flexible bridge [102].

### Effect of bridge rigidity

The quantum yield of charge separation seems to be higher in PN3 than in PN2, which has a flexible bridge. It is likely that the flexible structure of PN2 facilitates vibrations that are able to dissipate the energy in the excited state of HTH. The lower yield of charge separation in PN2 arises from competition from other processes that dissipate the excited state of PDI and HTH, corresponding to rates  $k_7$  and  $k_5$  in scheme 5.16. The flexible structure of PN2 could give rise to a large number of conformers, only some of which are able to do charge separation.

### Effect of bridge conjugation

To isolate the effect of bridge conjugation from bridge length, it is necessary to compare PN4 to PN2 and PN3. Because the ground state bleach of PDI decays more slowly in PN4 than PN2 following excitation of the PDI, it seems that PN4 is more likely to perform charge separation than PN2. However, it seem that PN3 could be more effective than PN4 at separating charge from the HTH excited state because it has a longer lifetime at 540 nm, where PDI absorbs to effectively separate charge, and does not seem to have as high of a HTH triplet signal. Overall, it appears that bridge conjugation is less important than bridge length in facilitating charge separation.

#### 5.4.1 Kinetic scheme

The processes within the PN molecules can be interpreted in the context of the kinetic scheme shown in Figure 5.16. Fitting the data to the scheme did not yield satisfactory fits, but the solution of the rate laws associated with the kinetic scheme is presented here. In this scheme, energy transfer can occur from HTH to PDI, and charge separation can occur from either HTH\* or PDI\*. HTH and PDI can also relax on their own to the triplet state or to the ground

state. This scheme has also been presented in reference [104], and includes the following rates:

1. Rate of energy transfer from HTH to PDI ( $k_1$ ).
2. Rate of charge separation from HTH ( $k_2$ )
3. Rate of charge separation from PDI ( $k_3$ )
4. Rate of charge recombination ( $k_4$ )
5. Rate of competing processes (intersystem crossing, internal conversion, fluorescence) from excited HTH ( $k_5$  and  $k_7$ )
6. Rate of competing processes from excited PDI ( $k_6$  and  $k_8$ )

Transient absorption and time-resolved fluorescence experiments probe the population of one or more of the states involved as a function of time following excitation. To extract the rates from experimental measurements, it is necessary to find the kinetic rate law that predicts the populations of measurable states.

The differential equations describing the evolution of the six states involved in the model of Figure 5.16 are

$$\frac{d}{dt} \begin{pmatrix} X_1 \\ X_2 \\ X_3 \\ X_4 \\ X_5 \\ X_6 \end{pmatrix} = \begin{pmatrix} -k_1 - k_2 - k_5 - k_7 & 0 & 0 \\ k_1 & -k_3 - k_6 - k_8 & 0 \\ k_2 & k_3 & -k_4 \\ k_7 & 0 & 0 \\ 0 & k_8 & 0 \\ k_5 & k_6 & k_4 \end{pmatrix} \begin{pmatrix} X_1 \\ X_2 \\ X_3 \end{pmatrix}. \quad (5.1)$$

The rate matrix in this expression has rank 3 because the evolution of all populations is determined by only the three states:  $X_1$ ,  $X_2$ , and  $X_3$ . This is because once the sample is in state  $X_4$ ,  $X_5$ , or  $X_6$ , it does not leave that state. The rate matrix has three eigenvalues:  $\lambda_1 = -k_1 - k_2 - k_5 - k_7$ ,  $\lambda_2 = -k_3 - k_6 - k_8$ ,  $\lambda_3 = -k_4$ . It is also convenient to define the following quantities:

$$\begin{aligned}
A_0 &= X_1(0) \\
A_1 &= \frac{k_1 A_0}{\lambda_1 - \lambda_2} \\
A_2 &= X_2(0) - A_1 \\
A_3 &= \frac{k_2 A_0 + k_3 A_1}{\lambda_1 - \lambda_3} \\
A_4 &= \frac{k_3 A_2}{\lambda_2 - \lambda_3} \\
A_5 &= \frac{k_5 A_0 + k_6 A_1 + k_4 A_3}{\lambda_1} \\
A_6 &= \frac{k_6 A_2 + k_4 A_4}{\lambda_2} \\
A_7 &= -\frac{k_4 (A_3 + A_4)}{\lambda_3} \\
A_8 &= \frac{k_7 A_0}{\lambda_1} \\
A_9 &= \frac{k_8 A_1}{\lambda_1} \\
A_{10} &= \frac{k_8 A_2}{\lambda_2}
\end{aligned}$$

Integrating equation 5.1 gives the following results:

$$\begin{aligned}
X_1(t) &= A_0 e^{\lambda_1 t} \\
X_2(t) &= A_1 e^{\lambda_1 t} + A_2 e^{\lambda_2 t} \\
X_3(t) &= A_3 e^{\lambda_1 t} + A_4 e^{\lambda_2 t} - (A_3 + A_4) e^{\lambda_3 t} \\
X_4(t) &= A_8 (e^{\lambda_1 t} - 1) \\
X_5(t) &= A_9 (e^{\lambda_1 t} - 1) + A_{10} (e^{\lambda_2 t} - 1) \\
X_6(t) &= A_5 (e^{\lambda_1 t} - 1) + A_6 (e^{\lambda_2 t} - 1) + A_7 (e^{\lambda_3 t} - 1)
\end{aligned} \tag{5.2}$$

The experimentally measurable signal related to  $X_6$  is a bleach of the ground state of PDI, which appears at 540 nm, so when the system is in state  $X_1$  or state  $X_4$ , the bleach will not be detected because the absorption spectrum of HTH is not in the detection range of the probe. As a result,  $X_6$  in the scheme above was not used in the fitting. Instead, the state  $X_6^*$  was used to fit to the ground state of PDI:

$$X_6^*(t) = X_2 + X_3 + X_4$$

When the HTH is excited at 400 nm, the initial condition is that  $X_1(0) = 1$  and  $X_2(0) = 0$ . When the the sample is excited at 525 nm, the initial condition is that  $X_1(0) = 0$  and

$X_2(0) = 1$ . In this latter case,  $A_0 = 0$ , which means that  $A_1 = 0$ ,  $A_3 = 0$ ,  $A_5 = 0$ ,  $A_8 = 0$  and  $A_9 = 0$ .  $A_7$  reduces to equal  $A_4$ . This yields the following simplified scheme for the situation where the sample is excited at 525 nm:

$$\begin{aligned}
 X_1(t) &= 0 \\
 X_2(t) &= A_2 e^{\lambda_2 t} \\
 X_3(t) &= A_4 (e^{\lambda_2 t} - e^{\lambda_3 t}) \\
 X_4(t) &= 0 \\
 X_5(t) &= A_{10} (1 - e^{\lambda_2 t}) \\
 X_6(t) &= A_6 (1 - e^{\lambda_2 t}) + A_4 (1 - e^{\lambda_3 t})
 \end{aligned} \tag{5.3}$$

I attempted to fit the available transient absorption and time-resolved fluorescence measurements were fit simultaneously to equations 5.2 and 5.3 simultaneously with fitting the time-resolved fluorescence measurements. It was not possible to obtain satisfactory fits to the scheme in Figure 5.16, suggesting that the scheme must be expanded to encompass the processes in PN1-4.

In this fitting attempt, the fit parameters were the rates  $k_1$ - $k_8$ , the amplitudes of the contribution of each state  $X_1$ - $X_6$  to the transient absorption signal, and the amplitudes of the contributions of the emissive states  $X_1$  and  $X_2$  to the fluorescence signal. The fluorescence data was fit by calculating the convolution with the model with the IRF. The transient absorption data was fit direction because the pulse width was too short to significantly affect the fitting at timescales greater than 1 ps. Each transient absorption trace of the sample excited at 525 nm was allowed to contained contributions from states  $X_2$ ,  $X_3$ ,  $X_5$  and  $X_6$ , and the each trace of the sample excited at 400 nm was allowed to contain contributions for all six states. The signal at each wavelength was allowed to have some contributions from each state, but the amplitudes were constrained to be consisted with the spectra published in the literature [100, 104, 103].

The conclusions of a global analysis would be strengthened by the availability of full absorption spectra for all molecules with both 525 nm and 400 nm excitation for all PN molecules and also for the HTH donor and the PDI-NDI acceptor. Because the existing data has only been collected at a limited number of probe wavelengths, we cannot assign specific spectra to the states  $X_1$  through  $X_6$  in Figure 5.16. There is software [106] that enables global analysis of transient absorption spectra.

## 5.5 Conclusion

Time resolved fluorescence and transient absorption spectroscopy has been conducted on donor-bridge-acceptor molecules consisting of a hexathiophene (HTH) oligomer as electron donor and a perylene bisimide (PDI)-naphthalene bisimide (NDI) dimer as electron acceptor. In PN1, which has a short, conjugated bridge, charge separation proceeded from excited states of both donor and acceptor; in PN2 and PN3, which have longer bridges of varying flexibility and conjugation, charge separation only proceeded from the HTH donor. Recombination of

the charge separated state occurs more rapidly in molecules with a short, conjugated bridge than in the other molecules with longer, flexible bridges, making the extraction of charges more difficult. Overall, a rigid bridge appears to be preferable to a flexible bridge for reducing the rate of charge recombination, and a short bridge appears to be necessary for charge separation to occur from both donor and acceptor.

Generalizing these observations to donor- $\pi$ -acceptors in dye-sensitized solar cells, it appears that short, conjugated bridges between donor and acceptor are needed for efficient charge separation to proceed from both donor and acceptor, and that it would be necessary to rapidly extract charge before the charge-separated state recombines.

In addition to designing molecules that are able to efficiently separate charge, it will be important to develop energy transfer systems that absorb light in a broad range of the solar spectrum [107, 108], in a similar manner to light harvesting by antenna proteins in photosynthesis [109]. In such systems, it is desirable for energy to be transferred between chromophores without undergoing charge separation. Covalently bonding antenna dyes to the charge-separation system would enable greater control of location and orientation of these antennas. The work presented here suggest that the rigid, non-conjugated bridge in PN3 would serve as a more effective tether of an energy relay dye to a charge-separation site than a flexible bridge or a conjugated bridge.

## 5.6 Fits of fluorescence lifetime data

This section contains fits of fluorescence lifetime of HTH.

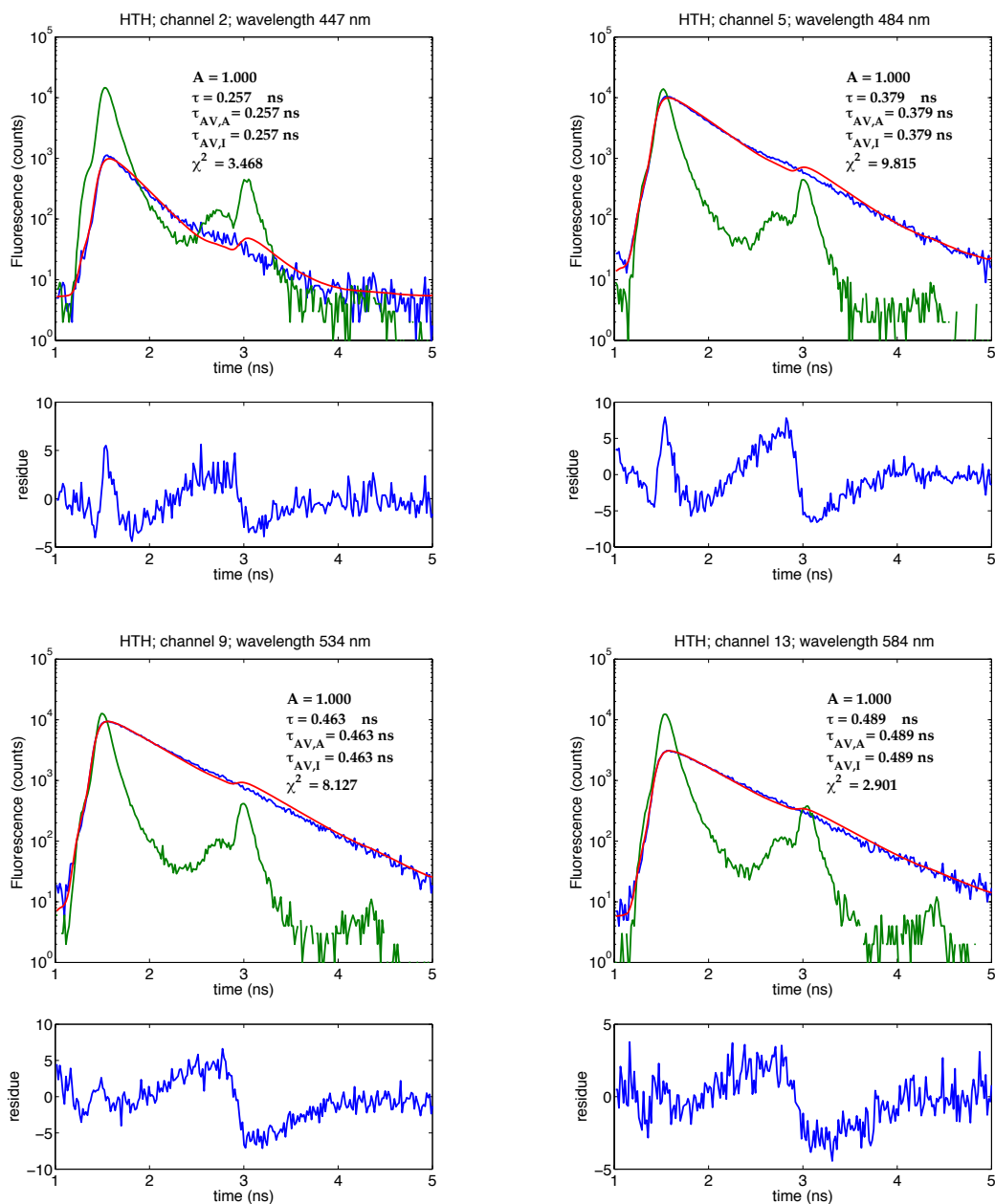


**Figure 5.33:** Fluorescence lifetime of Hexathiophene (HTH) in toluene excited at 400 nm. Detection wavelengths are 447 nm, 471 nm, 534 nm, 584 nm

# Chapter 6

## Reference Tables

**Table 6.1:** Abbreviations

NPQ	nonphotochemical quenching
qE	energy-dependent nonphotochemical quenching
RC	reaction center
PAM	pulse amplitude modulation
Chl	chlorophyll
NPQSM	NPQ Systems Model
GUI	graphical user interface
HTH	hexathiophene
PDI	perylene diimide
NDI	naphthalene diimide
PN1, PN2, PN3, PN4	names of molecules studied in Chapter 5

**Table 6.2:** qE mutants of *Arabidopsis thaliana*

mutant	description
<i>npq4</i>	missing gene for PsbS protein [20]
L17	elevated levels of PsbS protein [13]
<i>npq1</i>	missing gene for violaxanthin deepoxidase [22]
<i>lut2</i>	missing gene lycopene $\epsilon$ -cyclase [70]
<i>npq1lut2</i>	missing lycopene $\epsilon$ -cyclase and violaxanthin deepoxidase [79]

# Bibliography

- [1] Zhu, X.-G., Long, S. P. & Ort, D. R. Improving Photosynthetic Efficiency for Greater Yield. *Annual Review of Plant Biology* **61**, 235–261 (2010).
- [2] Blankenship, R. E. *Molecular mechanisms of photosynthesis* (Blackwell Science, 2002).
- [3] Hardin, B. E., Snaith, H. J. & McGehee, M. D. The renaissance of dye-sensitized solar cells. *Nature Photonics* **6**, 162–169 (2012).
- [4] Melis, A. Photosystem-II damage and repair cycle in chloroplasts: what modulates the rate of photodamage in vivo? *Trends In Plant Science* **4**, 130–135 (1999).
- [5] Adir, N., Zer, H., Shochat, S. & Ohad, I. Photoinhibition - a historical perspective. *Photosynthesis Research* **76**, 343–370 (2003).
- [6] Murata, N., Takahashi, S., NISHIYAMA, Y. & Allakhverdiev, S. I. Photoinhibition of photosystem II under environmental stress. *Biochimica et Biophysica Acta (BBA) - Bioenergetics* **1767**, 414–421 (2007).
- [7] Vass, I. Role of charge recombination processes in photodamage and photoprotection of the photosystem II complex. *Physiologia Plantarum* **142**, 6–16 (2011).
- [8] Takahashi, S. & Badger, M. R. Photoprotection in plants: a new light on photosystem II damage. *Trends In Plant Science* **16**, 53–60 (2011).
- [9] Asghar, M. I. *et al.* Review of stability for advanced dye solar cells. *Energy & Environmental Science* **3**, 418 (2010).
- [10] Peters, C. H. *et al.* The Mechanism of Burn-in Loss in a High Efficiency Polymer Solar Cell. *Advanced Materials* **24**, 663–668 (2011).
- [11] Hoke, E. T. *et al.* The Role of Electron Affinity in Determining Whether Fullerenes Catalyze or Inhibit Photooxidation of Polymers for Solar Cells. *Advanced Energy Materials* **2**, 1351–1357 (2012).
- [12] Kulheim, C., Agren, J. & Jansson, S. Rapid Regulation of Light Harvesting and Plant Fitness in the Field. *Science* **297**, 91–93 (2002).

- [13] Li, X.-P., Muller-Moule, P., Gilmore, A. M. & Niyogi, K. K. PsbS-dependent enhancement of feedback de-excitation protects photosystem II from photoinhibition. *Proceedings Of The National Academy Of Sciences Of The United States Of America* **99**, 15222–15227 (2002).
- [14] Müller, P., Li, X.-P. & Niyogi, K. K. Non-photochemical quenching. A response to excess light energy. *Plant Physiology* **125**, 1558–1566 (2001).
- [15] Li, Z., Wakao, S., Fischer, B. B. & Niyogi, K. K. Sensing and Responding to Excess Light. *Annual Review Of Plant Biology, Vol 61* **60**, 239–260 (2009).
- [16] de Bianchi, S., Ballottari, M., Dall’Osto, L. & Bassi, R. Regulation of plant light harvesting by thermal dissipation of excess energy. *Biochemical Society Transactions* **38**, 651–660 (2010).
- [17] Logan, B. A., Terry, S. G. & Niyogi, K. K. Arabidopsis genotypes with differing levels of PsbS expression differ in photosystem II quantum yield, xanthophyll cycle pool size, and aboveground growth. *International Journal of Plant Sciences* **169**, 597–604 (2008).
- [18] Terazono, Y. *et al.* Mimicking the Role of the Antenna in Photosynthetic Photoprotection. *Journal Of The American Chemical Society* **133**, 2916–2922 (2011).
- [19] Ruban, A. V., Johnson, M. P. & Duffy, C. D. P. The photoprotective molecular switch in the photosystem II antenna. *Biochimica Et Biophysica Acta-Bioenergetics* **1817**, 167–181 (2012).
- [20] Li, X.-P. *et al.* A pigment-binding protein essential for regulation of photosynthetic light harvesting. *Nature* **403**, 391–395 (2000).
- [21] Demmig-Adams, B. Carotenoids and photoprotection in plants: a role for the xanthophyll zeaxanthin. *Biochimica Et Biophysica Acta* **1020**, 1–24 (1990).
- [22] Niyogi, K. K., Grossman, A. R. & Björkman, O. Arabidopsis mutants define a central role for the xanthophyll cycle in the regulation of photosynthetic energy conversion. *The Plant Cell* **10**, 1121–1134 (1998).
- [23] Walters, R., Ruban, A. V. & Horton, P. Identification of proton-active residues in a higher plant light-harvesting complex. *Proceedings Of The National Academy Of Sciences Of The United States Of America* **93**, 14204–14209 (1996).
- [24] Bassi, R. & Caffarri, S. Lhc proteins and the regulation of photosynthetic light harvesting function by xanthophylls. *Photosynthesis Research* **64**, 243–256 (2000).
- [25] Jahns, P., Latowski, D. & Strzalka, K. Mechanism and regulation of the violaxanthin cycle: The role of antenna proteins and membrane lipid. *Biochimica et Biophysica Acta (BBA) - Bioenergetics* **1787**, 3–14 (2009).

- [26] Johnson, M. P. *et al.* Photoprotective Energy Dissipation Involves the Reorganization of Photosystem II Light-Harvesting Complexes in the Grana Membranes of Spinach Chloroplasts. *The Plant Cell* **23**, 1468–1479 (2011).
- [27] Betterle, N., Ballottari, M., Bassi, R. & 8. Light-induced dissociation of an antenna hetero-oligomer is needed for non-photochemical quenching induction. *The Journal of biological chemistry* **284**, 15255–15266 (2009).
- [28] Ruban, A. V. *et al.* Identification of a mechanism of photoprotective energy dissipation in higher plants. *Nature* **450**, 575–578 (2007).
- [29] Ahn, T. K. *et al.* Architecture of a charge-transfer state regulating light harvesting in a plant antenna protein. *Science* **320**, 794–797 (2008).
- [30] Holzwarth, A. R., Miloslavina, Y., Nilkens, M. & Jahns, P. Identification of two quenching sites active in the regulation of photosynthetic light-harvesting studied by time-resolved fluorescence. *Chemical Physics Letters* **483**, 262–267 (2009).
- [31] Baker, N. Chlorophyll fluorescence: a probe of photosynthesis in vivo. *Annual Review Of Plant Biology, Vol 61* 89–113 (2008).
- [32] Avenson, T. J. *et al.* Integrating the proton circuit into photosynthesis: progress and challenges. *Plant Cell and Environment* **28**, 97–109 (2005).
- [33] Graßes, T. *et al.* The role of pH-dependent dissipation of excitation energy in protecting photosystem II against light-induced damage in *Arabidopsis thaliana*. *Plant Physiology and Biochemistry* **40**, 41–49 (2002).
- [34] Zhu, X. G. The slow reversibility of photosystem II thermal energy dissipation on transfer from high to low light may cause large losses in carbon gain by crop canopies: a theoretical analysis. *Journal of Experimental Botany* **55**, 1167–1175 (2004).
- [35] Murchie, E. H. & Niyogi, K. K. Manipulation of Photoprotection to Improve Plant Photosynthesis. *Plant Physiology* **155**, 86–92 (2011).
- [36] Blankenship, R. E. *et al.* Comparing Photosynthetic and Photovoltaic Efficiencies and Recognizing the Potential for Improvement. *Science* **332**, 805–809 (2011).
- [37] Van Kooten, O., Snel, J. & Vredenberg, W. J. Photosynthetic free energy transduction related to the electric potential changes across the thylakoid membrane. *Photosynthesis Research* **9**, 211–227 (1986).
- [38] Belyaeva, N. E. *et al.* PS II model-based simulations of single turnover flash-induced transients of fluorescence yield monitored within the time domain of 100 ns–10 s on dark-adapted *Chlorella pyrenoidosa* cells. *Photosynthesis Research* **98**, 105–119 (2008).

- [39] Zhu, X.-G. *et al.* Chlorophyll a fluorescence induction kinetics in leaves predicted from a model describing each discrete step of excitation energy and electron transfer associated with Photosystem II. *Planta* **223**, 114–133 (2005).
- [40] Cruz, J. A., Sacksteder, C. A., Kanazawa, A. & Kramer, D. M. Contribution of electric field ( $\Delta\psi$ ) to steady-state transthylakoid proton motive force (pmf) in vitro and in vivo. control of pmf parsing into  $\Delta\psi$  and  $\Delta\text{pH}$  by ionic strength. *Biochemistry* **40**, 1226–1237 (2001).
- [41] Kuvykin, I., Vershubskii, A., Priklonskii, V. & Tikhonov, A. Computer simulation study of pH-dependent regulation of electron transport in chloroplasts. *Biophysics* **54**, 455–464 (2009).
- [42] Ebenhöf, O., Houwaart, T., Lokstein, H., Schlede, S. & Tirok, K. A minimal mathematical model of nonphotochemical quenching of chlorophyll fluorescence. *Biosystems* **103**, 196–204 (2011).
- [43] Rubin, A. & Rizhichenko, G. Modeling of the Primary Processes in a Photosynthetic Membrane. In *Photosynthesis In Silico*, 151–176 (Springer, 2009).
- [44] Lebedeva, N., Riznichenko, G. Y., Belyaeva, N. E., Demin, O. & Rubin, A. B. Kinetic Model of Primary Photosynthetic Processes. *Biofizika* 968–980 (2002).
- [45] Takizawa, K., Cruz, J. A., Kanazawa, A. & Kramer, D. M. The thylakoid proton motive force in vivo. Quantitative, non-invasive probes, energetics, and regulatory consequences of light-induced pmf. *Biochimica Et Biophysica Acta* **1767**, 1233–1244 (2007).
- [46] Sacksteder, C. A., Kanazawa, A., Jacoby, M. E. & Kramer, D. M. The proton to electron stoichiometry of steady-state photosynthesis in living plants: A proton-pumping Q cycle is continuously engaged. *Proceedings of the National Academy of Sciences* **97**, 14283–14288 (2000).
- [47] Raszewski, G. & Renger, T. Light harvesting in photosystem II core complexes is limited by the transfer to the trap: Can the core complex turn into a photoprotective mode? *Journal Of The American Chemical Society* **130**, 4431–4446 (2008).
- [48] Johnson, M. P., Perez-Bueno, M. L., Zia, A., Horton, P. & Ruban, A. V. The Zeaxanthin-Independent and Zeaxanthin-Dependent qE Components of Nonphotochemical Quenching Involve Common Conformational Changes within the Photosystem II Antenna in Arabidopsis. *Plant Physiology* **149**, 1061–1075 (2009).
- [49] Gilmore, A. M. & Yamamoto, H. Linear models relating xanthophylls and lumen acidity to non-photochemical fluorescence quenching. Evidence that antheraxanthin explains zeaxanthin-independent quenching. *Photosynthesis Research* **35**, 67–78 (1993).

- [50] Zhang, R., Kramer, D. M., Cruz, J. A., Struck, K. R. & Sharkey, T. D. The effects of moderately high temperature on zeaxanthin accumulation and decay. *Photosynthesis Research* **108**, 171–181 (2011).
- [51] Niyogi, K. K. Is PsbS the site of non-photochemical quenching in photosynthesis? *Journal of Experimental Botany* **56**, 375–382 (2004).
- [52] Buchanan, B. B. Role of Light in the Regulation of Chloroplast Enzymes. *Ann. Rev. Plant Physiol.* **31**, 341–374 (1980).
- [53] Kramer, D. M., Johnson, G., Kiirats, O. & Edwards, G. New fluorescence parameters for the determination of Q A redox state and excitation energy fluxes. *Photosynthesis Research* **79**, 209–218 (2004).
- [54] van Oort, B. *et al.* Effect of Antenna-Depletion in Photosystem II on Excitation Energy Transfer in *Arabidopsis thaliana*. *Biophysical Journal* **98**, 922–931 (2010).
- [55] Renger, T. & Schlodder, E. Primary Photophysical Processes in Photosystem II: Bridging the Gap between Crystal Structure and Optical Spectra. *ChemPhysChem* **11**, 1141–1153 (2010).
- [56] Scheibe, R. Strategies to maintain redox homeostasis during photosynthesis under changing conditions. *Journal of Experimental Botany* **56**, 1481–1489 (2005).
- [57] Junge, W. & McLaughlin, S. The Role of Fixed and Mobile Buffers in the Kinetics of Proton Movement. *Biochimica Et Biophysica Acta* **890**, 1–5 (1987).
- [58] Kramer, D., Sacksteder, C. & Cruz, J. How acidic is the lumen? *Photosynthesis Research* **60**, 151–163 (1999).
- [59] Kanazawa, A. & Kramer, D. M. In vivo modulation of nonphotochemical exciton quenching (NPQ) by regulation of the chloroplast ATP synthase. *Proceedings Of The National Academy Of Sciences Of The United States Of America* **99**, 12789–12794 (2002).
- [60] Kalituho, L., Beran, K. C. & Jahns, P. The transiently generated nonphotochemical quenching of excitation energy in *Arabidopsis* leaves is modulated by zeaxanthin. *Plant Physiology* **143**, 1861–1870 (2007).
- [61] Bravo, L. A. *et al.* Effect of cold acclimation on the photosynthetic performance of two ecotypes of *Colobanthus quitensis* (Kunth) Bartl. *Journal of Experimental Botany* **58**, 3581–3590 (2007).
- [62] Munekage, Y. *et al.* Cyclic electron flow around photosystem I is essential for photosynthesis. *Nature* **429**, 579–582 (2004).

- [63] Livingston, A. K., Kanazawa, A., Cruz, J. A. & Kramer, D. M. Regulation of cyclic electron flow in C3 plants: differential effects of limiting photosynthesis at ribulose-1,5-bisphosphate carboxylase/oxygenase and glyceraldehyde-3-phosphate dehydrogenase. *Plant Cell and Environment* **33**, 1779–1788 (2010).
- [64] Kramer, D. M. & Avenson, T. J. Dynamic flexibility in the light reactions of photosynthesis governed by both electron and proton transfer reactions. *Trends In Plant Science* **9**, 349–357 (2004).
- [65] Ahn, T. K. *et al.* Investigating energy partitioning during photosynthesis using an expanded quantum yield convention. *Chemical Physics* **357**, 151–158 (2009).
- [66] Brooks, M. D. & Niyogi, K. K. Use of a Pulse-Amplitude Modulated Chlorophyll Fluorometer to Study the Efficiency of Photosynthesis in Arabidopsis Plants. In Jarvis, R. P. (ed.) *Methods in Molecular Biology*, 299–310 (Humana Press, Totowa, NJ, 2011).
- [67] Field, T. S., Nedbal, L. & Ort, D. R. Nonphotochemical Reduction of the Plastoquinone Pool in Sunflower Leaves Originates from Chlororespiration. *Plant Physiology* **116**, 1209–1218 (1998).
- [68] Rochaix, J.-D. J. Regulation of photosynthetic electron transport. *Biochimica Et Biophysica Acta* **1807**, 375–383 (2011).
- [69] Nilkens, M. *et al.* Identification of a slowly inducible zeaxanthin-dependent component of non-photochemical quenching of chlorophyll fluorescence generated under steady-state conditions in Arabidopsis. *Biochimica Et Biophysica Acta-Bioenergetics* **1797**, 466–475 (2010).
- [70] Pogson, B. J., Niyogi, K. K., Bjorkman, O. & DellaPenna, D. Altered xanthophyll compositions adversely affect chlorophyll accumulation and nonphotochemical quenching in Arabidopsis mutants. *Proceedings Of The National Academy Of Sciences Of The United States Of America* **95**, 13324–13329 (1998).
- [71] Shampine, L. & Reichelt, M. The MATLAB ODE suite. *SIAM Journal On Scientific Computing* **18**, 1–22 (1997).
- [72] Broess, K. *et al.* Excitation Energy Transfer and Charge Separation in Photosystem II Membranes Revisited. *Biophysical Journal* **91**, 3776–3786 (2006).
- [73] Johnson, M. P. & Ruban, A. V. Restoration of Rapidly Reversible Photoprotective Energy Dissipation in the Absence of PsbS Protein by Enhanced pH. *The Journal of biological chemistry* **286**, 19973–19973 (2011).
- [74] Goss, R., Lepetit, B. & Wilhelm, C. Evidence for a rebinding of antheraxanthin to the light-harvesting complex during the epoxidation reaction of the violaxanthin cycle. *Journal of Plant Physiology* **163**, 585–590 (2006).

- [75] Goral, T. K. *et al.* Light-harvesting antenna composition controls the macrostructure and dynamics of thylakoid membranes in Arabidopsis. *The Plant Journal* **69**, 289–301 (2011).
- [76] Niyogi, K. K., Björkman, O. & Grossman, A. R. The roles of specific xanthophylls in photoprotection. *Proceedings Of The National Academy Of Sciences Of The United States Of America* **94**, 14162–14167 (1997).
- [77] Li, Z. *et al.* Lutein Accumulation in the Absence of Zeaxanthin Restores Nonphotochemical Quenching in the Arabidopsis thaliana npq1 Mutant. *The Plant Cell* **21**, 1798–1812 (2009).
- [78] Jahns, P. & Holzwarth, A. R. The role of the xanthophyll cycle and of lutein in photoprotection of photosystem II. *Biochimica Et Biophysica Acta* **1817**, 182–193 (2012).
- [79] Niyogi, K. K. *et al.* Photoprotection in a zeaxanthin- and lutein-deficient double mutant of Arabidopsis. *Photosynthesis Research* **67**, 139–145 (2001).
- [80] Zia, A., Johnson, M. P. & Ruban, A. V. Acclimation- and mutation-induced enhancement of PsbS levels affects the kinetics of non-photochemical quenching in Arabidopsis thaliana. *Planta* **233**, 1253–1264 (2011).
- [81] Crouchman, S., Ruban, A. & Horton, P. PsbS enhances nonphotochemical fluorescence quenching in the absence of zeaxanthin. *FEBS Letters* **580**, 2053–2058 (2006).
- [82] Funk, C. *et al.* The PSII-S protein of higher plants: a new type of pigment-binding protein. *Biochemistry* **34**, 11133–11141 (1995).
- [83] Terazono, Y. *et al.* Multiantenna Artificial Photosynthetic Reaction Center Complex. *Journal Of Physical Chemistry B* **113**, 7147–7155 (2009).
- [84] Savarese, M. *et al.* Fluorescence Lifetimes and Quantum Yields of Rhodamine Derivatives: New Insights from Theory and Experiment. *The Journal of Physical Chemistry A* **116**, 7491–7497 (2012).
- [85] Léonard, J. J. *et al.* Broadband ultrafast spectroscopy using a photonic crystal fiber: application to the photophysics of malachite green. *Optics Express* **15**, 16124–16129 (2007).
- [86] Fleming, G. R., Knight, A. W. E., Morris, J. M., Morrison, R. J. S. & Robinson, G. W. Picosecond Fluorescence Studies of Xanthene Dyes. *Journal Of The American Chemical Society* **99**, 4306–4311 (1976).
- [87] Magde, D., Rojas, G. & Seybold, P. Solvent dependence of the fluorescence lifetimes of xanthene dyes. *Photochemistry and Photobiology* **70**, 737–744 (1999).
- [88] Nagasawa, Y. *et al.* Ultrafast excited state deactivation of triphenylmethane dyes. *The Journal of Physical Chemistry A* **106**, 2024–2035 (2002).

- [89] Maruyama, Y., Magnin, O., Satozono, H. & Ishikawa, M. Ground- and Excited-State Isomerization of Triphenylmethane Dyes in the Femtosecond Regime. *The Journal of Physical Chemistry A* **103**, 5629–5635 (1999).
- [90] Dobryakov, A. L., Kovalenko, S. A. & Ernstring, N. P. Coherent and sequential contributions to femtosecond transient absorption spectra of a rhodamine dye in solution. *Journal Of Chemical Physics* **123**, 044502 (2005).
- [91] Robl, T. & Seilmeier, A. Ground-state recovery of electronically excited malachite green via transient vibrational heating. *Chemical Physics Letters* **147**, 544–550 (1988).
- [92] Nagasawa, Y., Ando, Y. & Okada, T. Solvent dependence of ultrafast ground state recovery of the triphenylmethane dyes, brilliant green and malachite green. *Chemical Physics Letters* **312**, 161–168 (1999).
- [93] Oster, G. & Nishijima, Y. Fluorescence and Internal Rotation: Their Dependence on Viscosity of the Medium1. *Journal Of The American Chemical Society* **78**, 1581–1584 (1956).
- [94] Duxbury, D. F. The photochemistry and photophysics of triphenylmethane dyes in solid and liquid media. *Chemical Reviews* **93**, 381–433 (1993).
- [95] Cai, N. *et al.* An Organic D--A Dye for Record Efficiency Solid-State Sensitized Heterojunction Solar Cells. *Nano Letters* **11**, 1452–1456 (2011).
- [96] Roncali, J. Molecular Bulk Heterojunctions: An Emerging Approach to Organic Solar Cells. *Accounts of Chemical Research* **42**, 1719–1730 (2009).
- [97] Haid, S. *et al.* Significant Improvement of Dye-Sensitized Solar Cell Performance by Small Structural Modification in  $\pi$ -Conjugated Donor-Acceptor Dyes. *Advanced Functional Materials* **22**, 1291–1302 (2012).
- [98] Ren, X., Jiang, S., Cha, M., Zhou, G. & Wang, Z.-S. Thiophene-Bridged Double D--A Dye for Efficient Dye-Sensitized Solar Cell. *Chemistry of Materials* **24**, 3493–3499 (2012).
- [99] Szarko, J. M., Guo, J., Rolczynski, B. S. & Chen, L. X. Nanoscale structure, dynamics and power conversion efficiency correlations in small molecule and oligomer-based photovoltaic devices. *Nano Reviews* **2** (2011).
- [100] Chen, L. X., Xiao, S. & Yu, L. Dynamics of photoinduced electron transfer in a molecular donor-acceptor quartet. *The Journal of Physical Chemistry B* **110**, 11730–11738 (2006).
- [101] Grebner, D., Helbig, M. & Rentsch, S. Size-Dependent Properties of Oligothiophenes by Picosecond Time-Resolved Spectroscopy. *Journal Of Physical Chemistry* **99**, 16991–16998 (1995).

- [102] Fujitsuka, M., Harada, K., Sugimoto, A. & Majima, T. Excitation Energy Dependence of Photoinduced Processes in PentathiophenePerylene Bisimide Dyads with a Flexible Linker. *The Journal of Physical Chemistry A* **112**, 10193–10199 (2008).
- [103] Wasielewski, M. R. Excited Doublet States of Electrochemically Generated Aromatic Imide and Diimide Radical Anions. *The Journal of Physical Chemistry A* **104**, 6545–6551 (2000).
- [104] Guo, J. *et al.* Structure and dynamics correlations of photoinduced charge separation in rigid conjugated linear donor-acceptor dyads towards photovoltaic applications. *New Journal Of Chemistry* **33**, 1497–1507 (2009).
- [105] Bhosale, S. V., Jani, C. H. & Langford, S. J. Chemistry of naphthalene diimides. *Chemical Society Reviews* **37**, 331 (2008).
- [106] Mullen, K. M. & van Stokkum, I. H. M. TIMP: an R package for modeling multi-way spectroscopic measurements. *Journal of Statistical Software* **18**, 1–46 (2007).
- [107] Hardin, B. E. *et al.* Increased light harvesting in dye-sensitized solar cells with energy relay dyes. *Nature Photonics* **3**, 406–411 (2009).
- [108] Yum, J.-H. *et al.* Incorporating Multiple Energy Relay Dyes in Liquid Dye-Sensitized Solar Cells. *ChemPhysChem* **12**, 657–661 (2011).
- [109] Fleming, G. R., Schlau-Cohen, G. S., Amarnath, K. & Zaks, J. Design principles of photosynthetic light-harvesting. *Faraday Discussions* **155**, 27–41 (2012).